# Acoustic Measurements of Stratification and Internal Seiching in an Enclosed Former Estuary

## A Case Study in Lake Veere

MSc Thesis

Patrick de Bruijn

TU Delft

# Acoustic Measurements of Stratification and Internal Seiching in an Enclosed Former Estuary

## A Case Study in Lake Veere

by

Patrick de Bruijn

to obtain the degree of Master of Science

at the Delft University of Technology,

to be defended publicly on Friday February 21, 2025 at 02:00 PM.

Student number: 4864034
Project duration: April 22, 2024 – February 21 , 2025

| | | | |
|---|---|---|---|
| Thesis committee: | Dr. ir. | W. M. Kranenburg | TU Delft, Deltares, supervisor |
| | Prof. dr. | J. D. Pietrzak | TU Delft, chair |
| | Dr. | A. Kirichek | TU Delft, committee member |
| | Ir. | H. M. Clercx | TU Delft, informer |
| | M.Sc. | M. Daugharty | Nortek Netherlands, informer |

Style: TU Delft Report Style, with modifications by Daan Zwaneveld

TU Delft

# Preface

Before you lies my master's thesis "Acoustic Measurements of Stratification and Internal Seiching in an Enclosed Former Estuary", which is the culmination of six years of studying civil engineering at Delft University of Technology, and with which I hope to add the prefix of engineer to my name.

Having spent an internship abroad, I was glad to arrive back home and pursue my interest in field-measurements. Moreover, I got to measure internal flow in a lake! Unexpectedly, I suddenly found myself in the field of underwater acoustics, which I (more than once) passingly described as an uphill battle. Nevertheless, it is a wondrous world of which I have learned much and more, even though I feel like I have barely scratched its surface. I am sure those experiences will come in useful in future research, and if not, I will cherish them whenever I am on a boat, in Zeeland, or playing a game of "fish-or-thermocline".

I would like to thank several people for their help during my thesis, starting with my committee. Wouter, you have been the hands-on supervisor that I needed, allowing me to pave my own path while keeping my overly large ambitions and all-over-the-place workflow on an academic leash. Thank you for your involved feedback, many meetings, and encouragement to present my work to the scientific community. Julie, thank you for sparking my interest in internal waves, sharing laughs over sushi and wine, and attending my meetings despite personal circumstances. Alex, thank you for our impromptu discussions and your grounding feedback. Maeve, thank you for your guidance through the acoustic labyrinth, your in-depth feedback, and your patience during long Teams sessions of me trying to code something that was already present in the Nortek software. Finally, Hannah, thank you for being in the trenches with me and, more importantly, being my friend in addition to being part of my (unofficial) committee. Good luck with my Python code; you get one daily question once we share an office.

Tess, I would like to thank you for your sample data. I hope my research helps you as much as your data helped me. Lab staff, thank you for your help in prepping me for the fieldwork. Best believe I will be driving that 4x4 soon! Sandra, thank you for being the best contact person I could wish for. To all my Fluid Mechanics colleagues and adherents, I could not wish for a more fun office. Maintaining our meme wall falls to you.

I would like to thank the StratiFEst user committee for engaging in discussions and allowing me to go on about echosounding in front of an interested audience. Finally, I would like to thank the Rijkswaterstaat Roompot crew for hosting and helping me during our measurement campaigns.

Finally, I would like to thank my friends and family. Acoustics is a field rich in imagery, and you allowed me to proudly share and discuss my figures with you—even in our most uninformed moments. Thank you to my partner for unconditionally loving and supporting me and reminding me about the things in life more important than the sonar equation. Thank you to my parents for always giving me freedom and providing me with opportunities, my big little brother for trading blows, beans, and laughs, and my little little brother for showing me the way in both personal and professional life.

*Patrick de Bruijn*
*Delft, February 2025*

*Historically, interpreting acoustic data often involved retreating to a backroom with colored pencils and funny cigarettes to magically emerge with a picture. We should move beyond this tradition by asking ourselves: What exactly are we looking at?*

— Paraphrased from Ruddick et al. (2009).

# Summary

Many enclosed former estuaries experience water quality problems. These problems are related to stratification, which inhibits the downward mixing of dissolved oxygen to the deep former estuarine channels and pits, leading to hypoxia. Former estuaries like Lake Veere and Grevelingenmeer have also seen events of massive fish mortality, presumably related to the wind-driven upwelling of deep water. To unravel these dynamics, we require more insight into the spatiotemporal behaviour of the stratification.

Stratification is currently measured through fortnightly temperature-salinity-oxygen transects with measurement points every few kilometres. These often do not capture all relevant dynamics, such as mixing and internal oscillations of isopycnals (e.g., tilting, seiching). Echosounding, which overcomes these issues, has been used extensively in the ocean to detect stratification but has seen limited use in lakes, where scatterers are often scarce. Impedance gradients by stratification are an established source of backscatter but are often overshadowed by other potential scatterers (i.e., air bubbles, biota, turbulence). The current generation of acoustic Doppler current profilers (ADCPs) allows for multi-frequency echosounding in combination with the usual velocity measurements, providing new opportunities to acoustically monitor stratification by covering a large frequency bandwidth.

In this study, we aimed to continuously monitor stratification and infer internal processes through narrowband multi-frequency echosounding. In the summer of 2024, we collected measurements with two uplooking ADCPs, three underwater moorings equipped with thermistor chains, and a high-resolution CTD casting instrument in the northwest of Lake Veere. The ADCPs measured backscatter at three frequencies: $250$, $500$, and $1000$ kHz, a wide bandwidth that we expected to facilitate the distinction between backscatter mechanisms at a high spatial resolution. We compared direct temperature measurements by moorings, high-resolution conductivity-temperature-depth (CTD) casts, and frequency-dependent acoustic backscatter to infer backscatter mechanisms. We then used the acoustic backscatter to monitor stratification by tracking (gradient) maxima and compared acoustically derived thermocline heights to directly inferred thermocline heights from the temperature moorings. Finally, we used the monitored stratification to characterize internal seiching by combining data from several locations. To that end, we analysed the time series of thermocline heights using the continuous wavelet and wavelet coherence transforms to identify periods of internal seiching and validated those with current profiles measured by the ADCPs.

We observed stratification of the upper water column in the acoustic data during extended warm periods. The upper and lower layers were separated by a gradient in backscatter, with increased backscatter in the upper water column. This gradient coincided with the directly measured main thermocline, demonstrating the potential of monitoring the thermocline height through acoustic backscatter. We hypothesize that the large backscatter gradient (as opposed to a local backscatter maximum) was caused by a difference in phytoplankton concentration, which remained above the thermocline through buoyancy and bloomed during extended warm periods (end of July and August). Consequently, stratification was more visible in the acoustic data during these warm periods, despite not necessarily being strongest at those times. We did not observe impedance gradients due to stratification; instead, we attribute local backscatter maxima to suspended matter aggregating on isopycnals. As such, we continuously observed a secondary layer near the bed throughout June and July.

We computed phase velocities of internal seiching using CTD casts and estimated the internal seiching bandwidth between $1$–$10$ hours. We found events of cross-lake and along-lake internal seiching—with respective periods of $4$ and $6$ hours—in thermocline heights through increased wavelet coherence and out-of-phase behaviour between measurement locations on opposing sides of the lake. Additionally, most thermocline height time series sporadically contained a daily component, which was likely forced by wind rather than heat input. The secondary layer near the bottom contained both a daily and semi-daily component, with the latter likely related to tidal forcing. We validated the observed internal seiching

using velocity data to confirm that velocities above and below the thermocline were out-of-phase (i.e., reversed). Finally, we found that velocity shear was not a consistent indicator of thermocline height, but was often either concentrated at or bounded by the thermocline, thus providing a general measure of the average thermocline height.

In conclusion, we found that acoustic backscatter is strongly related to stratification. A strong backscatter gradient—hypothetically a gradient in phytoplankton concentration—distinguished the layers above and below the thermocline. Similarly, we hypothesized that aggregating suspended matter indicated the presence of a deeper pycnocline. Both can be tracked through maximum (gradient) approaches and we found that the backscatter gradient coincided with the thermocline. The generalization of this method to other sites largely depends on the presence of these gradients, which we hypothesize to be largely dependent on biological productivity and the absence of other dominant scattering mechanisms (i.e., bubbles injected by waves). Key considerations for future research include improving the robustness of the inference algorithm, optimizing the frequency of acoustic pulses, and echosounder calibration.

# Contents

# List of Figures

# List of Tables

# Nomenclature

## Abbreviations

| Abbreviation | Definition |
|---|---|
| ABS | Acoustic backscatter sensor |
| ADCP | Acoustic Doppler current profiler |
| ADV | Acoustic Doppler velocimeter |
| CWT | Continuous wavelet transform |
| CTD | Conductivity-temperature-depth |
| ENU | East-North-Up |
| FS | Full-scale range |
| MLD | Mixed layer depth |
| PSU | Practical salinity unit |
| RQ | Research question |
| RWS | Rijkswaterstaat |
| SBL | Surface boundary layer |
| StratiFEst | Stratification, Circulation and Mixing in Enclosed Former Estuaries |
| TSO | Temperature-salinity-oxygen |

## Symbols

| Symbol | Definition | Unit |
|---|---|---|
| $A$ | Area ensonified by echosounder | [m$^2$] |
| $a$ | Transducer radius | [m] |
| $B\left(\theta\right)$ | Localization term for targets | [dB] |
| $C_{10}$ | Wind drag coefficient | [-] |
| $c$ | Wave speed | [m/s] |
| $c_s$ | Speed of sound | [m/s] |
| $D_{\text{min}}$ | Minimum particle diameter required for scattering | [m] |
| $D_{\text{peak}}$ | Particle diameter at which scattering is at a maximum | [m] |
| $f$ | Inertial frequency | [rad/s, Hz] |
| $f_{\text{height}}$ | Factor for threshold of peak height | [-] |
| $f_{\text{prom}}$ | Factor for threshold of peak prominence | [-] |
| $f_s$ | Sampling frequency | [Hz] |
| $G$ | Calibration gain | [dB] |
| $G_{\text{int}}$ | Calibration gain for volume | [dB] |
| $g$ | Gravitational acceleration | [m/s$^2$] |
| $g'$ | Reduced gravitational acceleration | [m/s$^2$] |
| $h$ | Layer thickness | [m] |
| $h_1$ | Surface layer thickness | [m] |
| $h_2$ | Bottom layer thickness | [m] |
| $\delta j$ | Wavelet scale resolution | [-] |
| $k$ | Acoustic wavenumber | [rad/m] |
| $L$ | Longitudinal extent of lake | [m] |
| $L_e$ | Integration length scale | [m] |
| $M_{\text{bc}}$ | Baroclinic moment about centre of volume in a lake | [Nm] |

| Symbol | Definition | Unit |
|---|---|---|
| $N$ | Buoyancy frequency | [rad/s, Hz] |
| $N_{\text{samples}}$ | Number of samples per burst | [-] |
| $N_{\text{signal}}$ | Number of samples in a signal | [-] |
| $N_{\text{sub}}$ | Number of sublayers | [-] |
| $NT$ | Noise threshold | [dB] |
| $N_{\text{signal}}$ | Number of samples in the signal | [-] |
| $P_r$ | Power level recorded by echosounder | [dB] |
| $PL$ | Reference power level | [dB] |
| $p$ | Pressure | [Pa] |
| $p_{\text{inc}}$ | Pressure of incoming pressure wave | [N/m$^2$] |
| $p_{\text{scat}}$ | Pressure of scattered pressure wave | [N/m$^2$] |
| $R$ | Reflection coefficient | [-] |
| $r$ | Range | [m] |
| $r'$ | Range over a stratification structure | [m] |
| $r_{\text{max}}$ | Range of echosounder | [m] |
| $\Delta r$ | Range-resolution of echosounder | [m] |
| $S$ | Salinity | [PSU] |
| $S_v$ | Volume backscatter | [dB re $1\,\text{m}^{-1}$] |
| $S_{v,c}$ | Volume backscatter corrected for noise | [dB re $1\,\text{m}^{-1}$] |
| $S_{v,NT}$ | Volume backscatter calculated from noise | [dB re $1\,\text{m}^{-1}$] |
| $SNR$ | Signal-to-noise ratio | [dB] |
| $s$ | Wavelet scale | [s] |
| $T$ | Temperature | [°C] |
| $T_1$ | Mode-1 internal seiching period | [s] |
| $T_{\text{Fourier}}$ | Fourier period | [s] |
| $T_{\text{pot}}$ | Potential temperature | [°C] |
| $TS$ | Target strength | [dB re $1\,\text{m}^2$] |
| $TSI$ | Thermocline strength index | [°C/m] |
| $\Delta t$ | Timestep | [s] |
| $th_{\text{prom}}$ | Threshold of peak height | [-] |
| $th_{\text{height}}$ | Threshold of peak height | [-] |
| $U_{10}$ | Wind speed measured at $10\,\text{m}$ above the surface | [m/s] |
| $u$ | Horizontal velocity | [m/s] |
| $u_*$ | Shear velocity of wind | [m/s] |
| $z$ | Vertical coordinate | [m] |
| $z_{\text{max}}$ | Maximum height in water column of peaks in volume backscatter | [m] |
| $z_{\text{min}}$ | Minimum height in water column of peaks in volume backscatter | [m] |
| $z_v$ | Depth of the centre of volume of a lake | [m] |
| $\Delta z$ | Minimum vertical distance between peaks | [m] |

## Greek Symbols

| Symbol | Definition | Unit |
|---|---|---|
| $\alpha$ | Acoustic absorption coefficient | [dB/m] |
| $\Delta$ | Thickness of a homogeneous sublayer | [m] |
| $\eta$ | Acoustic impedance | [-] |
| $\theta_{1/2}$ | Half of beam angle | [rad] |
| $\mu_{\text{geom}}$ | Geometric mean | [dB] |
| $\xi$ | Dimensionless time | [-] |
| $\psi$ | Complex amplitude of vertical velocity | [m/s] |
| $\rho$ | Density of water | [kg/m$^3$] |

| Symbol | Definition | Unit |
|---|---|---|
| $\rho_a$ | Density of air | [kg/m$^3$] |
| $\rho_v$ | Volumetric density of targets in the beam | [$1$/m$^3$] |
| $\sigma_{bs}$ | Backscattering cross-section | [m$^2$] |
| $\sigma_{\text{geom}}$ | Geometric standard deviation | [dB] |
| $\sigma_v$ | Volume backscattering cross-section | [$1$/m] |
| $\tau_{\text{wind}}$ | Shear stress by wind acting on water surface | [N/m$^2$] |
| $\tau_{\text{SBL}}$ | Shear stress by wind transferring momentum to surface boundary layer | [N/m$^2$] |
| $\tau_{\text{wave}}$ | Shear stress by wind transferring momentum to surface waves | [N/m$^2$] |
| $\tau_{\text{pulse}}$ | Pulse length | [s] |
| $\tau_{e\text{-folding}}$ | $e$-folding time | [s] |
| $\phi$ | Latitude | [rad] |
| $\Psi$ | Equivalent beam angle | [dB] |
| $\Psi_0$ | Wavelet function | [-] |
| $\psi$ | Complex amplitude of vertical velocity | [m/s] |
| $\Omega$ | Frequency of Earth's rotation | [rad/s] |
| $\omega_0$ | Dimensionless frequency | [-] |

# Dimensionless Numbers

| Symbol | Definition |
|---|---|
| $L_N$ | Lake number |
| $Ri_{\text{b}}$ | Bulk Richardson number |
| $Ri_{\text{g}}$ | Gradient Richardson number |
| $S_i$ | Burger number |
| $St$ | Schmidt stability number |
| $W$ | Wedderburn number |

# 1 Introduction

Globally, estuaries have been increasingly altered through anthropogenic influence for coastal protection, land reclamation, and freshwater divergence (Jung et al., 2024). As such, the North Sea floods of 1953 prompted the Dutch government to create the Deltaworks, entailing the closure of several tidal estuaries in the south of the Netherlands. One such former estuary is Lake Veere (Craeymeersch and De Vries, 2007), located in Zeeland, the Netherlands (Figure 1.1a). Lake Veere was created after its enclosure by the Zandkreekdam and the Veerse Gatdam in 1960 and 1961, respectively (Prins et al., 2024). Since then, it has become a brackish lake, still characterized by features commonly associated with tidal estuaries, such as shoals and deep tidal channels, which can be observed in Figure 1.1b.

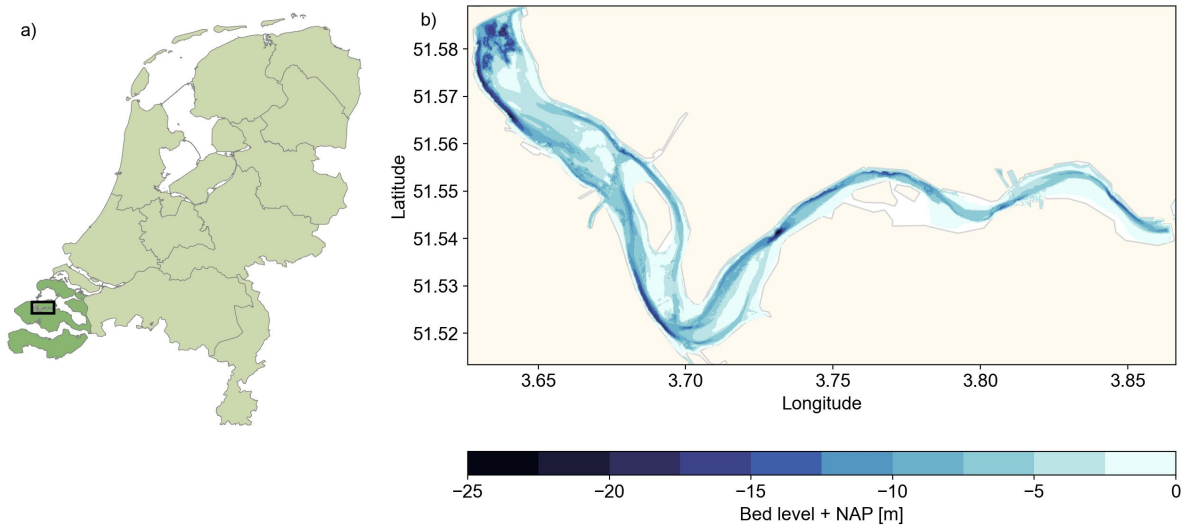


**Figure 1.1:** a) Lake Veere in Zeeland, the Netherlands, and b) bathymetry of Lake Veere. Bathymetry data was obtained from Rijkswaterstaat.

## 1.1. Research context

Ever since its enclosue, the water quality of Lake Veere has been degrading (Holland et al., 2004; Prins et al., 2015). Measurements have shown hypoxia and the presence of hydrogen sulfide in the deep parts of Lake Veere. In 2004, a flush gate was added to the system to increase the mixing of the stagnant deeper layers with water from the Eastern Scheldt (Craeymeersch and De Vries, 2007). While this led to an enhancement in water quality in the eastern part of Lake Veere, no corresponding improvement was observed in the middle and western parts (Prins et al., 2015). In recent years, fish mortality events in the northwest part of the lake during the warm summers of 2018 and 2019 (Prins et al., 2023, 2024), triggered a response by Rijkswaterstaat (RWS), who initiated a project to assess water quality in Lake Veere.

The presence of a strong temperature gradient, or thermocline, typically inhibits mixing, leading to the anoxification of deeper layers due to the limited re-aeration by the atmosphere and the increased oxygen demand associated with higher bacterial production in these layers (Boehrer and Schultze, 2008; Greenwood et al., 2010). This production stems from the decomposition of organic material—

most abundant during summer—sinking to the bottom. Consequently, Prins et al. (2024) hypothesize three major factors contributing to the poor water quality in the northwestern part of Lake Veere: 1) the thermal stratification inhibiting mixing during summer, 2) a high oxygen demand of bottom sediment, and 3) the long travel distance for oxygen-rich water from the Eastern Scheldt between the flush gate in the east and the middle/western part of Lake Veere. Furthermore, two possible causes for fish mortality were hypothesized: 1) the upwelling of deep anoxic water and 2) the release of hydrogen sulfide from bottom sediment (Prins et al., 2024). Upwelling of anoxic water was hypothesized to be caused by wind-induced tilting of isopycnals (Kranenburg, 2023), while the accompanying circulation and subsequent generation of internal seiching may contribute to the internal mixing and/or release of hydrogen sulfide from the bottom sediment. The circulation and mixing patterns contributing to the re-aeration of the water column remain relatively unexplored. Mapping these mechanisms is essential to understanding the relation between wind and (temporary) water quality degradation in Lake Veere.

## 1.2. Problem definition

Monitoring is essential to describe all dynamics contributing to the poor water quality in Lake Veere. Water quality is currently monitored through TSO (temperature-salinity-oxygen) and $H_2S$ (hydrogen sulfide) measurements along a transect consisting of 17 measurement points. At these locations, temperature, salinity, oxygen, and hydrogen sulfide concentrations are measured at a vertical resolution of approximately $1$ meter. Before 2020, these were performed at a seasonal frequency, which was increased to monthly after the start of the monitoring project and fortnightly after the fish mortality events. An example of such measurements and their respective locations is shown in Figure 1.2. Besides vessel-based measurements, two measurement buoys were installed for the summers of 2021 and 2022 (Prins et al., 2023), providing continuous TSO measurements near Veere (2021, 2022) and in the northwest of Lake Veere (2021). Finally, RWS deployed two acoustic Doppler current profilers (ADCPs) during the spring of 2024.

While the regular TSO measurements provide valuable insights into the existence and location of the seasonal thermocline, they fall short of providing a holistic understanding of all dynamics that may contribute to poor water quality. To illustrate this, the temperature measured by RWS at measurement point 1 is shown in Figure 1.3. Based on these fortnightly profiles, strong stratification may be observed during the summers of 2020, 2021, and 2022. However, key physical processes, such as thermocline motions (e.g., tilting) and turbulent mixing through entrainment of the thermocline or internal wave breaking remain insufficiently characterized. This gap in understanding is attributed to several limitations in the measurements. Firstly, the absence of velocity measurements in TSO data means crucial information on circulation, upwelling, internal waves, and turbulence remains unattainable. Secondly, the current measurements lack temporal continuity, being captured at discrete intervals of $2$–$4$ weeks with a single device, reducing their ability to observe dynamic processes. Thirdly, the current measurement method precludes simultaneous sampling, allowing the measurement site to be subjected to external factors in between measurements. Finally, their spatial scope is constrained to a single transect positioned above deeper waters due to limitations imposed by the vessel's hull depth, restricting measurement locations to the deeper fairway. The resolution-related limitations are clearly visible in Figure 1.2 and Figure 1.3, in which spatial and temporal gradients, respectively, are only available at large respective scales. In summary, the current measurement method does not capture the full range of processes contributing to circulation in Lake Veere.

Acoustic measurements have historically been an important aspect of oceanography (Medwin and Clay, 1998). Relying on the reflection of acoustic pulses, acoustic measurements include (among others) echosounding and velocimetry, measured by echosounders and ADCPs, respectively. Both divide the water column into cells and send out acoustic pulses, of which an ADCP measures amplitude (i.e., backscatter) and Doppler shift (i.e., velocities) upon reception, while an echosounder only measures the amplitude.

Echosounders measure echo intensity, which depends on material properties, size, shape, roughness, and distribution of the scatterers (Bassett et al., 2023). They have historically been used to measure bathymetry (Mohammadloo et al., 2020), localize fish (Foote, 2009), study salt wedges in estuaries (Penrose and Beer, 1981), and study internal waves (Haury et al., 1979; Kranenburg et al., 1991; Pietrzak et al., 1991). The latter two have generally taken place at strong interfaces between fresh

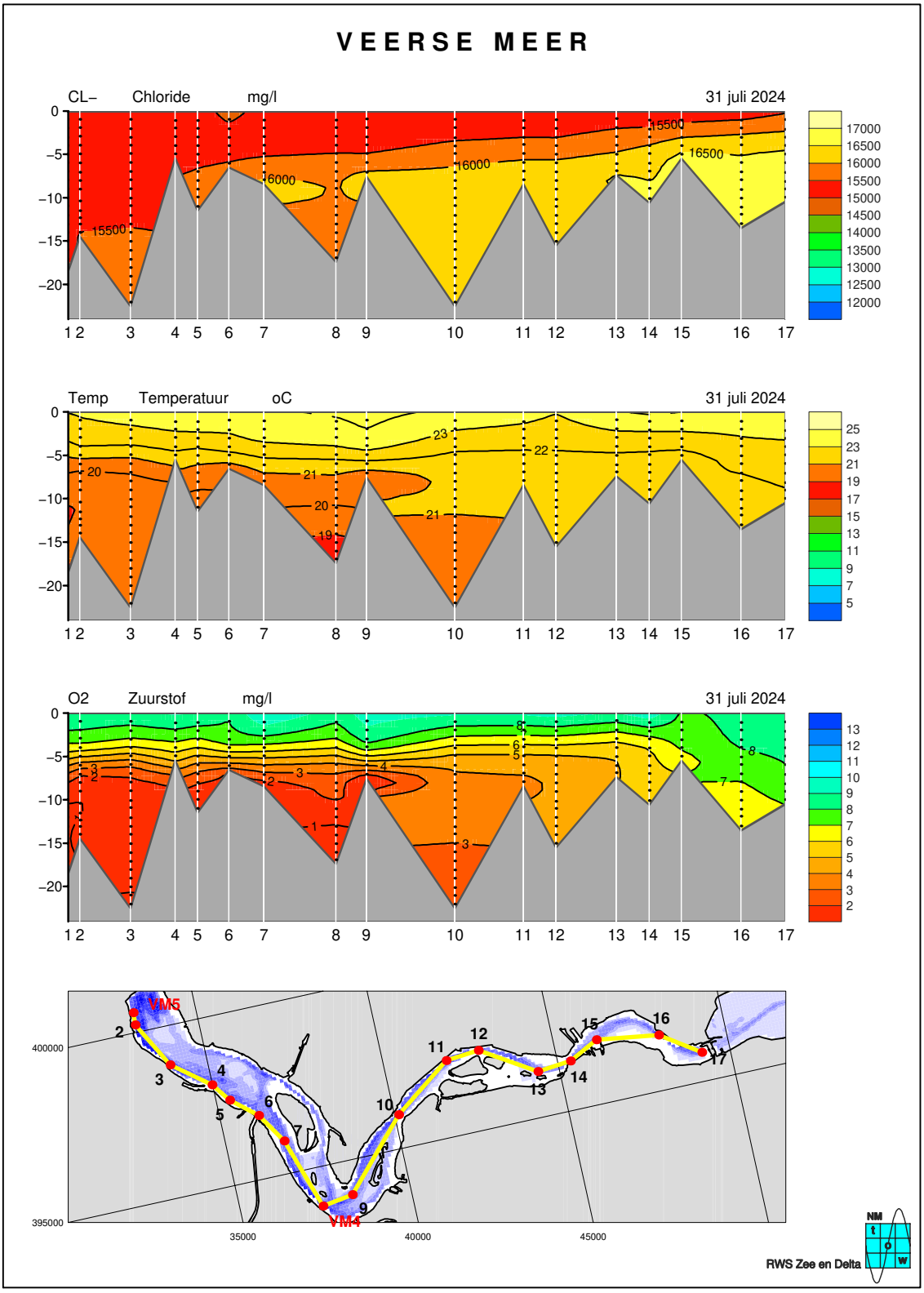


**Figure 1.2:** TSO-measurements in Lake Veere on July 31st, 2024. From top to bottom: chloride concentration [mg/l] as a proxy for salinity, temperature [°C], oxygen concentration [mg/l], and location of measurement points in Lake Veere. Depth is shown on the left axes. Measurements and visualization by Rijkswaterstaat (RWS).

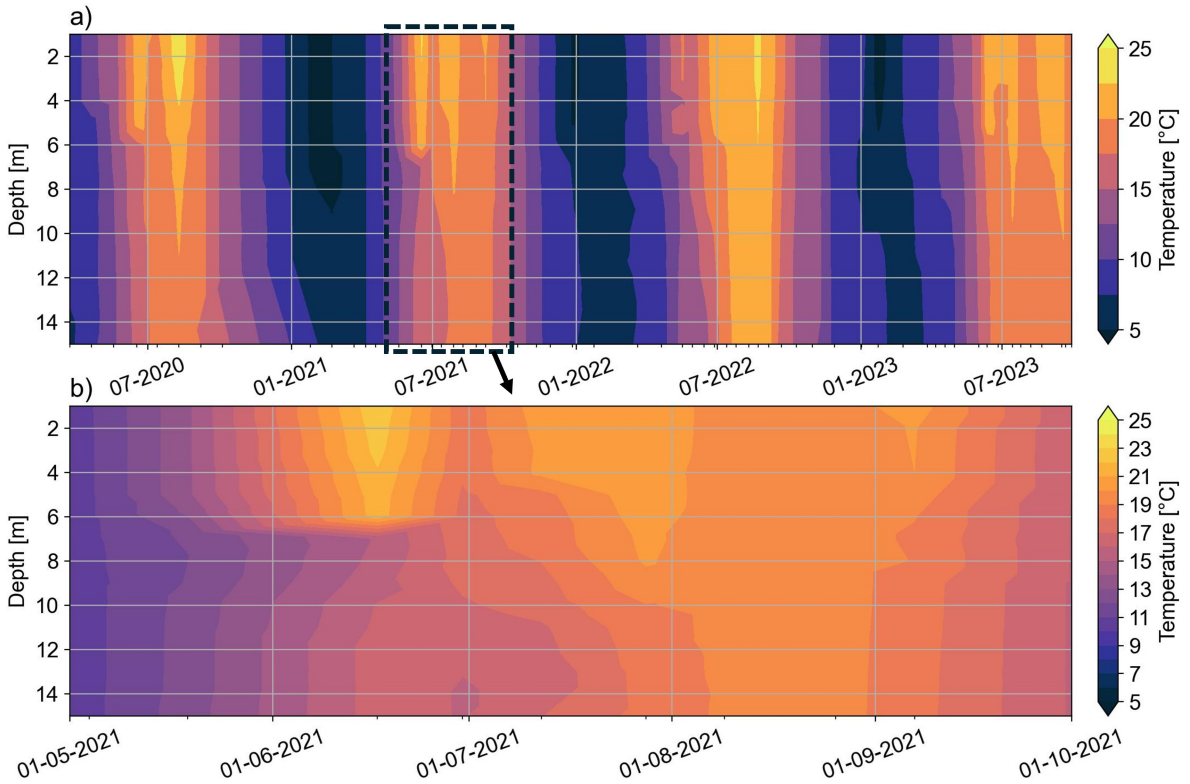


**Figure 1.3:** Temperature over time and depth at measurement point 1 in the northwest of Lake Veere from a) 2020 to 2023 and b) May to September 2021. The resolution of the depth measurements is roughly $1$ meter. The profiles are interpolated to get a continuous time series over depth. Measurements were obtained from Rijkswaterstaat and are part of the fortnightly TSO transect. Minor ticks on the x-axis indicate the measurement dates, which are spaced non-uniformly due to the increased measurement frequency during summer.

and saline water (e.g., in estuaries) or at sites where backscatter by stratification dominates (e.g., in the ocean). Inverted echosounders (Rossby, 1969), which rely on the same principle but are mounted on the bottom instead of a vessel or buoy and look upwards instead of downwards, have recently proven useful for measuring internal waves (Li et al., 2009), internal flow (Macrander et al., 2007), and oceanic mixed layer depth (Brenner et al., 2023). In the absence of interfering scatterers, small density steps as small as $0.1$ g/L may be identified (Stranne et al., 2017), showing the applicability of acoustic instruments for measuring relatively small density steps. However, acoustically detecting thermal stratification proved difficult due to the limited (gradient of) backscattered acoustic energy, the limited presence of scatterers, and noise caused by other dynamics (Assunção et al., 2021). Furthermore, attributing backscatter to specific scattering mechanisms remains challenging in the absence of complementary measurements of these scatterers, but attempts have been made through the analysis of their frequency-dependence (i.e., spectral slopes; Bassett et al., 2023; Warren et al., 2003), which is facilitated by multi-frequency echosounding.

ADCPs have been long established to measure full velocity profiles over the water column (Ton et al., 2020). Full velocity profiles may be used to map currents in dynamic systems (Kranenburg et al., 2023), to analyze the seasonal energy input in lakes (Simpson et al., 2021), to estimate the location of sharp density gradients using the local maximum of interfacial shear (Brenner et al., 2023; Macrander et al., 2007), or to characterize the internal wave field in lakes (Antenucci et al., 2000; Flood et al., 2020). Accurately measuring velocities requires a coarser resolution, so, recently, echosounders have been integrated into ADCPs through the addition of a fifth measurement beam (Bassett and Zeiden, 2023; Black et al., 2015), which operates at multiple frequencies semi-simultaneously. These ADCPs provide continuous non-intrusive measurements of currents and backscatter at multiple frequencies, allowing for both mapping of circulation patterns and inferring site-specific scattering mechanisms at a high resolution over the entire water column, providing new opportunities for the study of internal processes

contributing to the degrading water quality in Lake Veere.

In summary, deploying (multiple) ADCPs potentially solves monitoring issues relating to the lack of current velocities, temporal and vertical resolution, and simultaneous sampling. Additionally, stratification may be observed directly through acoustic backscatter by density gradients, allowing inferring of thermocline height and corresponding motions (e.g., tilting). Observing stratification remains challenging, though, with few application examples of echosounders in thermally stratified lakes (or former estuaries) due to the dominance of other processes over backscatter by temperature gradients or the absence of scatterers entirely.

## 1.3. Objectives

This research aims to develop a method to monitor thermal stratification from continuous acoustic measurements and to describe the motions of the thermocline that contribute to circulation in Lake Veere. Successfully measuring these extends the applicability of acoustic measuring techniques to other low-dynamic sites, where temperature stratification is dominant and density anomalies are minimal. Ultimately, successfully measuring these dynamics contributes to a parameterization that describes the relation between wind, mixing, and stratification in Lake Veere and similar systems.

We aim to do this using measurements of acoustic backscatter, currents, and temperature conducted in the summer of 2024. These measurements were collected with two bottom-mounted ADCPs with multi-frequency echosounding, measuring current velocities and acoustic backscatter, accompanied by three temperature moorings. These moorings collect high-resolution continuous temperature measurements and consist of temperature sensors, pressure sensors and CTD (conductivity-temperature-depth) sensors. Finally, casts are made using a CastAway CTD to collect high-resolution CTD data over the same transect as the TSO measurements of Rijkswaterstaat. Summarizing, four methods for detecting thermal stratification are employed: acoustic backscatter, velocities, temperature moorings, and CTD casts. The focus lies, however, on the technological innovation that is the echosounding functionality of the ADCPs.

In this way, the exact location of the thermocline is measured continuously. Successfully conducting these measurements entails extensive research on acoustic measurement devices and the site-specific characteristics that allow for the detection of the thermocline, complicated by its sporadic existence. Multiple expeditions were undertaken with the CastAway CTD during the summer of 2024. Furthermore, the noisy nature of acoustic data entails a large amount of post-processing.

This research is scoped mostly to the analysis of the data collected by the ADCPs and with the CastAway CTD to find the thermocline depth in Lake Veere. This included planning and logistics, safety, and device management for the CastAway CTD. The logistics of the other measurements are not included. This analysis is further supported by data gathered from the moorings. The analysis thus includes four methods of determining the interface depth and associated oscillations but does not include the inverse modelling of density, temperature or other constituents, which is impossible with uncalibrated echo data. The analysis of turbulent mixing is not included due to time constraints and the limited vertical resolution of the velocity data. Furthermore, forcing mechanisms (e.g., wind, flush gate discharge) are excluded from this research.

## 1.4. Research questions

The following research question (RQ) summarizes the objectives of this research:

*To what extent can thermal stratification and corresponding internal oscillations be measured with acoustic instruments in low-dynamic former estuaries?*

This research question is divided into several sub-questions, which are listed below. Firstly, the different dynamics that may be expected are researched and characterized, making sure that all oscillations with corresponding frequencies are correctly identified from the data.

1. *Which thermocline dynamics are expected in Lake Veere?*

Having identified all physical processes that influence internal dynamics, we proceed with constructing a measurement and analysis methodology. This entails research regarding underwater acoustics in the

presence of thermal stratification. Furthermore, post-processing and analysis methods are researched to ensure optimal usage of the data.

2. *How have acoustic instruments historically been used to measure (thermal) stratification and what are the most important factors determining their effectiveness?*

The collected data are analyzed to confirm the presence of the dynamics identified in sub-question 1. These are compared across the different measurement methods to study the accuracy and effectiveness of measuring thermocline height through acoustic backscatter. Ground truth measurements (i.e., temperature moorings) are used to validate this.

3. *To what extent can thermal stratification be observed through acoustic backscatter and velocity measurements in Lake Veere?*

Having found and characterized periods of stratification and periods of mixing by answering the previous questions, we proceed with an analysis to study the spatio-temporal evolution of this stratification. These are compared across the different measurement methods to arrive at conclusions regarding the expected internal dynamics in Lake Veere.

4. *Which internal oscillations are observed in Lake Veere (and how do these compare across the measurements by the ADCPs and the temperature moorings)?*

## 1.5. Outline

This research proposal is structured as follows. Chapter 2 presents a literature review discussing relevant historical and recent developments in the research areas of thermal stratification, internal flow, and underwater acoustics in the presence of stratification. Supported by this theoretical framework, the research methodology is presented in Chapter 3. This consists of both directly and acoustically inferring thermocline heights and analyzing the frequency components in these heights using the continuous wavelet transform. The results are presented in Chapter 4. These are interpreted and placed in the wider scientific context in Chapter 5. Conclusions and recommendations are presented in Chapter 6 and Chapter 7, respectively.

# 2
# State-of-the-art

Chapter 1 outlined the research problem, highlighting the division between two main topics: the physics of stratification and internal flow, and underwater acoustics in stratified environments. Our approach addresses these through the first two research questions. Ultimately, we arrive at the internal dynamics common in (thermally) stratified lakes (RQ1). Additionally, by building on previous acoustic stratification studies, we extend the application of acoustic measurements to stratified lakes, enabling acoustic monitoring of thermocline heights (RQ2).

This chapter is structured as follows. Firstly, we research the physics associated with the formation of a thermocline in Section 2.1. Section 2.2 discusses the dynamics specific to wind forcing that may occur in the presence of (thermal) stratification. Section 2.3 treats the relevant physics of underwater acoustics and how acoustic measurements have historically been used and analyzed in the context of stratification. Finally, Section 2.4 introduced the case study in the context of stratification and related dynamics.

## 2.1. Thermal stratification in lakes

In this section, we discuss thermal stratification in lakes. Firstly, we define stratification in general, including some important stability conditions. Secondly, we discuss the seasonality of thermal stratification.

### 2.1.1. Stratification

The distribution of constituents throughout natural water bodies is often non-uniform. This variation affects water density, giving rise to stratification. Stratification refers to the separation of the water column into layers, each with a distinct density. These layers may be discrete or continuous. Water density is a function of temperature and dissolved substances, with mineral concentrations playing a significant role (Boehrer and Schultze, 2008). The water density as a function of (potential) temperature and salinity is commonly described by the UNESCO formula (Fofonoff and Millard, 1983). The full formulas are provided in Appendix A. This relation is also plotted in Figure 2.1a.

Stable stratification typically suppresses mixing due to a positive feedback loop: as stratification increases, mixing is further reduced, facilitating the increase of stratification. Initial stratification may, for example, be caused by heat input from the atmosphere or fresh riverine waters overlaying salty oceanic waters. In a stably stratified fluid, density increases with depth and the fluid is in hydrostatic equilibrium (in the absence of forcing). A stratified structure may be observed as, for example, two-layer systems separated by a strong density gradient, complex thermohaline staircases separated by small (yet discrete) density increments (e.g., Kranenburg et al., 2020; Sommer et al., 2013; Stranne et al., 2017), or as more continuous density profiles. Strong density gradients separating layers are known as pycnoclines, which can be further categorized as haloclines, chemoclines, or thermoclines depending on the dominant factor contributing to the density gradient (Boehrer and Schultze, 2008). Among these, thermoclines are particularly important to the study of Lake Veere (Prins et al., 2024).

A sharp density gradient is associated with a local minimum in turbulent kinetic energy, resulting in minimal mixing that may only affect a few percent of the water column (Wüest and Lorke, 2003). The stability of a stratified system under the influence of vertical velocity shear is commonly assessed using the bulk Richardson number (Kirillin and Shatwell, 2016; Stevens and Imberger, 1996)

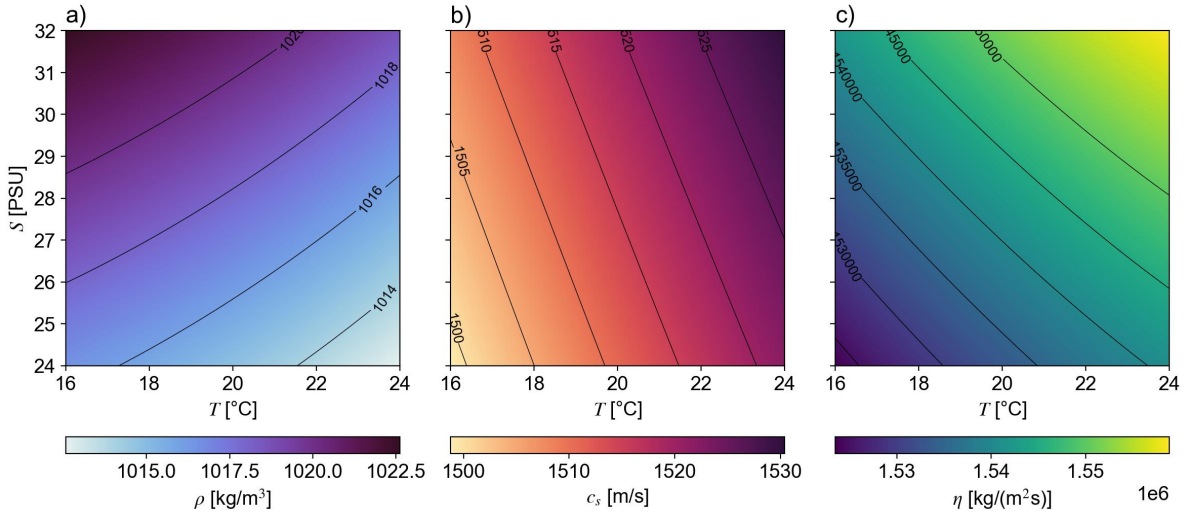


**Figure 2.1:** a) Density distribution in accordance with the UNESCO formula, b) speed of sound in seawater in accordance with the parametrization by Chen and Millero (1977), and c) corresponding acoustic impedance. Temperature and salinity cover ranges typical for Lake Veere during summer. The pressure was taken as constant at $20$ dbar.

$$Ri_{\mathsf{b}} = \frac{g' h_1}{u_*^2} \tag{2.1}$$

or the gradient Richardson number (Kirillin and Shatwell, 2016)

$$Ri_{\mathsf{g}} = \frac{-\frac{\partial g'}{\partial z}}{\left(\frac{\partial u}{\partial z}\right)^2} = \frac{-g\frac{\partial \rho}{\partial z}}{\rho\left(\frac{\partial u}{\partial z}\right)^2}, \tag{2.2}$$

which represent the ratio of buoyancy and shear forces in the vertical momentum equation, or, the ratio of turbulence damping and generation. Here

$$g' = g\frac{\Delta\rho}{\rho_0} \tag{2.3}$$

is the reduced gravity, with $\rho_0$ representing the average density of two layers and $\Delta\rho$ their density difference. Furthermore, $h_1$ denotes surface layer thickness, $u_*$ the shear velocity of the wind, $u$ horizontal velocity, and $z$ vertical coordinate. $Ri > \frac{1}{4}$ is commonly used as a stability condition for both the bulk and gradient Richardson numbers (Howard, 1961; Miles, 1961). Galperin et al. (2007) provide a short discussion on deviations, but, generally, $Ri$ of order unity suggests a stable stratification. Sharper density gradients are associated with increased stratification stability.

### 2.1.2. Seasonal thermal stratification

Thermal stratification arises from temperature differences over the water column. In a stably stratified body of water, warmer, less dense water overlays colder, denser water. The temperature of the surface water depends on solar radiation, heat loss through long-wave emittance, heat exchange with the atmosphere and heat fluxes associated with evaporation and precipitation (Boehrer and Schultze, 2008). Conversely, the bottom layer remains shielded from these mechanisms and only exchanges heat with the surface layer through diffusion, which is historically divided into very slow molecular diffusion, and turbulent diffusion driven by wind stress on the surface (Boehrer and Schultze, 2008; Wüest and Lorke, 2003).

During the summer, when atmospheric temperatures and insolation reach their maximum, the surface layer is heated. Above a minimum temperature of $4\,^{\circ}$C (which corresponds to the maximum density of

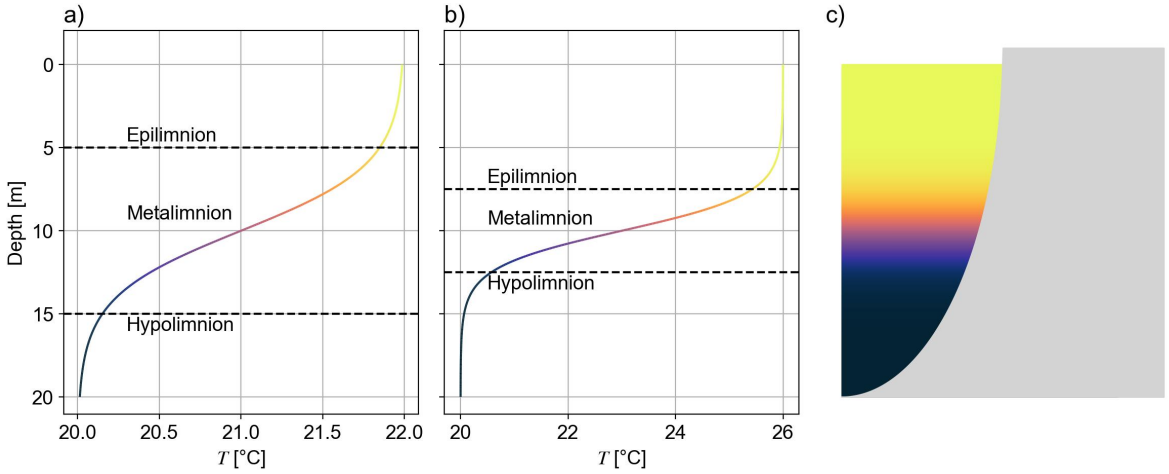


**Figure 2.2:** Temperature over depth with the water column divided into three layers: epilimnion, metalimnion, and hypolimnion. After decreased heat input and increased mixing during winter, a) the epilimnion is gradually heated. After increased heat input, b) the temperature difference increases and the thermocline sharpens. Panel c) shows a sample cross-section of the temperature distribution in a thermally stratified lake.

water), density gradients may sufficiently counteract the wind-induced turbulent diffusion to only penetrate up to a certain depth, allowing the formation of a thermocline (Boehrer and Schultze, 2008). This separates the water column into two layers: the surface layer or epilimnion and the bottom layer or hypolimnion. These layers are occasionally separated by an intermediary layer known as the metalimnion, which is also the location of a thermocline in the case of a sharp temperature gradient. This is illustrated in Figure 2.2. The thickness of these layers is a function of heat input and wind forcing and is not constant over the stratification period. Stronger heat forcing accounts for a thicker epilimnion. Accordingly, lower surface temperatures and increased wind forcing during the fall erode the thermocline, homogenizing the lake. The seasonality of heat input from the atmosphere and of wind forcing results in seasonality in thermal stratification, which is also visible in Figure 1.3, generally showing a stronger thermal stratification in Lake Veere during the summer months.

Several methods to derive the thermocline depth (or epilimnion thickness) from measurements have been suggested. These methods differ between limnic and oceanic research but usually rely on temperature gradients.

Historically, the thermocline depth is found using the maximum temperature gradient (e.g., Yang et al., 2020; Yu et al., 2010). This is referred to as the thermocline strength index ($TSI$) and is computed as $TSI = \Delta T/\Delta h$, where $\Delta T$ denotes the temperature difference over the thermocline and $\Delta h$ the thickness of the thermocline. The existence of a thermocline is commonly assessed using empirical values of this gradient of order unity (Yu et al., 2010), but different values have been proposed. These gradient methods perform less well when applied to noisy, high-frequency measurements, so Xu et al. (2019) developed a more robust algorithm to characterize lake stratification. In this algorithm, the temperature profile is first approximated with linear segments. The middle of the linear segment with the highest gradient is set as the thermocline depth, with a threshold gradient set at $0.15\,^{\circ}$C/m (in accordance with the common gradients between $0.05\,^{\circ}$C/m and $1\,^{\circ}$C/m). In this method, the limited amount of linear segments smooths out the noisier data. Not all methods are directly related to temperature gradients; the first moment of density has also been used in previous studies to derive thermocline height (Flood et al., 2020; Patterson et al., 1984).

In oceanography, the upper layer (of the ocean) is called the mixed layer and reaches down to the mixed layer depth (MLD). Similar to the methods used in limnology, several methods have been proposed to determine the MLD. An intuitive method by De Boyer Montégut et al. (2004) is based on taking a reference depth known to be above the main thermocline and then taking steps downward until a certain temperature or density anomaly is found. Brenner et al. (2023) found that the density and temperature approaches perform similarly. However, its applicability is limited to the ocean MLD. Another approach was suggested by Chu and Fan (2010), who used an optimal linear fit to find the MLD in the ocean.

Similar to lakes, most oceanic methods relate to the $TSI$ method in the sense that they all rely on some form of the maximum temperature gradient.

In addition to quantitative measures of thermal stratification, lake classification has traditionally served as a qualitative tool to describe stratification behaviour. Depending on the stratification frequency and circulation pattern, lakes have historically been classified as amictic, cold monomictic, continuous cold polymictic, discontinuous cold polymictic, dimictic, warm monomictic, discontinuous warm polymictic, or continuous warm polymictic (Lewis, 1983). Boehrer and Schultze (2008) highlight the importance of correctly classifying a stratified lake, as this facilitates predictability of certain properties and generalizability of findings. This classification is based on ice coverage, annual stratification span, and mixing frequency.

## 2.2. Internal waves in lakes

The formation and forcing of a thermocline are internal, baroclinic processes. These are bounded by the fluid itself and (in part) governed by internal density gradients. Similar to the interface between air and water, internal waves on these density gradients may be excited by external forcing. These internal waves occur along isopycnals and may be observed as standing or progressive waves, similar to barotropic waves. They have distinct modes and are known to contribute to turbulence by degenerating into higher modes (Thorpe, 1973). Besides, different internal wave types (e.g., seiches, Kelvin, Pointcaré, Rossby, geostrophic) occupy distinct frequency bands. Many of these, especially in the cases of arbitrary bathymetry and/or stratification, cannot be solved analytically. Prior knowledge of the expected frequency bands for various internal wave types simplifies analysis, as not all currents and dynamics in a lake are driven by density variations and peaks in the energy spectra may well be associated with barotropic flow instead of baroclinic flow.

Several schematizations exist to facilitate the modelling of internal waves (in general). Examples include linear stratification ($\frac{\partial \rho}{\partial z} =$ constant) or $n$-layer stratification, e.g., 2-layer (Mortimer et al., 1952) or 3-layer (LaZerte, 1980). Depending on the relative portion of the water column occupied by the metalimnion, a specific number of layers may be selected. A relatively thin metalimnion (transition layer) and pronounced epilimnion (warm upper layer) and hypolimnion (cold lower layer) constitute a sharp temperature gradient and thermocline, in which case a 2-layer model suffices (LaZerte, 1980).

As mentioned, internal waves are excited when a stratified water body is forced out of hydrostatic equilibrium, constituting a balance between gravity and buoyancy (Pomar et al., 2012). An example of such a forcing mechanism is wind stress.

### 2.2.1. Wind forcing

In lake dynamics, the major acting force is wind (Stevens and Imberger, 1996; Wüest and Lorke, 2003). Conservation of momentum dictates that the wind stress balances the momentum flux into the water surface. The stress acting on the surface is split into a momentum contribution by the formation of surface gravity waves $\tau_{wave}$ and a momentum flux into the surface boundary layer (SBL) $\tau_{\text{SBL}}$ (Wüest and Lorke, 2003)

$$\tau_{\text{wind}} = \tau_{\text{SBL}} + \tau_{\text{wave}}, \tag{2.4}$$

where $\tau_{\text{wind}}$ denotes the total stress acting on the water surface, the wind stress, which is defined as (Wüest and Lorke, 2003)

$$\tau_{\text{wind}} = \rho_a C_{10} U_{10}^2, \tag{2.5}$$

where $C_{10}$ denotes the wind drag coefficient, $U_{10}$ the wind speed measured at $10\,\text{m}$ above the surface and $\rho_a$ the density of air. Several baroclinic mechanisms may be excited by wind forcing. While the net transport of water in an enclosed basin is limited to wind setup, the associated internal flow can result in significantly greater transport due to reduced gravity, increasing the tilt of isopycnals. After the wind subsides, this may give rise to the excitation of basin-scale internal waves (Wüest and Lorke, 2003).

Besides tilting, the insertion of wind momentum into the internal wave field largely happens at two distinct frequencies: the inertial frequency $f$ and the buoyancy frequency $N$ (Wüest and Lorke, 2003). Large-scale inertial motions, which carry relatively more momentum, are generated by a strong wind that persists up to half an inertial period and/or by a strong wind that suddenly changes direction (Bauer et al., 1981; Pollard and Millard, 1970). For smaller-scale internal waves near the buoyancy frequency, the forcing mechanism is more difficult to determine (Antenucci and Imberger, 2001; Wüest and Lorke, 2003). The next sections divide internal waves into basin-scale internal waves (which include seiching-like and inertial oscillations) and high-frequency internal waves, analogously to Wüest and Lorke (2003).

### 2.2.2. Basin-scale internal waves

The wind momentum transferred to the surface layer of the lake is most efficiently coupled to internal lake processes through the setup of the thermocline (Mortimer et al., 1952; Wüest and Lorke, 2003). The response of stratified lakes to wind stress consists of two phases (Mortimer et al., 1952): 1) the wind stress leads to surface set-up at the downwind, leading to set-up of the thermocline at the upwind end to maintain an internal force balance, and 2) internal seiching after the wind ceases (or changes direction). We visualize this in Figure 2.3a and b, respectively. Similarly, the first phase is forced, while the second phase is a free oscillation. While the surface setup is usually in the order of several centimetres, the setup of the thermocline can reach several meters due to reduced gravity. The subsequent internal seiching is the first example of a basin-scale internal wave. We first discuss tilting and continue with the resulting internal oscillations.

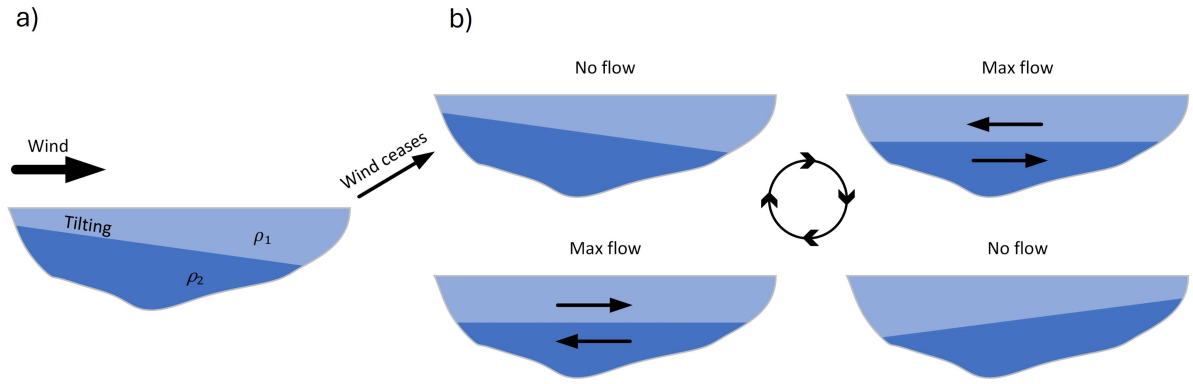


**Figure 2.3:** Schematic of the unimodal response of a 2-layer stratified lake to wind forcing. The response is divided into two phases following Mortimer et al. (1952): a) tilting of the thermocline and b) internal seiching.

Several response types exist that describe the response of the stratified interior of a lake to wind stress. If the tilting is sufficiently large for the thermocline to reach the surface, this is referred to as upwelling. Thompson and Imberger (1980) introduced the Wedderburn number to quantify this upwelling response:

$$W = \frac{h_1}{L} Ri_{\mathrm{b}} \approx \frac{g' h_1^2}{u_*^2 L} \tag{2.6}$$

with $L$ the longitudinal extent of the lake. The bulk Richardson number was used to rewrite $W$. Thompson and Imberger (1980) used this number to classify four mixing dynamic regimes: (1) homogenization through mixing, (2) interface shear and large interface displacement, (3) internal seiching, and (4) Buoyancy dominance, each with corresponding criteria in terms of $Ri$, and thus also $W$. Starting from the Wedderburn number, Imberger and Patterson (1989) introduced the Lake number. This was rewritten (right-hand side) by Kirillin and Shatwell (2016) and is defined as

$$L_N = \frac{M_{\mathrm{bc}}}{\tau_{\mathrm{wind}} A z_v} = \frac{2 h_1 St}{L \rho_0 u_*^2 z_v}, \tag{2.7}$$

where $M_{\mathrm{bc}}$ denotes the baroclinic moment about the centre of volume with lever arm $z_v$, $A$ denotes the surface of the lake, and $St$ the Schmidt stability number. Stevens and Imberger (1996) describe the Lake number as "effectively an integral equivalent to $W$". It can be used to relate stratification to basin shape and to assess the stratification stability of complex systems (Kirillin and Shatwell, 2016).

The period of persisting wind required for upwelling varies considerably between basins (see Table 1; Stevens and Imberger, 1996), with a modal response observed for wind forcing periods between $20\,\%$ to $400\,\%$ of the internal seiching period. They parameterized the time required for upwelling as

$$T_{\mathrm{u}} = \frac{T_1}{2\pi} \arccos\left(1 - W\right), \tag{2.8}$$

where $T_1$ is the mode-1 internal seiching period. They also used the Wedderburn number and Lake number to quantify upwelling regimes:

1. $W >> 1$ $L_N >> 1$ Small-amplitude internal seiching.
2. $W < 1$ $L_N >> 1$ Mode-2 response, with a predictable upwelling time.
3. $W >> 1$ $L_N < 1$ Deep seiching with no upwelling.
4. $W << 1$ $L_N << 1$ Large-scale tilting, especially if wind persists for $\frac{1}{4}T_1$.

After the wind subsides, the system moves back towards hydrostatic equilibrium, overshoots, and oscillates until the momentum is dissipated. At the surface, this leads to the well-known seiching phenomenon (Battjes and Labeur, 2017), which coexists with internal seiching of the lake interior. The period of a uninodal seiche in a (shallow) stationary 2-layer fluid has historically been described by the Merian or Watson formula (Watson, 1904)

$$T_1 = \frac{2L}{c}, \tag{2.9}$$

with

$$c^2 = g' \frac{h_1 h_2}{h}, \tag{2.10}$$

where $h_2$ denotes the thickness of the second layer from the top (and in the case of a 2-layer system also the bottom layer). This response is the same for barotropic and baroclinic flows. However, the large differences in density ($\rho_1 << \rho_2$) and layer height ($h_1 >> h_2$) of barotropic seiching reduce the barotropic wave celerity to $c_{\mathrm{bt}} = \sqrt{g h_2}$. Since $g'$ and $g$ usually differ by three orders of magnitude, the wave celerity of barotropic seiching is at least an order of magnitude larger than the wave celerity of baroclinic seiching, with typical periods of $20\,$minutes and $15\,$hours, respectively (Battjes and Labeur, 2017; Stevens and Imberger, 1996). Observations of the latter show an especially large range due to the sensitivity to not only length but also the density profile. Gill (1982) describes the solution method to find the nodal structure of vertical velocity (and phase velocity) for each mode in the case of arbitrary stratification. The solution consists of numerically solving the equations for the complex amplitude of the vertical velocity (Gill, 1982; Simpson et al., 2021)

$$\frac{d^2\psi}{dz^2} + \frac{N^2\left(z\right)}{c^2}\psi = 0, \tag{2.11}$$

where $\psi$ is the complex amplitude of the vertical velocity. The stratified fluid is divided into layers and each mode is solved separately, where the eigenvalue of mode $n$ is the phase velocity $c_n$. Subsequently, Equation (2.9) can be used to determine the corresponding period. In that case, $L$ should be the effective basin length, which is often initially estimated and subsequently validated from data (Simpson et al., 2021).

The discussed, basin-scale internal seiching manifest as standing waves. Standing waves are prominent in small lakes where Coriolis force is negligible (Wüest and Lorke, 2003). With increasing lake

size and latitude, the Coriolis force is no longer negligible and internal seiches affected by Coriolis may degenerate into Kelvin or Poincaré waves (Antenucci et al., 2000; Csanady, 1967; Valipour et al., 2015; Wüest and Lorke, 2003). The former propagates along the coast, while the latter manifests in the central, deeper parts of a lake. The periods of both may be sub- or super-inertial and are solved numerically for arbitrary bathymetries (Hodges et al., 2000; Ou and Bennett, 1979; Valipour et al., 2015).

Whether Coriolis forces influence a barotropic flow is indicated by the Rossby number, representing the balance between inertial forces and Coriolis forces. The external Rossby radius of deformation further indicates the flow's sensitivity to Coriolis effects: when the flow scale exceeds this length, Coriolis forces become significant. In practice, this is found mainly in the ocean. Analogously, the internal Rossby radius (of deformation) indicates whether an internal flow is influenced by Coriolis forces. The internal Rossby radius is defined as (Wüest and Lorke, 2003)

$$L_R = \frac{c}{f}, \tag{2.12}$$

where $c$ denotes the internal wave celerity and

$$f = 2\Omega \cdot \sin\phi \tag{2.13}$$

is the inertial frequency with $\Omega = 7.29 \times 10^{-5}$ rad/s is the frequency of Earth's rotation and $\phi$ is the latitude. The influence of Coriolis forces is then assessed by comparing these wavelengths to the dimensions (width or length) of the lake. Additionally, this length scale may be inserted into Equation (2.12) to arrive at the internal Burger number (Flood et al., 2020; Valipour et al., 2015)

$$S_i = \frac{c}{fL}, \tag{2.14}$$

which effectively normalizes the internal Rossby radius with the length scale of the lake. Quantitatively, Antenucci et al. (2000) reported the influence of Coriolis when the internal Rossby radius is half of the basin width ($S_i = 0.5$). While barotropic flows in lakes are typically unaffected by the Coriolis force, baroclinic flows are often influenced due to the slower phase speeds of internal waves compared to surface waves.

Besides internal seiching and its Coriolis-induced degenerations, other basin-scale internal waves exist.

- Inertial currents are Coriolis-affected, circular currents within the ocean and most large lakes (Wüest and Lorke, 2003). They rotate at (or just below) the inertial frequency and stem from the geostrophic adjustment after wind (Bauer et al., 1981). In the ocean, D'Asaro (1985) found that the shear between the mixed layer and the ocean body is mainly contained in the inertial frequency. This is due to wind-forced inertial currents "slipping" more easily along a pycnocline than along the bottom (Bauer et al., 1981). In many lakes of medium size, the distinction of basin-scale seiching and its derived wave types from inertial currents is complicated by the similarity in their wave period, which is typically around $15$ hours.
- Sub-inertial topographic Rossby waves are generated by gradients in potential vorticity. These gradients are found at large bed-level gradients ($f/h$) but are rarely observed in lakes (Wüest and Lorke, 2003).

### 2.2.3. High-frequency internal waves

Besides inertial and basin-scale internal oscillations, a short-wave peak is often observed in the energy frequency spectrum in the metalimnion. This peak is prevalent after wind forcing (Wüest and Lorke, 2003) and usually occurs near the buoyancy frequency

$$N^2 = -\frac{g}{\rho_0}\frac{\partial\rho}{\partial z}, \tag{2.15}$$

where $\rho_0$ denotes the average density between discrete layers or over a certain range. The exact mechanism through which these are energized is unknown (Wüest and Lorke, 2003), but they may

be excited directly through wind (Antenucci and Imberger, 2001) or by internal seiches degenerating into higher modes (Boegman et al., 2005; De Carvalho Bueno et al., 2023). The latter mechanism is generally negligible compared to the energy that is dissipated through the nonlinear steepening of internal seiches (De Carvalho Bueno et al., 2023). Besides, the contribution to the total energy of the internal wave spectrum is usually limited, with propagating high-frequency internal waves contributing up to $1\,\%$ of this energy to the spectrum (Boegman et al., 2003).

## 2.3. Underwater acoustics in the presence of stratification

Acoustic measurements have long been an important aspect of oceanic and limnologic measurements. Their main advantage is the increased spatial and temporal resolution compared to traditional means of measuring stratification, e.g., CTD-profiles (Lavery and Ross, 2007). Furthermore, they provide a non-intrusive means of continuously measuring full velocity profiles, as opposed to traditional methods that collect point measurements, e.g., Pitot tubes.

Acoustic measurements rely on the transmission of acoustic pulses, which are reflected and subsequently recorded. These pulses can be received from a small single control volume (acoustic Doppler velocimeter; ADV), a large area (acoustic backscatter sensor; ABS), or multiple successive control volumes (ADCP). Depending on the system, they use either a single receiver (ABS) or multiple receivers (ADV, ADCP). A single receiver only measures backscatter intensity, while multiple receivers enable the measurement of Doppler shift, which can be used to determine velocity profiles across the water column (Ton et al., 2020). While velocity measurements are well-established, even in stratified conditions, the study of backscatter remains an active area of research.

Acoustic (backscatter) methods are divided into forward and inverse methods. Forward methods are used to predict backscatter based on measured or assumed properties of the scatterer, while inverse methods are used to derive properties of a scatterer based on measured backscatter. Backscatter-affecting quantities include bubbles, turbulence, density gradients, suspended sediment, and biota. These quantities may be modelled forwardly, while inverse modelling often requires additional sets of assumptions, such as (frequency-dependent) dominant scattering mechanisms (Bassett et al., 2023).

Backscattering of acoustic signals by density gradients was proposed by Munk and Garrett (1973). This was hypothesized to be due to the dependence of the speed of sound in water on salinity and temperature. Since then, pycnoclines have been measured many times using acoustic instruments. Important contributions include Gupta (1965, 1966) who created a scattering model, which was subsequently used by Penrose and Beer (1981) who conducted measurements of a salt wedge in a low-dynamic estuary and concluded that scattering occurred due to the presence of a pycnocline.

The guiding principle of acoustically measuring a pycnocline is the echo reflection by large gradients in the speed of sound or density (Munk and Garrett, 1973; Penrose and Beer, 1981). This is accompanied by backscatter from other passive tracers, such as bubbles (Bassett et al., 2023; Li et al., 2009), biota (e.g., plankton, fish; Lavery et al., 2007; Warren et al., 2003), suspended sediment, and turbulent microstructure (Brenner et al., 2023; Penrose and Beer, 1981). The relative importance of these scatterers varies per situation and depends on their concentrations and, in the case of a pycnocline, its thickness and the magnitude of the sound speed/density gradient. Specifically measuring a pycnocline through sound speed and density gradients alone requires a sharp gradient (Ross and Lavery, 2011), so measurements in estuarine environments at the interface between salty sea and fresh fluvial waters are the predominant application (Bassett et al., 2023; Penrose and Beer, 1981). However, the attribution of backscatter to stratification is often complicated by the common aggregation of biota or suspended sediment on pycnoclines due to reduced mixing, so this attribution has predominantly been done in environments where density stratification is the dominant (or only) scattering mechanism (e.g., thermohaline staircases; Shibley et al., 2020).

Acoustic backscatter is commonly expressed using reflection coefficients (Ross and Lavery, 2011; Weidner et al., 2020), representing the ratio between the scattered pressure wave ($p_{\text{scat}}$) and the incoming pressure wave ($p_{\text{inc}}$). Reflection coefficients over depth and time constitute an echogram, which principally shows the echo intensity over time. Echo intensity reaches a maximum at the interface core (Shibley et al., 2020). Reflection coefficients are defined as

$$R_{n,n+1} = \frac{\rho_{n+1}c_{s,n+1} - \rho_n c_{s,n}}{\rho_{n+1}c_{s,n+1} + \rho_n c_{s,n}} = \frac{\eta_{n+1} - \eta_n}{\eta_{n+1} + \eta_n}, \tag{2.16}$$

where $R_{n,n+1}$ denotes the reflection coefficient between layer $n$ an $n+1$, $c_s$ denotes the speed of sound, and $\eta$ denotes the acoustic impedance ($\eta = \rho c_s$). Predicting reflection coefficients is beneficial for researching the feasibility of acoustically measuring a pycnocline and for inversely deriving properties of this pycnocline, such as the presence of passive tracers (e.g., plankton) or other water properties (Ross and Lavery, 2011).

The speed of sound in water greatly depends on the temperature, salinity, and pressure in water. Extensive research on this parameterization was performed by Chen and Millero (1977, 1986), the former focusing on seawater and the latter on fresh lake water. This relation is given in Appendix A and plotted in Figure 2.1b. It is observed that temperature fluctuations have a more pronounced effect on the speed of sound than salinity fluctuations. Conversely, acoustic impedance $\eta$, being a product of density and sound speed, is equally affected by temperature and salinity in the relevant ranges (see Figure 2.1c). This disagrees with Ruddick et al. (2009), who states that impedance is dominated by temperature, and it can be concluded that the dominant source of stratification governs the dominant acoustic scattering mechanism in a stratified body of water.

### 2.3.1. Modelling acoustic backscatter by stratification

Lavery and Ross (2007) developed and tested a scattering model to predict acoustic backscatter by double-diffusive interfaces. Based on this, Ross and Lavery (2011) created a scattering model for oceanic pycnoclines. This model does not make assumptions regarding the processes involved in creating and maintaining a pycnocline and is based on backscatter from density and sound speed gradients. It is summarized by

$$\frac{p_{\text{scat}}}{p_{\text{inc}}}(r_{\text{scat}}) = \frac{1}{2} \sum_{n=r_{\text{scat}}/\Delta - N_{\text{sub}}/2}^{r_{\text{scat}}/\Delta + N_{\text{sub}}/2} \frac{R_{n,n+1} \exp\left(2i \sum_{m=r_{\text{scat}}/\Delta - N_{\text{sub}}/2}^{n} k_m \Delta\right)}{\left(n + \frac{N_{\text{sub}}}{2} + 1\right) \Delta / r_{\text{scat}}}, \tag{2.17}$$

and

$$S_v = 10 \log_{10} \left( \frac{\left(\frac{p_{\text{scat}}}{p_{\text{inc}}}\right)^2}{2\pi L_e (1 - \cos\theta_{1/2})} \right), \tag{2.18}$$

where $\Delta$ is the thickness of the homogeneous sublayers, $N_{\text{sub}}$ is the number of sublayers, $k$ is the acoustic wavenumber, and $r_{\text{scat}}$ is the range to the pycnocline. Furthermore, $p_{\text{scat}}$ and $p_{\text{inc}}$ denote the scattered and incoming pressure at the thermocline, respectively, $S_v$ denotes the volume scattering strength, $L_e$ is an integration length scale, and $\theta_{1/2}$ denotes half of the conical beam angle. This model is based on an assumed scattering volume of $r_{\text{scat}}^2 \cdot 2\pi L_e (1 - \cos\theta_{1/2})$.

Similarly, Weidner and Weber (2021) created an acoustic scattering model for weakly scattering stratification structures. They divide backscatter by changes in impedance into a contribution by density gradient and sound speed. Sound speed tends to dominate, especially in temperature-dominated stratified systems. This allows for the exclusion of several, smaller order terms. One of the key assumptions is that the acoustic source is far from the scattering interface, allowing the approximation of the incoming pressure wave as locally planar. Furthermore, the spatial variability of the thermocline (and its oscillations) should then be small compared to the area ensonified by the echo beams. They express the scattered pressure as

$$p_{\text{scat}}(r = 0) = -i \int \hat{p}_{\text{inc}} e^{-2ikr'} \Delta k \, \mathrm{d}r', \tag{2.19}$$

where $\hat{p}_{\text{inc}}$ is the amplitude of the incoming pressure wave and $r'$ is the range over the stratification structure. Interestingly, the model by Weidner and Weber (2021) looks very similar to a continuous

version of the discrete layer model by Ross and Lavery (2011). However, Bassett et al. (2023) questions the validity of both (and other) models, especially at short ranges. At these scales, waves may not be normally incident and therefore not planar. Furthermore, the range dependency of acoustic signals (e.g., frequency-dependent attenuation) is often uncertain, which impacts the validity of predicted backscatter coefficients.

### 2.3.2. Existing methods for acoustic measurements of stratification

A pycnocline can be measured in several ways: variations in acoustic impedance as seen in the backscatter intensity (Ross and Lavery, 2011), through velocity measurements, or both (Brenner et al., 2023; Macrander et al., 2007). Accordingly, Macrander et al. (2007) discriminates two methods of interface detection: the “maximum current shear method” and the “maximum backscatter method”. These methods generally correspond well but the absence of suspended particles in the water column significantly affects the backscatter method. In the following section, both methods are discussed. The result can ultimately be combined into a single time series. To this end, Brenner et al. (2023) firstly identified the periods in which specific data would prove unusable due to external factors. Afterwards, periods where multiple time series overlap were combined using weighted averages with weights determined by the ratio of peak prominence and the minimum peak threshold. However, using weighed averaging requires prior verification of both derived time series, which is not always available.

#### Acoustic backscatter methods

Echsounders have been used extensively to measure interfaces due to the scattering potential of several features in the water column. One of the earlier efforts of measuring stratification through narrowband echosounding at high frequencies was by Fisher and Squier (1975), who used an $87.5$ kHz narrowband echosounder to observe internal waves off the coast near San Diego. Since then, many observations have been made with broadband and narrowband echosounders. Of the previously mentioned scatterers, turbulent microstructure (Bassett et al., 2023; Duda et al., 2016; Lavery and Ross, 2007; Lavery et al., 2013; Ross and Lavery, 2010), density gradients or interfaces (Bassett et al., 2023; Duda et al., 2016; Fisher and Squier, 1975; Li et al., 2009; Penrose and Beer, 1981; Ruddick et al., 2009; Stranne et al., 2017; Weidner et al., 2020), suspended sediment (Bassett et al., 2023; Lavery et al., 2013), and biota (Macrander et al., 2007; Ross and Lavery, 2010; Weidner et al., 2020) are often associated with pycnoclines, because they directly constitute stratification (i.e., density gradients, turbulent microstructure), congregate on pycnoclines (i.e., suspended sediment, biota), or differ between the separated layers (i.e., turbulence, biota, suspended sediment). For example, interfaces are typically associated with the congregation of plankton (Haught et al., 2024; McManus et al., 2005) and turbulent instabilities (Lavery et al., 2013), which may be used as a proxy for the interface height. While this complicates quantifying isolated scattering mechanisms, their coincidence also means that quantification is not always required for deriving the interface height. However, validating the association between the dominant scatterer and the interface height is essential to ensure that they do, in fact, coincide.

The interface height is derived from relative acoustic backscatter, where global maxima (Macrander et al., 2007) or local maxima (Brenner et al., 2023) indicate the presence of a density interface. The latter used a minimum threshold and a three-point stencil to find the location of the peak. The three-point stencil serves to avoid confinement to the cells in which the water column was divided. Similarly, peaks in reflection coefficients (as determined through Equation (2.22)) may indicate the presence of an interface (Shibley et al., 2020; Weidner et al., 2020). These peaks also usually manifest as local maxima. Shibley et al. (2020) also adapted a minimum threshold, and two other criteria that mainly relate to the thermohaline staircase structure. Identifying peaks may be done visually (Stranne et al., 2017) or automatically (Shibley et al., 2020) but automated approaches require visual inspection to exclude outliers produced by fish, anthropogenic sources, and “multiple scattering”-phenomena (Bassett et al., 2023). These methods all rely on local backscatter maxima, pointing to the (sometimes implicit) assumption of scattering by density gradients or by the aggregation of constituents on the density interface (Haught et al., 2024; Lennert-Cody and Franks, 1999; McManus et al., 2003). In the absence of local maxima, separated water masses may exhibit different backscatter entirely (McManus et al., 2003; Warren et al., 2003). The interface is then better represented by a large vertical gradient in backscatter rather than a local maximum.

Echosounders operate across a wide frequency range, from hundreds of Hertz to several megahertz,

**Table 2.1:** Theoretical acoustic sensitivity. Adapted from Daugharty (2024), who derived it from Jaarsma (2023).

| Frequency | Theoretical resolvable particle size ($D_{\text{min}}$ to $D_{\text{peak}}$) |
|---|---|
| 3000 kHz | 8.0 to 160 µm |
| 2000 kHz | 12 to 240 µm |
| 1000 kHz | 24 to 480 µm |
| 500 kHz | 48 to 960 µm |
| 250 kHz | 96 to 1910 µm |

all of which have been used to measure stratification. The chosen frequency is often an optimization of resolution, attenuation, and the measured quantity. Both resolution and attenuation increase with frequency, limiting the application of high-frequency signals (i.e., MHz) to small depths. The measured quantities (or scatterers) have distinct acoustic frequencies at which backscatter is highest. For instance, bubbles reflect relatively low-frequency signals of $\mathcal{O}(10\text{–}100)$ kHz, while zooplankton contributes more at frequencies above $500$ kHz (Bassett et al., 2023; Penrose and Beer, 1981). It is important for an echosounder to cover the frequency bands of interest when measurements are conducted. Bassett et al. (2023) argue for the use of multiple frequencies, each at a bandwidth comparable to the scatterer-specific characteristic frequencies, to provide a full image of distinct scattering mechanisms present at a site. These frequencies largely depend on the corresponding resulting particle sizes, which are summarized in Table 2.1, where $D_{\text{min}}$ and $D_{\text{peak}}$ correspond with the minimum required diameter for scattering and the diameter associated with maximum scattering, respectively.

The frequency dependence of scatterers is commonly represented through spectral slopes, which describe echo intensity as a function of frequency. Differences in impedance and size cause scatterers to exhibit distinct frequency-dependent backscatter, which we can quantify by measuring across multiple frequencies. This can be achieved using discrete frequencies (i.e., narrowband Warren et al., 2003), a continuous frequency band (i.e., broadband; Stanton et al., 1994), or multiple continuous bands (Bassett et al., 2023; Lavery et al., 2007). Accurate backscatter measurement in these approaches requires proper calibration.

Echosounders are operated in either narrowband or broadband mode (also referred to in the literature as “frequency-modulated”). Narrow-band echosounding uses a single frequency for each pulse and at each pulse transmission, while broadband sends out pulses at different frequencies over a spectrum. Broadband echosounding facilitates inverse methods since inversion of properties can now be performed on a range of frequencies which is more likely to include the characteristic frequency or frequencies associated with a scatterer (Bassett and Zeiden, 2023; Lavery et al., 2017) and allows for spectral slope computation over a frequency band. Furthermore, broadband echosounding increases the resolution through pulse compression techniques. Calibration and post-processing, however, are more complex compared to narrowband echosounding (Lavery et al., 2017) and the chance of sidelobe interference increases (Nortek Support, 2022). Both modes have been extensively used to measure stratification but, recently, the focus has shifted mostly to broadband echosounding (Lavery et al., 2017).

Acoustic measurements rely on the emittance and reception of an acoustic pulse that propagates through the water column. As explained, this pulse is attenuated and reflected by a wide variety of scatterers moderating its amplitude and frequency. Upon reception by the device, it is recorded as a power level $P_r$ (Bassett and Zeiden, 2023). This should be corrected for several attenuation factors, such as absorption and spherical spreading. It is converted to, depending on the nature of the scatterer, volume backscatter (also called volume backscattering strength; Bassett and Zeiden, 2023; Brenner et al., 2023; Gostiaux and Van Haren, 2010)

$$S_v = P_r + 20\log_{10} r + 2\alpha r - PL - 10\log_{10}\frac{c\tau_{\text{pulse}}}{2} - \Psi + G_{\text{int}} \tag{2.20}$$

or target strength (Bassett and Zeiden, 2023)

$$TS = P_r + 40\log_{10} r + 2\alpha r - PL + G + B(\theta). \tag{2.21}$$

Here, $r$ is the range from the ensonified target or area to the transducer, $PL$ is a reference power level, $c\tau_{\text{pulse}}/2$ is the pulse length with $\tau_{\text{pulse}}$ the pulse duration, $\Psi$ is the equivalent beam angle, and $G$ and $G_{\text{int}}$ are calibration terms. $\alpha$ is a frequency-dependent coefficient related to water properties that influence attenuation, which generally increases with frequency (Bassett and Zeiden, 2023; Brenner et al., 2023). Split beam echosounders require the inclusion of a beam directivity term, $B(\theta)$, which is a localization term for targets in the ensonified volume, but this term is omitted here. Finally, a noise threshold $NT$ can be included, which is subtracted in the linear domain, replacing $P_r$ in Equation (2.20) and Equation (2.21) with $10\log_{10}\left(10^{P_r/10} - 10^{NT/10}\right)$. This term depends on environmental conditions and is generally not known beforehand. It may therefore initially be omitted and corrected for later (see Section 3.2.2).

Generally, the choice of using either $S_v$ or $TS$ depends on the measurable. $S_v$ is used for multiple targets (e.g., gradients in impedance, double-diffusive interfaces), integrating over the ensonified volume, while $TS$ is used for discrete targets (e.g., fish). Whether $S_v$ and $TS$ can be accurately computed largely depends on the availability of calibration. If not, any attempt at inverse modelling of temperature or reflection coefficients is unfeasible, but localizing the thermocline is still possible through maximum backscatter (gradient) approaches using $S_v$. In that case, $S_v$ and $TS$ are referred to as relative volume backscatter and relative target strength, respectively. The target strength is related to the reflection coefficient by (Shibley et al., 2020; Stranne et al., 2017)

$$R = 10^{(TS - 10\log_{10} A)/20}, \tag{2.22}$$

where $A$ is the ensonified area at a distance $r$ from the transducer. $A$ is defined as

$$A(r) = \pi\left(r\tan\theta_{1/2}\right)^2. \tag{2.23}$$

Finally, the target strength and volume backscatter are related through

$$\begin{aligned} \sigma_v &= \rho_v \sigma_{bs} \\ S_v &= 10\log_{10}\rho_v + TS, \end{aligned} \tag{2.24}$$

where $\rho_v$ is the volumetric density of targets in the beam, $\sigma_v$ is the volume backscattering cross-section (which is the linear form of $S_v$), and $\sigma_{bs}$ is the backscattering cross-section (which is the linear form of $TS$). This shows how $S_v$ is used for volumes and $TS$ for discrete targets (Bassett and Zeiden, 2023; Maclennan et al., 2002). The literature on echosoundering is generally inconsistent in the definitions and units used, with values often conveniently reported in decibels [dB]. While these units should be expressed as dB re $1\,\text{m}^{-1}$ (Maclennan et al., 2002), we will follow the convention of most studies and use dB throughout this work.

In practice, typical practical parameters of interest regarding echosounding are: blanking distance, cell/bin size, and pulse length. Furthermore, the instrument-specific beam width determines the ensonified area, where a wider beam width provides greater spatial coverage but reduces resolution, especially at greater depths. These parameters are defined in Chapter 3, but their contributions to measuring thermal stratification are not researched and are taken at face value instead.

### Velocity methods

Increased stratification is often associated with increased velocity shear (Simpson et al., 2021). Conversely, a region of maximum stratification or pycnocline may be identified through regions of increased shear (Brenner et al., 2023). Under the assumption that the stratification is approximately horizontal, this reduces to vertical shear, which is defined as

$$\left(\frac{\partial \vec{u}}{\partial z}\right)^2, \tag{2.25}$$

where $\vec{u}$ is the horizontal velocity vector.

Currents in lakes are affected by many external forces and are inherently of many different scales. It is thus unlikely that the global maximum in vertical shear consistently represents the location of a pycnocline. Furthermore, when external forcing such as wind persists for an extended period, the large velocity gradients—and consequently the shear—subside. Following the initial response of a two-layer system to wind forcing, the system eventually reaches a steady state (Mortimer et al., 1952; Stevens and Imberger, 1996). At this point, the system comprises two rotating cells with a continuous velocity distribution between them. In such a case, the maximum vertical shear is unlikely to align with the interface between the layers. Instead, since the shear profile reverses direction where the cells rotate in opposite directions, the interface is more likely to coincide with the inflexion point of the shear distribution.

Knowledge of the frequency bands with which a pycnocline is associated facilitates the identification of shear that could help localize it. For example, in the ocean, the shear between the mixed layer and the ocean body is mainly contained in the inertial band (D'Asaro, 1985; Brenner et al., 2023; Chaudhuri et al., 2021; Pollard and Millard, 1970). In thermally stratified lakes, it is mainly contained in the first and second internal seiche modes (Simpson et al., 2011, 2021). They used co-spectra of measured velocities at different depths to confirm the theoretical frequencies of the first two internal seiche modes and showed the coincidence of vertical shear and stratification. This vertical shear was not limited to the internal seiche band but included the entire spectrum. They also found that the general area of the thermocline was well indicated by the $24$-hourly magnitude of the vertical shear. The isolation of specific frequency bands is not always necessary. For example, strong currents at the Denmark Strait Overflow did not require Macrander et al. (2007) to limit themselves to certain frequencies, since the flow is dominated by the current separated by the pycnocline.

## 2.4. Case study: Lake Veere

In this section, we include a brief discussion of the relevant characteristics of Lake Veere. We discuss basin geometry, the previously known aspects of (seasonal) stratification, and biota (i.e., plankton, fish).

### 2.4.1. Basin geometry

Lake Veere stands out from freshwater lakes due to its remaining estuary-like features. It has an average depth of $4.8$ meters and a maximum depth of $23$ meters. Its surface area varies between $2342$ ha in the winter and $2195$ ha in the summer. Deep ($> 8$ m), intermediate ($4$–$8$ m), and shallow ($< 4$ m) parts constitute around $22$ %, $25$ %, and approximately $50$ % of the surface area, respectively.

Joosten (2021) divides Lake Veere into eight different areas. The researched areas, which are located in the northwest, are the widest. The shores are lined with abundant vegetation and various buildings. It is characterized by a section of deep waters (see Figure 1.1b) and contains the longest stretch for northeastern (or southwestern) winds. The northwest of Lake Veere is located at a latitude of $51.58°$.

We identify several sections in the northwest corner of Lake Veere (see Figure 1.1 or refer ahead to Figure 3.1). Overall, the width across the lake is between $1$–$1.5$ km. A long, narrow (ex-)tidal channel is observed along the southwestern shore. This channel is the deepest and longest, containing several especially deep sections of $22$ meters. It has a length and width of approximately $2500$ meters and $250$ meters, respectively. Two adjacent areas of deeper waters are found at the north(east) side of this channel. These are separated from the channel by depths of $10$–$12.5$ meters and reach depths of $15$–$17.5$ meters and their horizontal dimensions are in the order of several hundred meters. Finally, a large, deeper section is found a little further to the east. It reaches depths up to $20$ meters and has horizontal dimensions of around $500$ meters.

### 2.4.2. Stratification and internal processes

The annually averaged salinity in Lake Veere is around $25$–$30$ PSU, which is lower than the neighbouring Eastern Scheldt due to the limited discharge through the flush gate. The water temperature varies between $0.5\,°$C and $24\,°$C. The restricted inflow and outflow through Katse Heule ($< 40\,\mathrm{m}^3$/s) results in a tidal range of approximately $7$ cm (Van der Kaaij and Kerkhoven, 2021; Prins et al., 2015, 2024).

As discussed in Chapter 1, a seasonal thermocline develops in Lake Veere, with typical temperature

differences of $2$–$3\,^{\circ}$C and corresponding density variations of $1$–$2\,$g/L (Prins et al., 2023). Additionally, heavy saline water from the Eastern Scheldt infiltrates the lake, leading to near-bed salinity increasing from west to east towards the sluices (Van der Kaaij and Kerkhoven, 2021). This denser water may accumulate in deeper areas, causing density differences of up to $3\,$g/L. The relative contributions of temperature and salinity to stratification likely vary over time and with depth in the water column (Van der Kaaij and Kerkhoven, 2021).

Based on the criteria by Lewis (1983) and the system analysis by Prins et al. (2024), we find that Lake Veere should be classified as discontinuous warm polymictic. This entails the absence of seasonal ice cover, periods of stratification lasting days or weeks, and multiple mixing events throughout the year. It also entails the absence of a fully continuous seasonal stratification. This implies complete mixing occurs at least once during the main heating season (Kirillin and Shatwell, 2016), which is also the case for Lake Veere (in the summer of 2024).

Circulation models indicate a long water residence time in the northwest, though this was not considered the primary driver of hypoxia compared to the decomposition of organic material on a sub-yearly timescale (Prins et al., 2023). On a shorter timescale (i.e., wind-driven processes) circulation in Lake Veere remains largely unknown. Beyond seiching, more complex wind-driven circulation patterns are likely to emerge due to the estuarine bathymetry, as observed in Haringvliet (Kranenburg et al., 2023).

### 2.4.3. Biota

Phytoplankton measurements were conducted in Lake Veere between 1990 and 2003 before its reconnection with the Eastern Scheldt, but not much is known about the current state of plankton concentration and composition. Then, most phytoplankton types had sizes of order $10\,$µm (Wetsteyn, 2004a). Zooplankton concentrations were generally low at the surface, especially during the summer, but increased towards the bed with large contributions of microzooplankton ($< 20\,$µm; Wetsteyn, 2004b). We expect the commissioning of Katse Heule in 2003 to have had a significant effect on the plankton composition, so new measurements are desirable.

Most primary production (phytoplankton) is concentrated in the upper $6\,$meter of the water column where light can penetrate, generally above the hypothesized thermocline depth ($5$–$10$ meters; Prins et al., 2023, 2024). Chlorophyll concentrations—a general indicator of phytoplankton—peak between April and September in line with an increase in temperature and insolation (Lewandowska et al., 2012; Prins et al., 2024).

While data is available on the fish species in Lake Veere, we do not know of any trends or developments on a sub-yearly timescale (Prins et al., 2023; Van Rijsen et al., 2022). We therefore exclude them from analysis as much as possible.

## 2.5. Conclusions

Seasonal thermal stratification is characterized by variability in the thermocline height and strength. This is best characterized using gradient-based methods, such as the $TSI$ method, but may require more robust methods in the presence of noise or complex layered structures. Findings regarding the evolution of seasonal stratification may be generalized using the discussed lake classification methods, which aid in relating results to the corresponding field of research.

The research into the internal dynamics has resulted in the identification of several important frequencies. The inertial frequency is readily determined, the buoyancy frequency requires measurements, and internal seiching modes require numerically solving Equation (2.11) and/or additional numerical simulation. These should be validated through measurements since the effective basin length remains an initial estimate. Simpson et al. (2021) researched internal seiching using ADCPs and conducted a spectral analysis (of velocities) to identify major seiching frequencies. Instead of using velocities, a sharp interface may be used directly for spectral analysis (e.g., Saggio and Imberger, 2001). Furthermore, Antenucci et al. (2000) researched the presence of internal waves under the influence of Coriolis. Their research provides a good framework to use for frequency analysis in lakes.

Strong stratification has been frequently measured using narrowband echosounders, but the popularization of broadband echosounders has recently occupied most research. While the frequency de-

pendence of backscatter by stratification has been modelled, its validation has been limited. Multi-frequency echosounding provides opportunities for researching the frequency-dependence of backscatter. Since impedance is predominantly influenced by temperature, thermally stratified, low-dynamic sites are a good contender to isolate backscatter by impedance gradients. This also constitutes the largest research gap. Acoustic backscatter has seen many applications in oceanographic research to measure the mixed layer depth and double-diffusive interfaces, but few in limnologic research. The small density gradients and the limited presence of scatterers (in relation to the range resolution) have complicated this research. The continuous tracking of interfaces through the multi-mode approach by Macrander et al. (2007) presents an opportunity to monitor thermal stratification at a high spatial and temporal resolution while also leveraging all the measurements that can be obtained with conventional ADCPs.

Uncalibrated acoustic measurements have limited quantitative use, but Gostiaux and Van Haren (2010) and Brenner et al. (2023) provide helpful methods leveraging these as well as possible for the analysis of stratification. Shibley et al. (2020) provides a good framework for the tracking of thermal interfaces. Furthermore, backscatter models (Ross and Lavery, 2011; Weidner et al., 2020) may provide insights into the theoretical reflection coefficients when presented alongside volume backscatter, even if this backscatter is not converted to reflection coefficients, which would require calibration. To this end, Bassett et al. (2023) provides methods and acoustic processing techniques to facilitate qualitative comparisons, while also identifying individual scattering mechanisms.

The above-described relations are summarized in the conceptual framework shown in Figure B.1.

# 3 Methodology

This chapter outlines the methodology used to research the feasibility of measuring seasonal thermal stratification in a low-dynamic former estuary. This has not been measured through acoustic backscatter before, emphasizing the explorative nature of this research. The process is guided by the main research question: “To what extent can thermal stratification and corresponding baroclinic motions be measured with acoustic instruments in Lake Veere?”

During the summer of 2024, we collected in Lake Veere. We complemented the usual fortnightly TSO measurements with continuous temperature measurements by three moorings equipped with temperature sensors and acoustic measurements by two Nortek Signature1000 ADCPs. Furthermore, we joined three TSO measurement campaigns to obtain high-resolution CTD data using a CastAway-CTD at the regular TSO locations and a few additional locations. We provide a complete overview of measurement campaigns in Table 3.1. The locations of the moorings, the ADCPs and the CTD casts are shown in Figure 3.1.

We determine the depth and presence of the thermocline through two approaches. Firstly, we use direct measurements to infer a thermocline height. Then, we infer the thermocline height from the acoustic backscatter. We do this by first characterizing periods of stratification and analyzing the associated backscatter, to relate theoretical backscatter (by impedance gradients as computed from the CTD profiles) and measured backscatter. Finally, we compare the results of the acoustic method to the actual thermocline depth obtained from temperature measurements.

After characterizing periods of stratification and creating a time series of the thermocline height, we proceed with spectral analysis to isolate specific frequency components. We can then relate peaks in the spectral density to theoretical frequencies, considering inertial, basin-scale, and high-frequency internal waves. We use this to identify periods where internal flow is present. The flow velocities during these periods are then analyzed to find flow directions and phase differences above and below the thermocline.

Generally, we first discuss the inference of thermocline height (RQ3) and then discuss the observations of internal flow that are facilitated by this method (RQ4). We structure the methodology as follows. Firstly, we discuss the measurement campaigns, processing, and inference of stratification for the direct in Section 3.1 and for the acoustic measurements in Section 3.2. We then analyze the frequency components in the obtained thermocline height time series to find internal oscillations in Section 3.3.

**Table 3.1:** Overview of the measurement period. The moorings and ADCPs measured continuously during this period. We collected CTD casts during three measurement campaigns.

| Date | Device | Device name(s) |
|---|---|---|
| 03-06-2024 – 06-09-2024 | Temperature moorings | Mooring 1<br>Mooring 2<br>Mooring 3 |
| 03-06-2024 – 06-09-2024 | Nortek Signature1000 | ADCP3<br>ADCP6 |
| 24-06-2024,<br>22-07-2204,<br>05-09-2024 | Sontek CastAway-CTD | - |

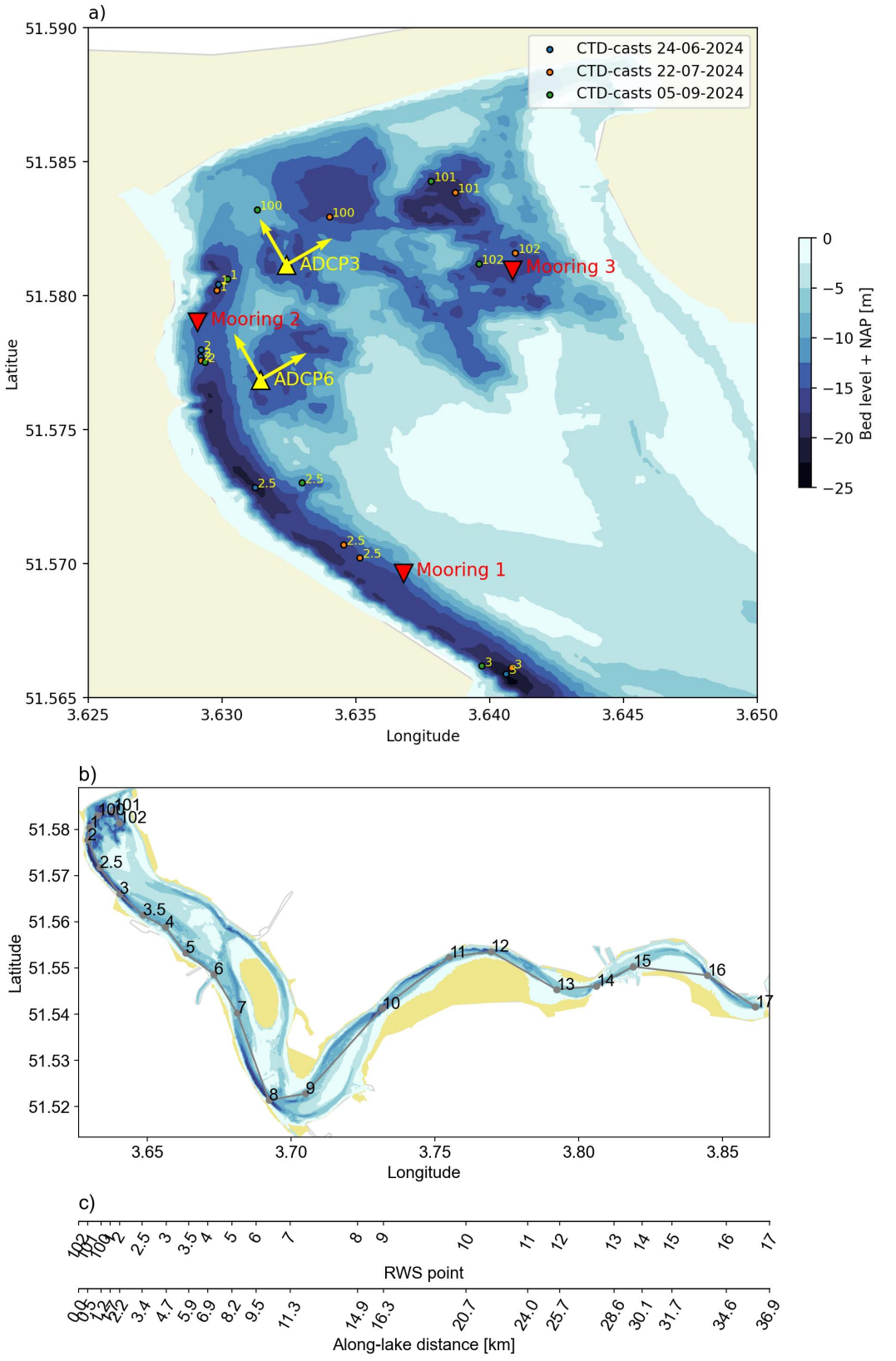


**Figure 3.1:** a) Measurement locations over the summer of 2024, showing the locations of two ADCPs, three moorings, and CTD casts spread out over three campaigns. Casts are labelled with their corresponding RWS TSO label. The cross-lake and along-lake coordinate system is shown with yellow quivers. Furthermore, we indicate b) RWS TSO location and c) corresponding along-lake distances used for interpolating the castaway profiles.

## 3.1. Direct stratification measurements

We directly measured the stratification in Lake Veere through two types of measurements: continuous temperature measurements with moorings and point measurements with a CastAway-CTD. The latter is, in practice, a higher-resolution version of the usual TSO measurements but does not measure oxygen levels. We first discuss the mooring and cast measurements, and then how we used them to characterize stratification in Lake Veere and how a thermocline height time series was inferred.

### 3.1.1. Temperature mooring measurements

We equipped three moorings with temperature sensors to measure temperatures over the water column. These operate at a high temporal and spatial resolution for extended periods of time. Furthermore, these thermistor chains are equipped with several pressure sensors to infer the depth at which the temperature sensors are recording. We employed temperature, CTD, and pressure loggers, which we divided over three moorings, as shown in Figure 3.1a. We placed the moorings such that the locations coincide with the hypothesized locations of maximum excitation of internal seiching (H.M. Clercx, personal communication, June 17, 2024). The moorings measure temperature, of which fluctuations are expected to have a maximum amplitude at the antinodes.

The temperature sensors (RBR*solo*$^3$ T) measure at a sampling frequency of $1$ Hz and are mounted on the cable at a depth resolution of $0.4$ m. The pressure sensors (RBR*solo*$^3$ D) are, due to limited availability, sparsely divided over the thermistor chains. We added either one or two pressure sensors depending on the cable length. This configuration allows for linear interpolation between pressure sensors to determine the vertical position of each temperature sensor. Finally, a CTD sensor (RBR*concerto*$^3$) is installed at the downward end of each mooring. The configurations of the three moorings are shown in Figure 3.2. Temperature and pressure are measured with an accuracy of $0.002\,^\circ$C and $0.05$ % FS, respectively. FS refers to the full-scale range of the device, $1000$ dbar, approximately amounting to $1000$ m. The CTD sensors measure temperature at the same accuracy but measure the depth with an FS of $750$ m. Conductivity is measured at an accuracy of $0.003$ mS/cm.

The moorings were prepared in the Waterlab and acquired in the context of StratiFEst (Kranenburg, 2023). They were installed on Monday, June 3 to measure over the summer of 2024 and recovered on September 6, 2024. Mooring 1 was caught on a piece of measurement equipment during the regularly scheduled TSO transects, causing it to snap, fatally damaging temperature sensors 10 and 11 on September 5. Sensor 10 was damaged to the point where the data was lost, while sensor 11 was still usable.

### 3.1.2. High-resolution point measurements with a CastAway-CTD

We used the SonTek CastAway-CTD (see Figure 3.3) to measure CTD profiles along a longitudinal profile in Lake Veere. A CastAway-CTD is a measurement device which is cast from a line into the water, measuring conductivity, temperature, and pressure as it is lowered to the bed. Conductivity is converted into salinity and pressure is converted into depth. The CastAway measures at $5$ Hz and is designed for a free fall speed of $1$ m/s, combining for a maximum measurement spacing of $0.2$ m. Salinity, temperature, and depth are measured with accuracies of $0.1$ PSU, $0.05\,^\circ$C, and approximately $0.25$ m, respectively.

We collected CastAway-CTD measurements while tagging along with the regularly scheduled TSO measurements by RWS (see Table 3.1). On June 24, July 22, and September 5, 2024, we collected measurements along the same transect and at the same points as the TSO survey (see Figure 3.1b). To improve resolution in a section where fish mortality was observed, we added two additional casting points: one between points 2 and 3 (“2.5”) and another between points 3 and 4 (“3.5”), increasing the total number of measurement points to 19.

The TSO vessel began its survey from the dock near Veere, conducted measurements in the northwest corner, and proceeded eastward along the lake. The full campaign lasted between $4$ and $6$ hours, depending on external conditions.

We secured the CastAway on a line with depth markings at a $1$ m resolution. To minimize drift, we attached an extra weight (see Figure 3.3), increasing the free-fall speed and requiring some resistance while lowering. Additionally, the weight facilitates detecting the bottom when lowering the CastAway.

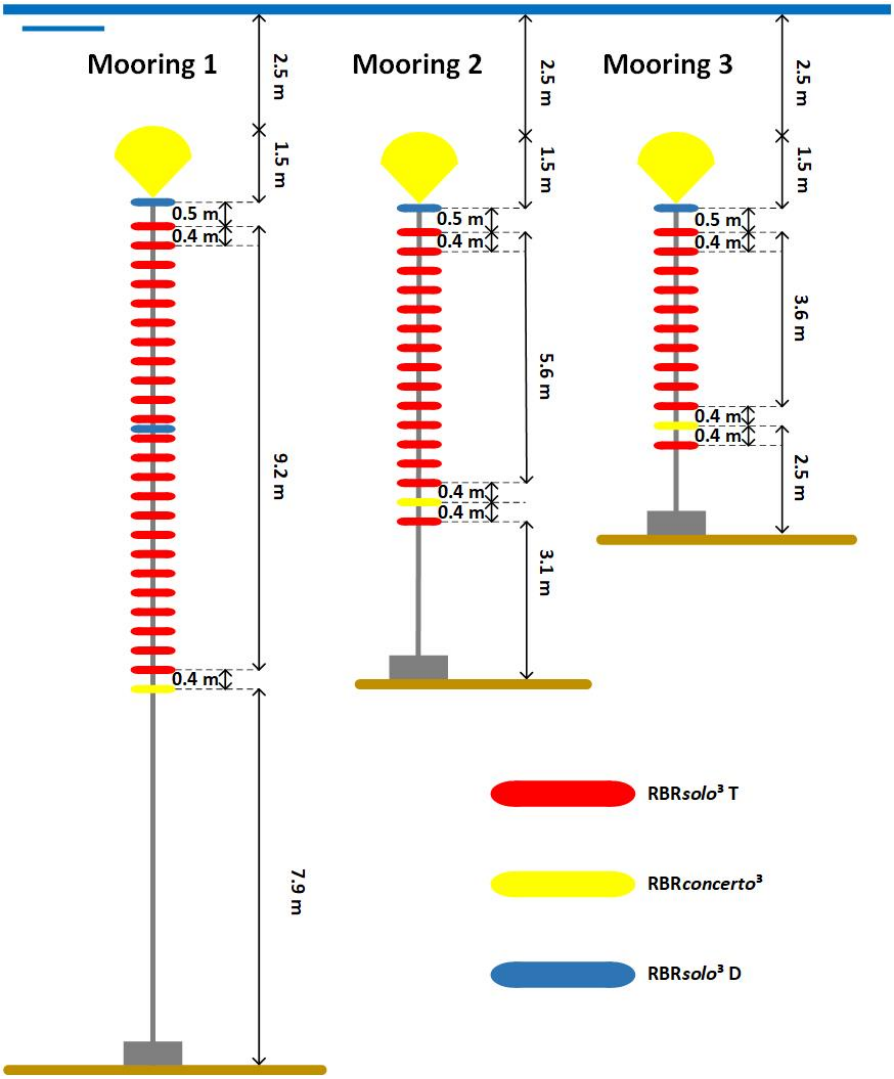


**Figure 3.2:** Schematic of the temperature moorings.

**Figure 3.3:** Sontek CastAway-CTD secured on a cable including extra weight.

We used the depth markings to better control the fall speed. Before each measurement, the CastAway is connected to GPS satellites. After a $10\,\mathrm{s}$ acclimatization period just below the surface, we manually lowered it through the water column until reaching the bottom, before reeling it in. Throughout the process, the CastAway remains secured to the railing to mitigate the risk of loss. Once retrieved, the measurement is finalized, and its location is saved. We omitted several measurements due to faulty data or GPS failure. Figure 3.1a shows the available casts in the northwest of Lake Veere.

Minimal processing is required for the CastAway profiles. We converted the cast data to NetCDF using the CastAway software to facilitate Python analysis. Profiles are analyzed according to their RWS TSO labels. We use the CTD casts in two ways: to characterize the spatial pattern of stratification in Lake Veere and to facilitate the attribution of acoustic backscatter to specific scattering mechanisms (see Section 3.2).

### 3.1.3. Characterizing stratification and inferring thermocline height

We characterize the stratification in Lake Veere using the moorings and the CTD casts. Then, we infer the thermocline heights at three locations from the moorings.

Firstly, we characterize stratification spatially using the CTD casts on the three measurement dates (i.e., June 24, July 22, and September 5). We averaged the measured depths at each labelled point to get the approximate depths at each point. We then interpolated along these depths to create transects along the fairway of Lake Veere, similar to the TSO transects by RWS (see Figure 1.2) but with a higher vertical resolution. The cast locations and interpolation distances are shown in Figure 3.1b and c.

Using CTD cast profiles, we analyze the distribution of temperature and salinity gradients throughout the lake. Finally, we assess the contributions of temperature and salinity to density to determine the dominant stratification type along the transect. We use surface temperature and salinity to compute a reference density at the surface. Keeping either temperature or salinity constant while moving downward, we compute the difference with the reference density to obtain profiles for $\Delta\rho_T$ and $\Delta\rho_S$, indicating the respective contributions of temperature and salinity to density over the vertical w.r.t. the surface.

We use the mooring data to give a general description of the temporal evolution of stratification. We roughly estimate the maximum $TSI$ by computing vertical temperature gradients and discuss the warming of the lake over the summer. Additionally, we identify mixing events through homogenization of the temperature profile. This is aided by the Richardson number, which is used to identify periods of stable stratification and to identify periods of mixing and unstable stratification.

H.M. Clercx performed most of the temperature processing (personal communication, December 4, 2024), so for this research, we primarily processed the mooring data to align it with the acoustic backscatter and velocity grids, as detailed in Section 3.2. To match the temporal resolution of the echosounder, we averaged the data from $1\,\mathrm{Hz}$ to once per $6\,\mathrm{min}$. We then interpolated it onto the vertical grid of the echosounder, using measured temperatures at the mooring's ends to pad areas outside of the mooring's range, allowing the computation of fully sound speed profiles for accurate echo-grid estimation.

Similarly, we interpolated the temperature data onto the velocity grid to compute the gradient Richardson number, but without padding, since Richardson relies on gradients so same-padding would not add any meaningful information. The Richardson number is determined using Equation (2.2), a central differences scheme for density gradients, velocity data from ADCPs, and temperature data from mooring 2, which is located the closest to ADCPs. A theoretical stability limit is $Ri > \frac{1}{4}$, but a more practical analysis may use a higher stability limit, in which case the limit becomes more of a limit for complete mixing through the water column instead of a very localized stability limit. In this case, a limit of $Ri > 10$ is used for qualitative purposes.

H.M. Clercx took the following steps to derive a time series for thermocline height from the temperature moorings (personal communication, December 4, 2024). First, they determined the sensor heights by linearly interpolating between the top and bottom pressure sensors, compensating for atmospheric pressure (Rijkswaterstaat, 2024). They then increased the spatial resolution to $10\,\mathrm{cm}$ using Akima interpolation. Next, they calculated the temperature gradient, applying same-padding at the boundaries. To

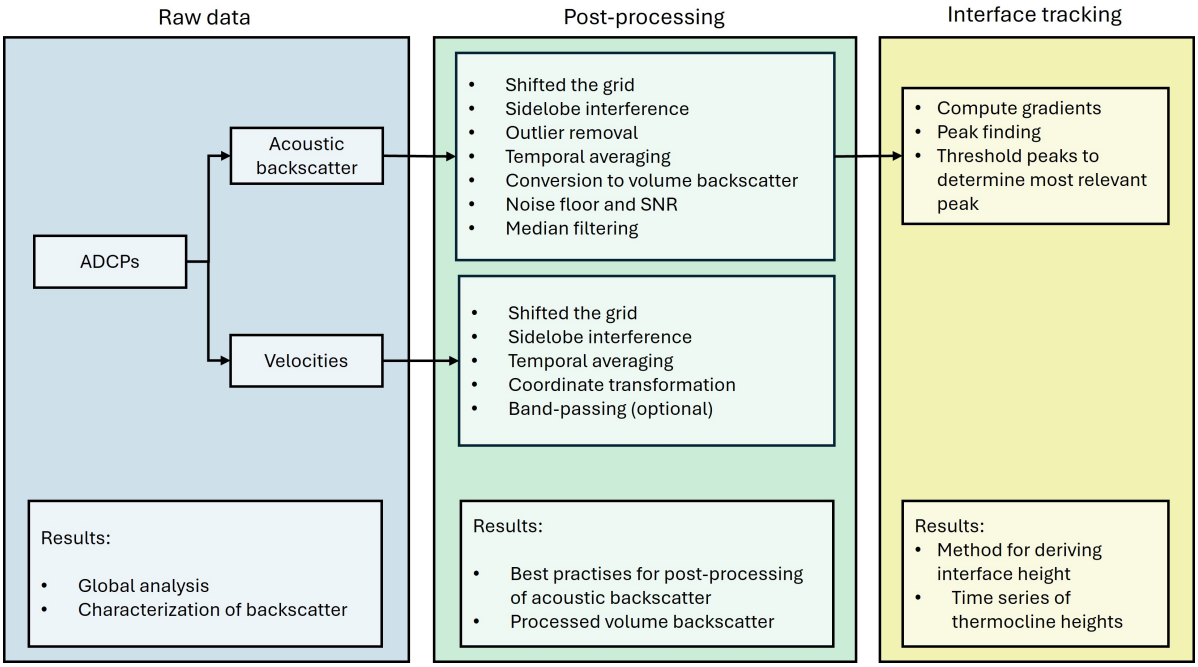


**Figure 3.4:** Flowchart of the methodology used for processing and analyzing the ADCP data. We mainly highlight the acoustic backscatter and indicate the results we obtain from each of these steps.

obtain a continuous time series of thermocline height, they tracked the maximum temperature gradient without a $TSI$-threshold (as a threshold would introduce discontinuities). Finally, they smoothed the series using a moving mean with a window size of approximately $3.5$ hours.

## 3.2. Acoustic stratification measurements

In this section, we outline the steps taken to obtain an acoustically measured time series of thermocline heights. This is visualized in Figure 3.4. Firstly, we discuss the used ADCP and the measurement campaign. Then we highlight the key considerations of the post-processing. Finally, we discuss the inference of dominant scattering mechanisms and thermocline heights from the acoustic data.

### 3.2.1. Measurement device and campaign

A Nortek Signature1000 is a five-beam ADCP with one vertically oriented beam (Bassett and Zeiden, 2023). The vertical beam is operated as an echosounder, collecting acoustic backscatter intensities (e.g., Velasco et al., 2018), so it is not used to measure velocities. The ADCP transmits acoustic pulses with a frequency of $1000$ kHz which are reflected by suspended particles in the water column, (e.g., biota, sediment, bubbles). Subsequently, the Doppler shift is measured and translated to velocities over the water column. It divides the water column into cells and determines three-dimensional flow velocity at sampling frequency $f_s$.

Besides the Doppler shift, the Signature1000s use echosounding to measure acoustic backscatter. The echosounders are operated in narrowband mode at multiple frequencies. Broadband mode allows for a $25$ %-frequency range of $875$-$1125$ kHz, while multi-frequency narrowband echosounding allows for larger (discrete) increments. The Signature1000 allows semi-simultaneous sampling at $1000$, $500$, and $250$ kHz. In this case, semi-simultaneous means that pulses are not transmitted simultaneously, but in series with a possible transmit pulse length of $0.064$ to $0.500$ ms. We tested the relatively new multi-frequency mode, which was made available by Nortek, in a controlled environment (see Figure 3.5). Using multiple discrete frequencies should show the theoretical frequency dependence of backscatter with particles of different sizes expected to most efficiently reflect echos of different frequencies (see Section 2.3.1).

We employed two bottom-mounted Signature1000 ADCPs between the temperature moorings between


**Figure 3.5:** Testing of the bottom-mounted Signature1000 ADCP in a flume. Test measurements were conducted in multi-frequency mode at $1000$, $500$, and $250$ kHz.

**Table 3.2:** Relevant settings of the ADCPs.

| Measurable | Quantity | Value | Unit |
|---|---|---|---|
| **General** | Samples per burst | $480$ | [-] |
| | Burst duration | $6$ | [min] |
| | Burst: sampling | $2$ | [min] |
| | Burst: idling | $4$ | [min] |
| **Velocity** | Number of cells | $40$ | [-] |
| | Cell size | $0.5$ | [m] |
| | Blanking distance | $0.1$ | [m] |
| | Sampling frequency | $4$ | [Hz] |
| | Pulse frequency | $1000$ | [kHz] |
| **Backscatter** | Range | $20.02$ | [m] |
| | Bin size | $0.048$ | [m] |
| | Blanking distance | $0.1$ | [m] |
| | Transmit pulse length | $0.25$ | [ms] |
| | Pulse frequency 1 | $1000$ | [kHz] |
| | Pulse frequency 2 | $500$ | [kHz] |
| | Pulse frequency 3 | $250$ | [kHz] |

June 3 and September 6, 2024 (see Figure 3.1a). These are referred to by their index given by TU Delft, i.e., ADCP3 and ADCP6. We expected the largest internal flow velocities to occur between the moorings since the largest flow velocities of unimodal internal seiching occur at the node (between the anti-nodes; H.M. Clercx, personal communication, June 17, 2024). A miscommunication saw the placement of the ADCPs slightly off, such that the ADCP3 was not placed exactly in the middle (in cross-lake direction) and ADCP6 was not located in the former tidal channel, but in another pit closer to mooring 2.

The ADCPs operate in six-minute burst intervals, collecting data for two minutes followed by four minutes of idling. This data is stored in memory without averaging. The other relevant ADCP settings are listed in Table 3.2.

### 3.2.2. Acoustic data processing

All data were converted to NetCDF using MIDAS to facilitate parallel operations and indexing along multiple coordinates. Subsequent operations are performed in Python. In this section, we discuss the post-processing steps of the acoustic data. These steps are outlined in Figure 3.4. For the acoustic backscatter, we average, remove range dependence, remove noise, and apply filtering to smooth the data. We average the velocities and project them to a more relevant coordinate system. We provide

brief discussions here but often refer to Appendix C for more detailed considerations.

### Pre-processing of acoustic backscatter

Firstly, we redefine the spatial grid of the acoustic backscatter to the centre (rather than the default outputted end) of each cell. This grid is based on a nominal sound velocity of $1500\,\mathrm{m/s}$, but in reality varies along with variations in the speed of sound, which in turn varies with temperature, salinity, and pressure (in order of importance). We assume that this is negligible, and refer to Appendix C.1 for a detailed discussion.

Sidelobe interference affects both acoustic backscatter and velocity data, occurring when ADCP sidelobes reach a boundary (e.g., the surface) before the main beam (Nortek Support, 2022, 2024b). This contaminates signals, rendering them unusable in the affected region. While precise methods exist to determine its range, vertical velocities provide a useful estimate, as they should be zero near the surface but may show offsets due to interference. The penetration depth varies with surface scattering, influenced by waves and wind. For simplicity, a constant depth is often set at $90\,\%$ of the pre-boundary range (M. Daugharty, personal communication, December 10, 2024). Similarly, we limit the analyzed range to $90\,\%$ of $13.25$ and $17.49\,\mathrm{m}$ for ADCP3 and ADCP6, respectively, to account for sidelobe interference.

Before averaging, we remove outliers from the acoustic backscatter to reduce the potential offset of averaging introduced by the outliers. We do this in the $\log$-domain, so means and standard deviations become geometric means and geometric standard deviations, respectively. We use the geometric mean (and standard deviation) for its decreased sensitivity to the large variation of acoustic backscatter. We filter outliers using the daily geometric mean and a threshold of one (daily) geometric standard deviation as a threshold (see Appendix C.2). We then burst-average the acoustic backscatter using the geometric mean, so we get $1$ measurements per $6\,\mathrm{min}$.

The Signature1000s record backscatter as $P_r$, from which we need to remove range dependence. The acoustic pings emitted by the ADCP are attenuated as they propagate through the water column, so backscatter inherently reduces with distance from the transmitter and is therefore not readily used for analysis. We correct the signal for the distance from the echosounder using Equation (2.20) to arrive at volume backscatter strength $S_v$. For this, we require $\alpha$, $\Psi$, and $PL$.

We computed absorption using the formulas by Francois and Garrison (1982a,b) shown in Appendix A. The target reflectivity $-10\log_{10}\frac{c\tau_{\mathsf{pulse}}}{2}$ may be taken as the spatially varying cell size, but is here approximated using a constant cell size of $\Delta r = 0.048\,\mathrm{m}$. Finally, we compute the equivalent beam angle $\Psi$ through (Nortek Support, 2025)

$$\Psi = 10\log_{10}\frac{5.78}{(ka)^2}, \tag{3.1}$$

where $a = 15\,\mathrm{mm}$ is the transducer radius specific for the instrument and $k = \frac{2\pi}{L} = \frac{2\pi f}{c_s}$ is the wave number, which varies with the speed of sound. We set the reference power $PL$ is set to $0$.

We disregard the constant $G_{\mathsf{int}}$ since the echosounder is not calibrated. Technically, we are therefore working with relative volume backscatter rather than absolute volume backscatter. However, we will continue referring to it as volume backscatter for simplicity. Calibration is not expected to affect the localization of the thermocline—only its parameterization—because it appears as a linear term in the $\log$-domain, in which we are also working. Since thermocline localization relies on gradients in volume backscattering, which remain unaffected by the constant $G_{\mathsf{int}}$, disregarding this constant does not impact our results.

We proceed with removing noise from the volume backscatter, which we quantify through the noise floor. The noise floor provides a measure of the range-dependent noise received from the environment. At a large range, the echosounder no longer receives backscatter and the signal asymptotically flattens to a constant value, which is indicative of the noise floor. This range depends heavily on the signal attenuation, which in turn depends on the frequency and absorption-related quantities. In practice, $30$ meters is generally sufficient range for at least $1000\,\mathrm{kHz}$ to reach the noise floor.

**Table 3.3:** Orientations of the ADCPs, averaged over the measurement period. Orientations remained practically constant.

| | Heading | Pitch | Roll |
|---|---|---|---|
| ADCP3 | $310°$ | $16.1°$ | $11.2°$ |
| ADCP6 | $108°$ | $4.65°$ | $-17.6°$ |

The noise floor is determined through either passive measurement ("listening mode") or by estimating the range at which the noise floor is reached. Accurate passive measurements are challenging for uplooking ADCPs, but could theoretically be collected beforehand or afterwards, suspending the ADCP in listening mode from a vessel. We opted not to do this and to follow the noise-correction procedure by Bassett and Zeiden (2023), who adapted it from Robertis and Higginbottom (2007). It consists of the following steps: 1) identifying the noise floor, 2) determining (and subtracting) the noise threshold, and 3) removing data with a low signal-to-noise ratio ($SNR$). After this process, we have removed the range-dependent system noise from the volume backscatter and filtered data below the $SNR$-threshold. We refer to Appendix C.3 for the full procedure. We used a noise threshold of $23$ dB and an $SNR$-threshold of $3$ dB for the $1000$ kHz signal. The $500$ and $250$ kHz measurements were excluded at this point due to consistently low $SNR$s (even with conservative noise estimates; Jaarsma, 2023), which we further discuss in Section 4.2.1, but were used qualitatively for interpreting the scattering mechanisms.

Finally, we test the use of several filters that aid the localization of the thermocline. This is essentially an edge detection problem (between two water parts of the water column), which is often seen in image processing. We tested several filters (see Appendix C.4) but settled on a median filter of size $5$ in both time and space, meaning that we determine the median over $0.048 \times 5 = 0.24$ m and $6 \times 5 = 30$ min. The latter already indicates the limitations regarding frequency analysis, which we revisit in Section 3.3.

#### Pre-processing of velocities

Similar to the backscatter, we redefine grid cell coordinates to the center of each $0.5$ meter cell and remove data beyond $90$ % of the pre-boundary range to account for sidelobe interference. We burst-average the velocities, too, but in the linear domain.

The velocities are projected from BEAM coordinates to a more tangible coordinate system. This transformation is discussed in Appendix C.5. In summary, the coordinates are projected from BEAM coordinates to a local $xyz$-system and subsequently to the ENU (East-North-up) system. Finally, we convert this to a more locally relevant coordinate system of along-lake and cross-lake velocities by rotating $30°$ anti-clockwise, shown in Figure 3.1.

A large tilt (pitch and/or roll) increases the error in the velocity profile. Horizontal velocities are a function of the cosine of pitch and roll and are, as such, not significantly altered by small tilt angles. Any tilt over $10°$ should be compensated for, while $30°$ renders one of the beams unusable (Nortek Support, 2022). The measured orientations of the ADCPs remained constant over the measurement period and are shown in Table 3.3. These indicate a significant tilt for both ADCPs, requiring not only a transformation from beam to a local $xyz$-coordinate system, but a subsequent transformation to ENU-coordinates since $z$ is not pointing upwards. A large tilt also results in the cells of opposing beams being located at different depths. Compensation for this is called bin mapping (Nortek Support, 2022), but we do not include it in this research.

Finally, in some cases, we band-pass the velocities to isolate specific frequency components. We do this after the frequency analysis and discuss this in Section 3.3.4.

### 3.2.3. Characterizing acoustic backscatter

Analyzing acoustic data is often complicated by the contribution of many scatterers, which are difficult to measure comprehensively. Inferring the thermocline from acoustic data may therefore be hampered by the dominance of a different backscatter process rather than impedance gradients by stratification. This warrants an analysis beforehand, characterizing backscatter using the available data, either indicating that the thermocline is directly responsible for backscatter, or whether other processes dominate. If other processes dominate the backscatter, we should research whether it can be used as a proxy for thermocline height. The scattering mechanisms are identified using the CTD casts, the frequency

dependence of the raw backscatter $P_r$, and through observing trends, events, and anomalies in the backscatter.

We use the CTD casts to compute theoretical reflection coefficients using Equation (2.16) and overlay them with the acoustic data. From this, we find whether the measured acoustic backscatter can be attributed to gradients in stratification. The theoretical reflection coefficients are derived from the casts using Equation (2.16). While not exactly co-located, we compare backscatter by ADCP3 with reflection coefficients from cast locations 1 ($208\,$m) and 100 ($229\,$m) and backscatter by ADCP6 with reflection coefficients from cast location 2 ($174\,$m) for the casts taken on July 22, 2024 (see Figure 3.1a). The hourly geometric means (using one hour around the cast time) of the volume backscatter are overlayed with the theoretical reflection coefficients to determine whether stratification is the dominant scattering mechanism.

Besides, we include a manual data review. Besides the presence of layering, we identify specific periods of interest, events, and qualitative developments. We analyze the acoustic backscatter $P_r$ of all channels and the volume backscatter $S_v$ of the $1000\,$kHz channel. We visually characterize several trends, such as the presence, creation, or destruction of layers in the water column. We analyze their general evolution and observe oscillations. We categorize these observations as general trends and event-based observations.

### 3.2.4. Inferring the thermocline height from acoustic data

We identified periods of stratification in the previous section, of which we analyze the volume backscatter in this section. Mooring 2, located closest to the ADCPs (see Figure 3.1a), provides the best continuous comparison of thermocline depth derived from acoustic data. However, this comparison requires caution, as opposing seiching modes may cause out-of-phase behaviour between the thermoclines measured by these devices. Thus, the focus should remain on the general evolution of thermocline height rather than exact overlap.

We adopt a similar approach to Shibley et al. (2020) to infer the thermocline height from volume backscatter. In practice, the layers in the upper water column were separated by sharp gradients in volume backscatter $S_v$ rather than peaks. The interface, which is a maximum vertical gradient, is found by tracking $\nabla S_{v;\text{max}}$. Thresholds for the prominence and peak height are defined in terms of the geometrical standard deviation of volume backscatter over the vertical at each time step (Shibley et al., 2020), with

$$\begin{aligned} th_{\text{prom}} &= f_{\text{prom}}\sigma_{\text{geom}} \\ th_{\text{height}} &= f_{\text{height}}\sigma_{\text{geom}}, \end{aligned} \tag{3.2}$$

where $th_i$ denotes the respective thresholds for prominence and height, $f$ their respective factors, and $\sigma_{\text{geom}}$ the geometrical standard deviation over the vertical (at a timestep). We use factors $f_{\text{prom}} = 4$ and $f_{\text{height}} = 1$. Furthermore, we use a maximum vertical distance between local peaks of $1\,$meter and a minimum peak width of $3\Delta z = 14.4\,$cm. Finally, we used boundaries between which the peaks are found to exclude the surface: $z_{\text{min}} \in [2.5, 6.5]\,$m and $z_{\text{max}} \in 0.9 \times [13.25, 17.49]\,$m respectively for ADCP3 and ADCP6. These thresholds were calibrated manually. Most instances of multiple layers were short-lived, so we used the global maxima instead of the local maxima, thereby assuming that the water column (in the analyzed interval) is separated into two layers and excluding secondary layers.

Besides the maximum gradient, another deep interface was observed by ADCP6 at longer time scales. This was tracked using: $f_{\text{prom}} = 1$, $f_{\text{height}} = 0.5$, minimum vertical distance between peaks of $1\,$m, and a minimum peak width of $4.8\,$cm. From the boundaries, it becomes clear that the two interfaces measured by ADCP6 do not overlap. This would not have been the case, because the interfaces are not tracked simultaneously.

## 3.3. Frequency analysis of thermocline motions

Correctly mapping the oscillations present in the interior of Lake Veere consists of four steps: 1) finding the theoretical frequencies of internal oscillations of the thermocline, 2) pre-processing the thermocline height time series, 3) linking the theoretical frequencies to the frequency components in the thermocline

height signals, and 4) validating the observed oscillations with velocity measurements. Firstly, we describe the methods to compute theoretical internal frequencies. Secondly, we process the interface times series discussed in the previous sections to remove outliers and make them suitable for frequency analysis. We then discuss the methods for continuous wavelet analysis. Finally, we research flow velocities in the presence of internal oscillations and assess whether these are consistent with the results from the continuous wavelet analysis.

### 3.3.1. Theoretical internal frequencies

The physical interpretation of the frequency analysis relates the observed peaks in energy frequency spectra to expected dynamics in Lake Veere. The characteristic frequencies of these dynamics were discussed in Section 2.2. Given the lake's low dynamic activity, wind-induced baroclinic motions likely dominate, but frequency analysis must confirm this. These dynamics include thermocline tilting and subsequent internal seiching, which, under Coriolis influence, may generate various wave types. Wind forcing may also produce high-frequency internal waves (Wüest and Lorke, 2003) and rotary currents at the inertial frequency. Each relevant frequency should be found to enable the correct interpretation of the continuous wavelet transform. The inertial frequency is known beforehand through Equation (2.13), using a latitude of $51.55\,^{\circ}$.

To resolve internal seiche modes under arbitrary stratification, we apply the method from Gill (1982) to solve Equation (2.11), initially coded in MATLAB by Klink (1999) and later translated into Python. Since no casts were taken in August, we estimate the internal phase speed using a two-layer model with approximate temperatures and layer heights from August 5 and 16. These dates provide a bandwidth of internal seiching periods at each mooring. The wave period largely depends on the effective basin length through Equation (2.9), but the complex basin geometry (see Chapter 1) complicates accurate estimates. To approximate the bandwidth, we estimate the basin lengths as $2.5\,$km along the main channel and $500\,$m across pits (see Figure 3.1). These constitute the upper and lower bounds of the effective basin length, so represent a conservative bandwidth. Combining these values with computed phase speeds, we derive a seiching period bandwidth through Equation (2.9).

To establish an upper bound for high-frequency internal waves, we compute the buoyancy frequency using Equation (2.15) and CTD density profiles. Burst averaging of acoustic backscatter, which reduces the measurement frequency to once every six minutes, limits the resolution of the shortest waves, with typical periods of around $2\,$minutes.

### 3.3.2. Pre-processing of interface time series

The time series obtained through the previous methods were pre-processed for frequency analysis. Firstly, we removed outliers using a daily rolling mean with a window size of $1$ day and a threshold of two standard deviations. During times of decreased stratification, e.g., due to erosion of the stratification by mixing, the standard deviation increases, so this does not capture all the outliers. A frequency analysis requires a temporally consistent time series with a constant step size. A problem arises when gaps exist in the time series. These may occur when no peaks (in temperature gradient or in backscatter gradient) satisfy the predetermined thresholds or after the removal of outliers. In this case, the missing data was filled through linear interpolation. Since this operation does not have a cyclic component, it should not interfere with the frequency analysis.

We then removed the trend of the data by subtracting the fitted, first-order polynomial and subsequently normalized the data using the newly (that is, after outlier-removal) computed daily means and standard deviations (Krieger and Freij, 2023; Torrence and Compo, 1998). The final remaining outliers are filtered using a low-pass fourth-order Butterworth filter with a cutoff frequency of $1\,\text{hours}^{-1}$ (e.g., Brenner et al., 2023). This final step indicates that frequencies higher than $1\,\text{hours}^{-1}$ are omitted from this analysis, meaning that high-frequency internal waves are not resolved above this frequency.

### 3.3.3. Continuous wavelet analysis

Continuous wavelet transform (CWT) is a mathematical tool to analyze the frequency components of non-stationary signals in the time-frequency domain. A wavelet is a zero-mean, rapidly decaying oscillation localized in both time and frequency (Farge, 1992; Thomson and Emery, 2024). The wavelet is scaled and shifted in time and subsequently fitted to a signal to test for the importance of a scale at a cer-

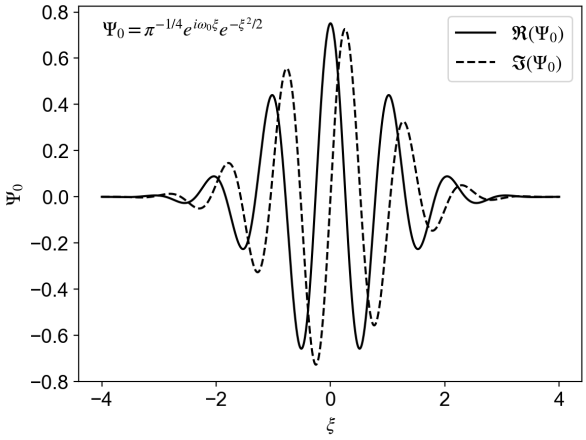


**Figure 3.6:** Morlet wavelet with (dimensionless) center frequency $\omega_0 = 6$. The real and imaginary parts are plotted separately.

tain time. These scales are predetermined and depend on the length of the signals and the frequencies of interest. Orthogonal and non-orthogonal wavelets are distinguished. Orthogonal wavelets, which are fitted to a signal, are uncorrelated and do not overlap, allowing for a discrete wavelet transform (Torrence and Compo, 1998). Non-orthogonal wavelets allow overlap and are used in both continuous and discrete wavelet transforms. Torrence and Compo (1998) provide a widely-used, practical guide to continuous wavelet analysis. We adapt this guide and its extension by Grinsted et al. (2004) to cross-wavelet analysis, discussing key considerations at each step.

1. Windowed Fourier transform to establish the necessity of wavelet analysis.
We created spectrograms using a windowed Fourier function with a window size of $2$ days.

2. Choosing a wavelet function and analysis scales.
A continuous wavelet transform requires a non-orthogonal wavelet (Farge, 1992; Torrence and Compo, 1998). Wavelets may be real or complex-valued. The latter returns both amplitude and phase, making it more suitable for our analysis. The Morlet is the most widely used wavelet in this category, especially in geophysical time series (Thomson and Emery, 2024). The Morlet wavelet is defined as

$$\Psi_0 = \pi^{-1/4} e^{i\omega_0 \xi} e^{-\xi^2/2}, \tag{3.3}$$

where $\Psi_0$ is the wavelet function, $\omega_0$ is the (dimensionless) center frequency, and $\xi$ is the dimensionless time. We used the Morlet wavelet with a centre frequency of $\omega_0 = 6$ for its good balance between time and frequency resolution (Grinsted et al., 2004). For reference, we show the Morlet wavelet in Figure 3.6.

The scales at which a wavelet is analyzed depend on the wavelet itself and the length of the signal. We chose the scales such that the smallest scale corresponded to $2\Delta t$ with $\Delta t$ the timestep ($6$ min). We set the largest scale to $N_{\text{signal}}/2$, where $N_{\text{signal}}$ is the number of samples in the signals. Scales in between usually follow a $\log_2$-distribution, with several steps in between powers of $2$. This resolution is represented by $\delta j$, which is generally constrained by the stability of the analysis on one end and the efficiency of the analysis on the other. We used $\delta j = 1/64$ for which neither stability nor efficiency presents issues. To summarize, the smallest resolved scale is approximately $12$ min and the largest half of the duration of the record that was computed in Section 3.2. Note that this period is too small to be resolved since we low-passed at periods of $1$ hour. The leakage of wavelet power of outliers (so at high frequencies) poses a significant problem if these frequencies are not band-passed, which would have rendered this part of the data unusable.

3. Finding the CWT of the time series.
The continuous wavelet transform (CWT) of a time series was computed by convolving the time series with a scaled and shifted wavelet function. We performed this convolution using PyCWT (Krieger and

Freij, 2023, citing Grinsted et al., 2004; Torrence and Compo, 1998), to find the wavelet coefficients (analogous to Fourier power) at each scale and time step.

4. Cone of influence and translation of scales to Fourier wavelengths.

The cone of influence is defined as the region unaffected by the edge-effects of the wavelet transform. In practice, the affected region is often excluded from analysis. The cone of influence is mathematically found using the $e$-folding time $\tau_{e\text{-folding}} = \sqrt{2}s$, in which $s$ denotes the scale (Torrence and Compo, 1998).

The scales of the Morlet wavelet are easily found algebraically (Meyers et al., 1993; Torrence and Compo, 1998). With $\omega_0 = 6$, the scales are almost identical to their Fourier counterpart with $T_{\text{Fourier}} \approx 1.03s$.

5. Wavelet coherence and phase.

Wavelet coherence provides a scale-normalized measure of the similarity between time series across different frequencies. It ranges from 0 to 1, where 1 indicates a perfect linear correlation at a given frequency. The complex coherence also encodes phase differences between the signals at specific frequencies. We computed complex wavelet coherence using PyCWT (Krieger and Freij, 2023), which is then separated into its real and imaginary components, representing coherence and phase, respectively.

After applying each step in the continuous wavelet analysis, we arrived at the wavelet power spectra of each signal and the complex coherence between different signals at all the considered frequencies. These were then related to the theoretical frequencies derived in the previous section with coherence and phase aiding the interpretation process. We used coherence and phase to distinguish between processes, mainly cross-lake and along-lake internal seiching. Additionally, we expect a daily component in the forcing of the thermocline, hypothetically related to heat input and therefore with zero-phase lag across the signals.

In the cross-lake direction, we expect internal seiching to occur between mooring 3 and the ADCPs or mooring 2, while, in the along-lake direction, we expect it between mooring 1 and the ADCPs or mooring 2 (see Figure 3.1). In terms of complex coherence, that means that if internal seiching occurred between ADCP3 and mooring 3 (cross-lake), the coherence magnitude at the cross-lake seiching frequency is high between both signals and the phase difference is $\pi$ rad, which indicates out-of-phase behaviour (refer back to Figure 2.3).

### 3.3.4. Flow velocities in the presence of internal oscillations

The direction of internal seiching, found from the coherence and phase between signals, was validated with cross-lake and along-lake velocities. It is expected that during periods of internal seiching, flow velocities above and below a thermocline (in a 2-layer stratification) are out of phase (i.e., reversed). We assessed this by identifying periods of expected internal seiching and isolating this frequency band in the velocity data using a band-pass filter.

Shear is often related to the depth of the thermocline (e.g., Bauer et al., 1981; Brenner et al., 2023; Simpson et al., 2021). We computed shear through Equation (2.25). During seiching, out-of-phase velocities above and below the thermocline give rise to vertical shear maxima at the interface height. Conversely, during tilting, two vertical rotation cells may develop in a steady state, constituting a shear minimum at the interface height. We researched this by identifying internal seiching through the wavelet spectra and complex coherence, validating this with velocity measurements, and researching shear during these events.

# 4
# Results

In this chapter, we discuss the results. First, we characterize the stratification in Lake Veere using CTD transects and temperature data from moorings. Next, we analyze acoustic backscatter to explore its relationship with stratification and derive a time series of thermocline height (RQ3). Finally, we examine the dominant internal oscillations in the lake using continuous wavelet analysis, investigate whether we can attribute these to specific wave types, and compare the findings with velocity measurements from ADCPs (RQ4).

## 4.1. Characterization of stratification using temperature and salinity measurements

The spatial character of stratification in Lake Veere is described using the high-resolution CTD measurements where available, supplemented by the TSO measurements and the temperature moorings. A first observation is the eastward (rightward in Figures 4.1 to 4.3) increase in water temperature, especially near the surface. In the second and third campaigns (Figures 4.2 and 4.3), the water temperature increased globally towards the east, while the first campaign (Figure 4.1)showed mainly an increase in surface temperature. The sun heats the surface water during the day, allowing the water to cool at night. This constitutes a daily cycle of increase and decrease of surface water temperature. This cycle coincides with the measurement campaigns, which launched from the west in the early morning and finished in the east in the afternoon. The surface temperature is therefore expected to increase towards the east as seen in Figure 4.1. This is also apparent in the second campaign, Figure 4.2, although it penetrates deeper. Similarly, the third campaign, Figure 4.3, shows an increase in temperature towards the east, but only in a global sense with a relatively well-mixed water column. Generally, the temperature of the lake increases between the three campaigns (over the course of the summer), but the amount of thermal stratification does not necessarily follow this increase. Each case shows a thermally stratified water column in the northwest, with the third campaign exhibiting the smallest temperature gradients.

The saltwater from the Eastern Scheldt stretches into the lake from the east along the bottom. Its distribution barely varies over the summer, but its magnitude does. The entire water column shows a general increase in salinity over the summer. This is likely due to the limited input of fresh water through precipitation and reduced discharge from surrounding polder pumping stations, leading to a net import of seawater from the Eastern Scheldt. The water column has quite a significant salt-stratification in the east, with a salinity difference of almost $3$ PSU between the surface and the bottom. In the west, this large stratification is not observed. Over the three campaigns, the difference between surface and bottom salinity is usually between $0.5$ and $1$ PSU in the northwest part of Lake Veere.

The density contours generally follow the salinity contours, which was expected from Figure 2.1a. For example, the density contours in Figure 4.2 follow the increased salinity near the bed all the way until around measurement point 3. Figure 4.2d and e show the separate contributions of salinity and temperature to density on July 22 (see Figures D.4 and D.5 for other dates). In each case, we computed the difference between the true density and the density if we took either the temperature or salinity as constant. In that way, we visualize the contribution of salinity and temperature to stratification (as seen from the surface). In the east, we observe that salinity is dominant, while temperature becomes more important towards the west, demonstrating the change of the dominant stratification type from east to west. This was most pronounced on July 22, when thermal stratification was strongest. An influence of salt is still found in the deep pit at measurement point 3. The importance of temperature is

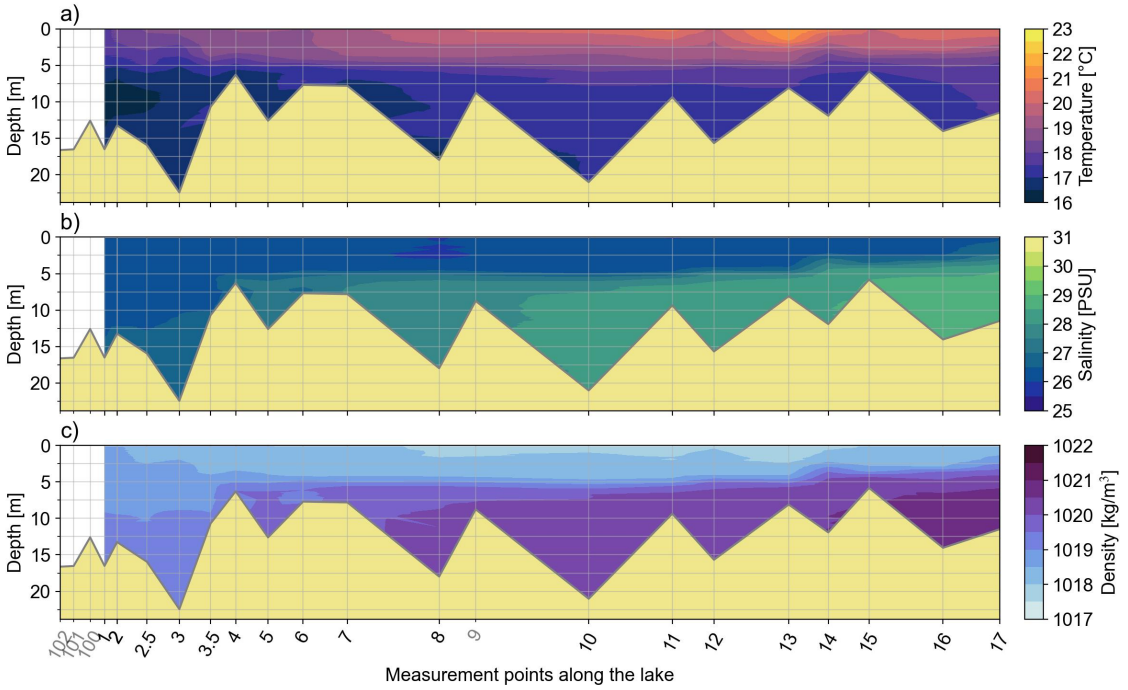


**Figure 4.1:** Transects of a) temperature, b) salinity, and c) density of Lake Veere on June 24, 2024. The horizontal axis shows the corresponding RWS measurement points along the lake. Grey labelling indicates that a measurement point was skipped on this day. Data is interpolated between available points. The average location and depth are used for the along-lake coordinate and height of the bed, respectively.

also visible in Figure 4.1; along the lake, the density contours follow the temperature near the surface and the salinity in the middle and along the bottom of the water column. In the west, they follow the temperature, again. Overall, contributions by temperature and salinity in the west are approximately equal during this campaign (see Figure D.4). During the third campaign in September, contributions in the west are also approximately equal but negligible, with the western part of the lake being relatively well-mixed (see Figure D.5).

We proceed with discussing the temporal evolution of stratification using the temperature measurements by the moorings, which are shown in Figure 4.4. A gradual increase in temperature is observed throughout the summer. This trend is generally the same for each mooring. At the start of June, the water temperature is around $15\,^{\circ}$C. Around June 10, this is completely homogenized over the moorings. This homogeneity persists until the end of June, with a maximum temperature difference between the top and bottom of the moorings of around $1\,^{\circ}$C. This homogeneity does not necessarily demonstrate the absence of stratification over the entire water column, just its absence from the ranges covered by the moorings. At the end of June, the highest sensors of moorings 1 and 3 measure an increase in temperature near the surface. This is the first clear sign of thermal stratification. This is also seen in CTD casts in Figure 4.1 (for a more quantitative representation, see Figure D.1), which show temperature differences of at least $2\,^{\circ}$C between the surface and the rest of the water column.

The first half of July does not exhibit strong signs of thermal stratification with a homogeneous temperature of $17\,^{\circ}$C over the moorings. During the second half of July, signs of stratification are apparent in all three moorings. Moorings 1 and 3 measure the strongest stratification. The depth of this stratification varies strongly but on average increases throughout August. Several events are distinguished where the warm upper layer dips down, for example on July 22 and 25. This is visible in all three moorings but is easily the strongest for moorings 1 and 3. From the second half of July, a seemingly daily oscillation becomes visible. Isothermals generally move downwards during the day and upward at night, but the exact behaviour varies per day. The maximum surface temperature $24\,^{\circ}$C is also recorded during this time. The middle of August shows the strongest thermal stratification and on average downward-moving isothermals. This persists until August 22, when the entire water column is homogenized again,

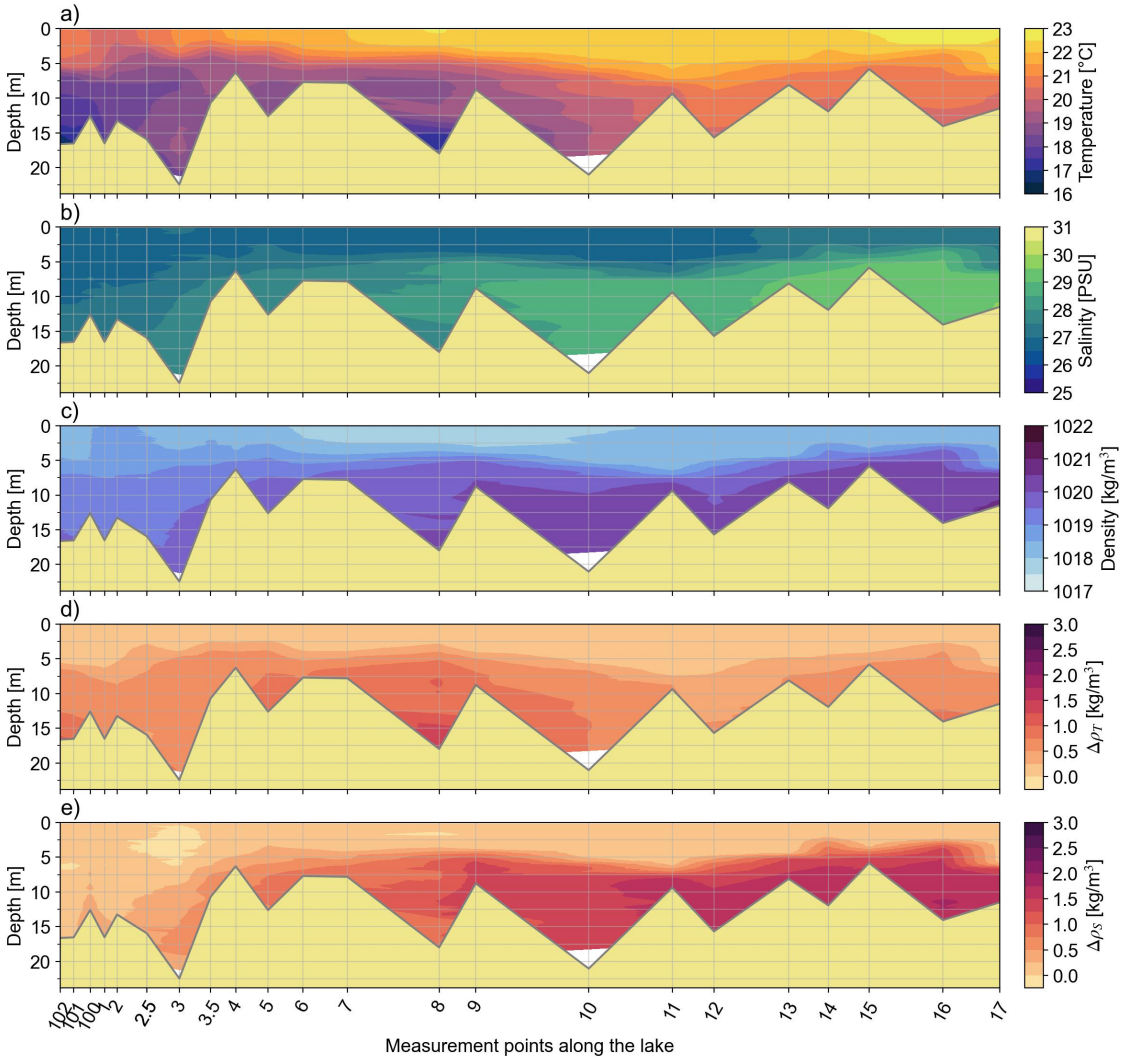


**Figure 4.2:** Transects of a) temperature, b) salinity, and c) density of Lake Veere on July 22, 2024. We also show the contributions of d) temperature and e) salinity to the density. These constitute the discrepancy between true density and approximate density if d) temperature or e) salinity were taken as constant (i.e., the value at the surface) over the water column. The horizontal axis shows the corresponding RWS measurement points along the lake. Grey labelling indicates that a measurement point was skipped on this day. Data is interpolated between available points. The average location and depth are used for the along-lake coordinate and height of the bed, respectively.

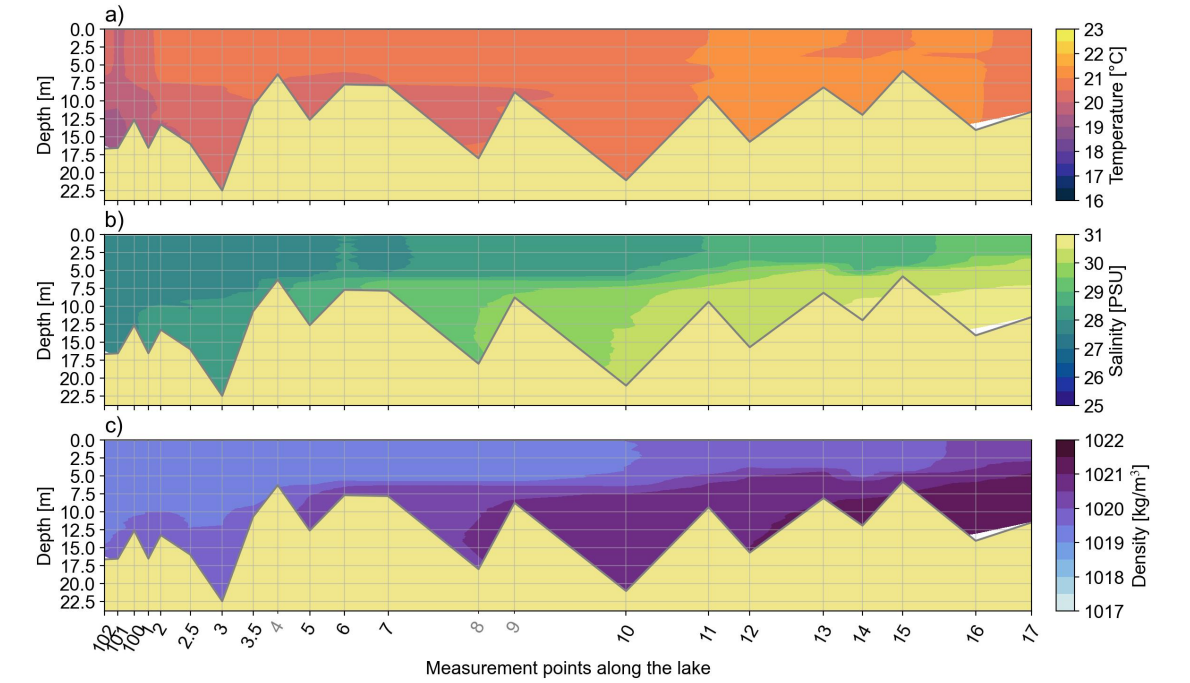


**Figure 4.3:** Transects of a) temperature, b) salinity, and c) density of Lake Veere on September 5, 2024. The horizontal axis shows the corresponding RWS measurement points along the lake. Grey labelling indicates that a measurement point was skipped on this day. Data is interpolated between available points. The average location and depth are used for the along-lake coordinate and height of the bed, respectively.

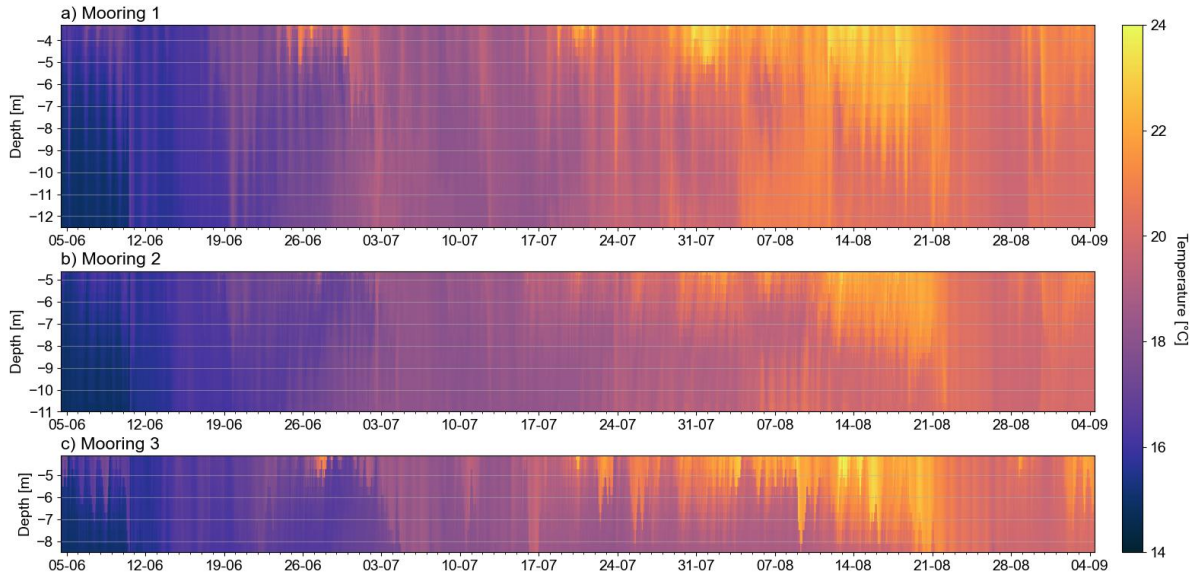


**Figure 4.4:** Temperatures recorded by the moorings over the summer of 2024. Data was processed and provided by H.M. Clercx (personal communication, October 9, 2024).

which is observed in each mooring. After the full homogenization, the start of September shows the development of some thermal stratification, strongest for mooring 3. We also assessed stratification stability using the Richardson number; however, the results were inconclusive due to the assumption of constant salinity. This led to artificially induced upward-positive density gradients in the lower water column, which are inherently unstable (see Figures E.1 and E.2). The thermally stratified upper water column was better represented, showing several periods of instability through June and July and towards the end of August.

The first week of August shows a notable event, where an oscillation of a warm water layer is visible from the bottom for mooring 2. Moving downward, a temperature increase of around $1\,^{\circ}$C is observed. A similar but smaller event is observed around July 28 for mooring 1. The interpretation of events and observations follows after investigating the extent to which thermal stratification can be inferred from the acoustic measurements.

In summary, the stratification in most of the water column (especially the range covered by the temperature moorings) of the northwestern part of Lake Veere is mainly governed by temperature gradients. Thermal stratification is strongest during the end of July and the start of August, after which the water column is homogenized on August 25. We use this as the final date of our acoustic analysis.

## 4.2. Detection of thermocline from acoustic backscatter

In this section, we infer the thermocline heights from the volume backscatter of the $1000$ kHz channel. We discuss the results in line with the flowchart in Figure 3.4. First, we globally analyze the acoustic backscatter at all frequencies for general observables and trends, in some cases supported by the volume backscatter, and compare the volume backscatter with CTD casts to infer backscatter mechanisms. Finally, we infer the thermocline heights using the maximum (gradient) of backscatter.

### 4.2.1. Characterization of backscatter

The raw data of ADCP3 is shown in Figure 4.5 (for ADCP6, see Figure F.1). The water surface is observed as a straight line of increased backscatter at approximately $13.25$ and $17.5$ meters. The thickness of the observed surface level varies and in some cases, the surface is observed as two smaller bands of increased backscatter. The surface is the only consistently measurable feature observed by both ADCPs at all frequencies. The $250$ kHz signal only captures surface reflections with minimal data besides this. Consequently, it is excluded from further analysis. Furthermore, the second measurement frequency, $500$ kHz, operates close to the noise floor. The removal of high-noise data depends on the selected noise threshold and $SNR$-threshold, but even conservative estimates render most of the $500$ kHz-signal unusable (also see Figure F.3). Care should thus be taken when inferring information from this measurement frequency.

These limitations suggest that the site contains few scatterers with diameters above $48$ (and $96$) µm (see Table 2.1), which are the minimum sizes of scatterers that reflect the echos at frequencies $250$ and $500$ kHz, respectively. The minimum scattering diameter of the $1000$ kHz signal is $24$ µm. Furthermore, the frequency dependence of the backscatter forms the basis of the argument that impedance gradients by stratification are not the dominant scattering mechanism. Considering the backscatter models in Equation (2.17) and Equation (2.19), backscatter from impedance gradients at stratification interfaces should increase with decreasing frequency. In practice, the backscatter decreased with frequency, so it is unlikely that backscatter is associated with impedance gradients by stratification. We further investigate this with the CTD profiles.

Theoretically, thermoclines reflect echos and should therefore constitute a (local) maximum in acoustic backscatter. We research this using the casts alongside the volume backscatter, which effectively removes range dependence, aiding this and further analysis. We show the squared reflection coefficients based on the CTD-casts in Figure 4.6. The echo data does not necessarily show volume backscatter peaks in the same region as the peak reflection coefficients. The right (c) profile shows instances where peaks are co-located, but the theoretically largest peak in the middle profile (b) is not found in the echo data. This peak is located $2$ meters below the backscatter peak measured by ADCP3. In the absence of calibration, we can not use Equation (2.22) to quantify the acoustical reflection coefficients, so we can not attribute these measured backscatter peaks to specific peaks in the predicted reflection

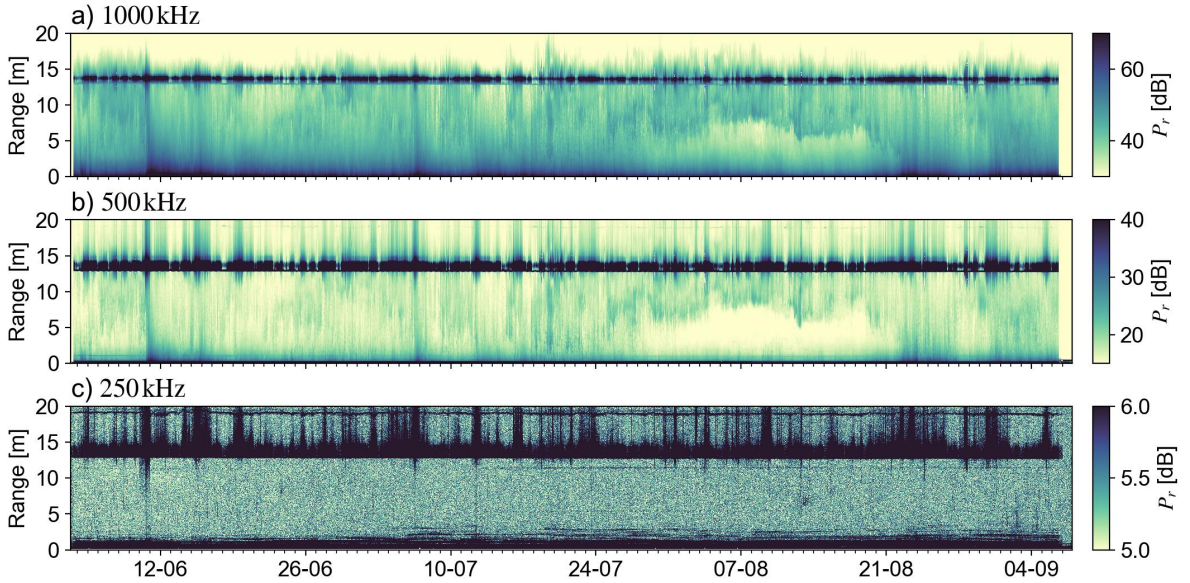


**Figure 4.5:** Raw acoustic backscatter recorded by ADCP3 at measurement frequencies a) $1000$, b) $500$, and c) $250$ kHz, This is pre-processed to remove outliers greater than one daily geometric standard deviation from the daily mean and subsequently averaged per burst.

coefficients, and conclude that impedance gradients at the thermocline are not the dominant source of backscatter. We should note the horizontal distances of order $100$ meters between the ADCPs and casts, so lateral differences in stratification could contribute to the discrepancies between the measured backscatter and predicted reflection coefficients.

Despite thermal stratification not being the direct source of backscatter, the data contains several interesting trends and events that are observed without requiring extensive analysis. We show the volume backscatter at $1000$ kHz for both ADCPs in Figure 4.7 (for $500$ kHz, see Figure F.2). Firstly, we observe that from the end of July up until the end of August a sharp gradient in volume backscatter separates the upper water column from the lower water column. Again, this is not a local maximum, suggesting that thermal stratification is not the responsible scatterer. Rather, it is a maximum gradient between an upper layer of increased backscatter and a lower layer of decreased backscatter. Not only is the backscatter of the lower layer low relative to the upper layer, but it is low compared to the entire backscatter record. We conclude that the upper layer contains an increased amount of scatterers, while these are absent from the lower layer. We hypothesize that the difference in occurrence is buoyancy-driven and the scatterers in the upper layer are separated from the lower layer due to their low density, prohibiting them from floating in a neutrally buoyant equilibrium in this layer. The stratification gradually develops throughout late July, with a clear boundary visible starting from around August 3. During this time, it increases in height from a depth of around $13.3 - 6 = 7.3$ m up to $17.5 - 12 = 5.5$ m (or $13.3 - 8 = 5.3$ m for ADCP3) depth around August 8, after which the depth increases by $2$ m. The gradual development of this layer is similar for both ADCP3 and ADCP6, which we discuss in detail in the next section.

Besides the layering in August, the data by ADCP6 shows an additional layer that persists from the middle of June up until August 7. At first glance, it seems the results of a high-intensity event on June 10, but upon closer inspection, it also briefly existed before this event, which may mark this event as a catalyst in the growth of this layer, but not necessarily its cause. It originally increases in height throughout June but dips out of view towards the start of July. Over the course of July, it increases in height from a depth of approximately $17.5$ to $17.5 - 4 = 13.5$ m in the middle of August and then disappears. Contrary to the previously discussed layering, this layer does constitute a local backscatter maximum. In general, the backscatter is slightly decreased just below this layer, then forms a maximum, and finally gradually decreases upwards, notably less abrupt than downward. The exact development of this layer and its height is discussed in the next section. Besides this layer, we observe other backscatter maxima (instead of maximum gradients) on August 8-9 and 23-25 (for the latter, see

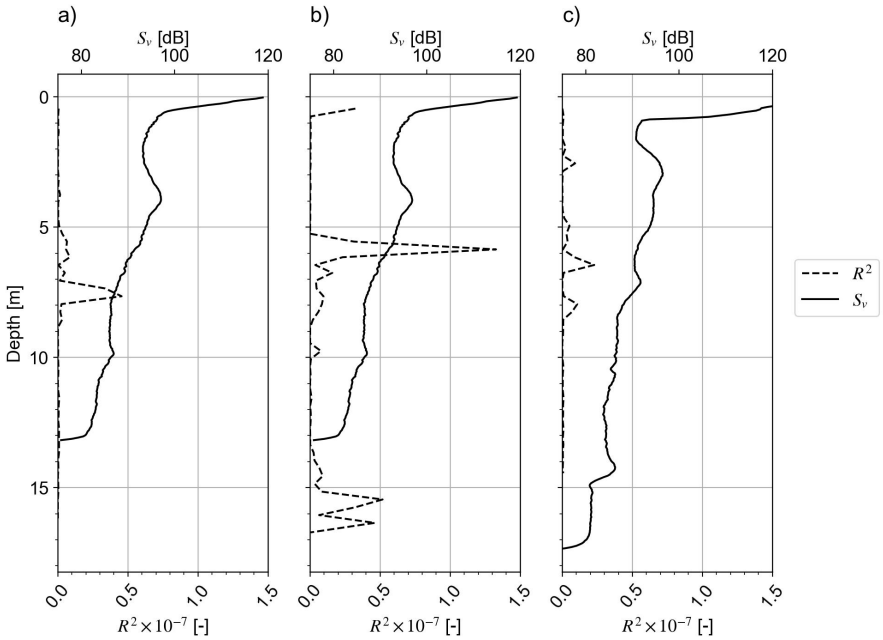


**Figure 4.6:** Hourly geometric means of the volume backscatter ($S_v$) alongside the theoretical reflection coefficients squared ($R^2$) for a) ADCP3 cast combined with location 1, b) ADCP3 combined with cast location 100, and c) ADCP6 cast combined with location 2. CTD Casts were taken on July 22, 2024.

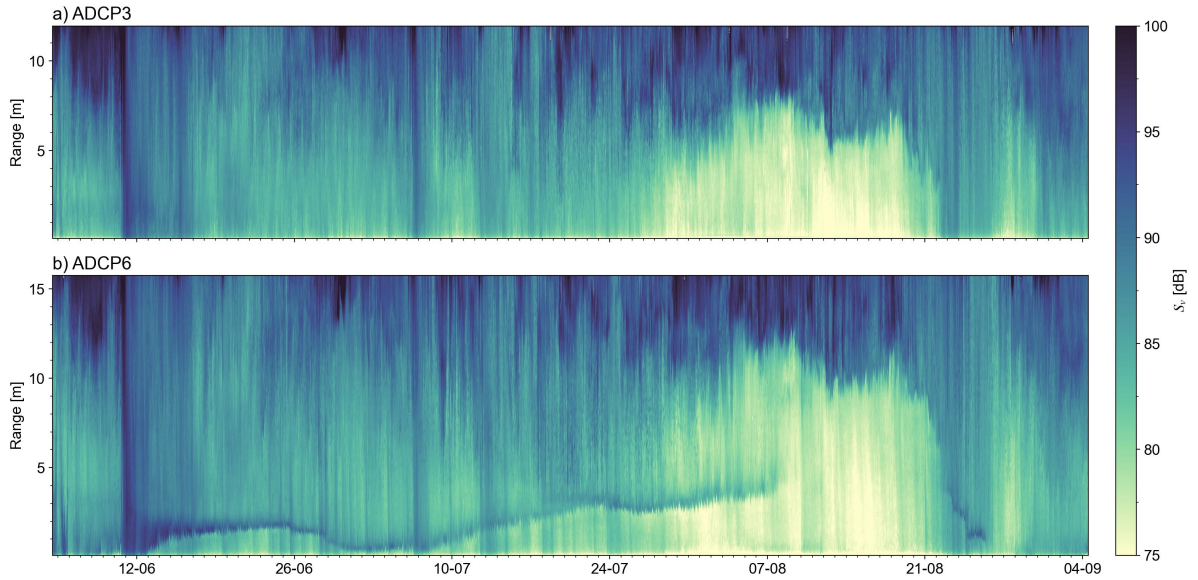


**Figure 4.7:** Volume backscatter of the first measurement frequency, $1000$ kHz, measured by a) ADCP3 and b) ADCP6. We observe clear layering in the backscatter of both ADCPs during August and a persisting lower layer recorded by ADCP6 during June and July.

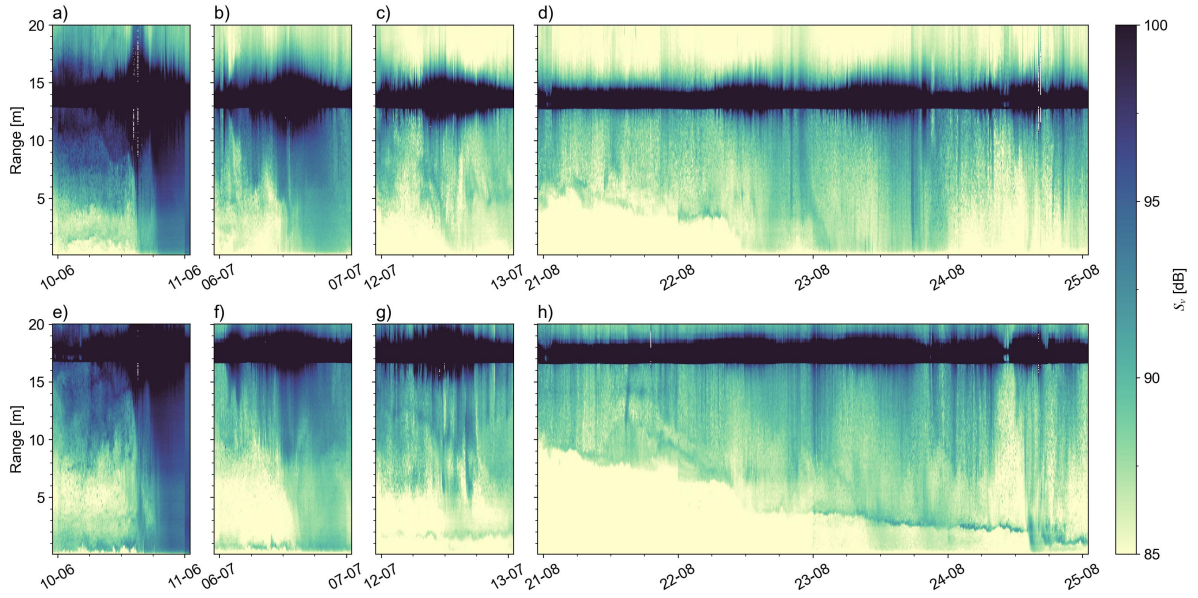


**Figure 4.8:** Volume backscatter measured by ADCP3 (a, b, c, and d) and ADCP6 (e, f, g, and h) at $1000$ kHz during mixing events. Events were identified by identifying periods where the volume backscatter was homogenized over the water column. White pixels were marked as outliers during pre-processing.

Figure 4.8h). This layer existed for several days after a mixing event, after which it disappeared again.

We found several occurrences of full mixing of the water column throughout the records. These are observed as a full homogenization of the volume backscatter across the water column, indicating that scatterers become well-mixed, instead of being mostly confined around the surface. Examples of mixing events, which we now define as events where the entire water column seems to homogenize (so not including partial mixing), include: June 10, July 6, July 12, and August 21-25. We show events in Figure 4.8, where we included the surface layer to emphasize the effect of increased shear on the surface on the measured backscatter. During periods of increased shear/mixing, the band of increased backscatter around the surface thickens and stratification is eroded if not fully erased. The storm on June 10 constitutes one of the bigger storms of 2024, which is also represented in the magnitude of the volume backscatter. We hypothesize this increase in backscatter to be induced by bubbles. This notion is further strengthened by the observation of a passing vessel (one of the TSO campaigns), causing a sudden increase in backscatter, which persists for a period of around $10$ min (see Figure F.4), likely caused by an injection of air bubbles into the water column. The mixing events on June 10, July 6, and July 13 all completely remove the weak layering that was present beforehand. During August, layering was much stronger and several events were recorded with increased backscatter at the surface that did not fully wipe out the layering. However, during the period between August 21 and 25, forcing at the surface was sufficient to fully overturn the stratification and mix the water column, which we also observed in the temperature measurements in Figure 4.4.

We show other anomalies besides mixing events in Figure 4.9. Firstly, we note how the band of increased backscatter is smaller now that the analysis does not specifically focus on mixing events. An interesting event occurred at the start of the measurements on June 4 and 5, before the initial layering was erased by the storm on June 10. A subsequent upward and downward oscillation is observed on these dates, respectively. This upward motion is recorded simultaneously by both ADCPs, while the downward motion is recorded a few hours earlier by ADCP3. Another upward motion is observed by ADCP6, but not by ADCP3. On June 30, the ADCPs recorded a band of increased backscatter around the surface that is not comparable to other mixing events in Figure 4.8. The backscatter at the surface compares well, but the band surrounding this has a relatively high magnitude while being contained close to the surface. Other events, where backscatter at the surface is of similar magnitude, reached further downward. This is mainly observed by ADCP6. On July 20, the bottom layer that was previously identified from ADCP6 gains an additional layer approximately $1$ meter above it, which persists for a few

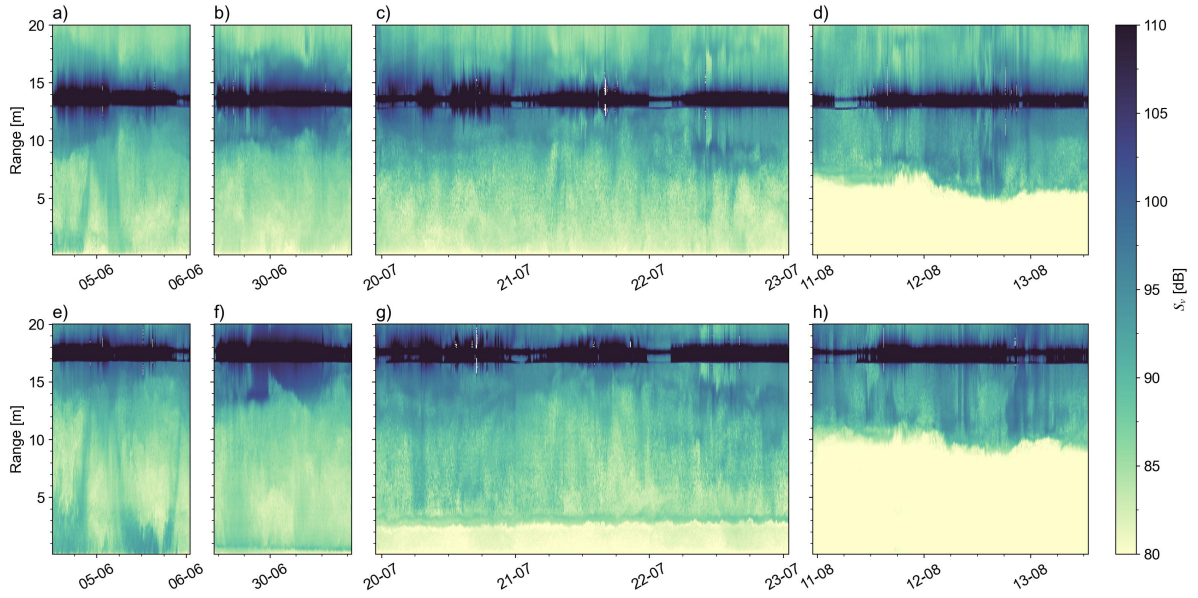


**Figure 4.9:** Volume backscatter measured by ADCP3 (a, b, c, and d) and ADCP6 (e, f, g, and h) at $1000$ kHz during specific events. Events were identified by observing anomalies compared to the rest of the data. White pixels were marked as outliers during pre-processing.

days before disappearing on July 23. Finally, on August 11-12, there is reason to believe a tilt of the thermocline has occurred. Following the start of a persistent band of increased backscatter on August 11 (which we assume to be wind), the interface moved downward, before its height increased again on August 13 when the wind subsided as observed by ADCP6. Additionally, the downward movement of the interface is accompanied by oscillations of increased frequency compared to the tilt. These are prevalent for ADCP6 but are barely observed by ADCP3.

### 4.2.2. Acoustically tracked interface heights

We continue with the inferred interface height from the volume backscatter. Six interfaces were tracked: the maximum temperature gradient measured by moorings 1–3 (H.M. Clercx, personal communication, December 4, 2024), the maximum backscatter gradients by ADCP3 and ADCP6 for the period of August 5 to August 21, and the maximum backscatter measured by ADCP6 for the period of June 12 to August 2. We first discuss the interfaces recorded in August and then continue with the lower interface that was recorded during June and July.

We show the echo-interfaces and the thermocline derived from mooring 2 in Figure 4.10 (for a full version, see Figure F.5). On average, the time series correspond well in height. Each time series starts at around the same height at a range of $8$ and $12$ meters for ADCP3 and ADCP6, respectively. This was already observed visually in the previous section. The average height stays constant for the first few days of the record, before moving downward on August 10, followed by an event of large deviation between time series on August 12 (also see Figure F.5 for the deviation between moorings); this event was previously identified as a potential tilt. Starting August 20, the interface erodes and is tracked less well.

The thermocline heights measured by the moorings generally show larger oscillations than the interfaces measured through the backscatter. Relatively large deviations occur, for example, on August 9 and 10, when the moorings show a deviation in the order of several meters downward, which is not observed by either ADCP. Similarly, the mooring time series show large deviations from August 13 to 15, which are not present in the echo data, except for one large deviation on August 15 recorded by ADCP3. On August 10, mooring 1 recorded a large downward movement of the thermocline, which was not recorded by either ADCP or the remaining moorings. This occurs again on August 16, August 18, and August 21. The larger oscillations near the moorings compared to the ADCPs are consistent with the hypothesis that the moorings and ADCPs were positioned near the antinodes and nodes of

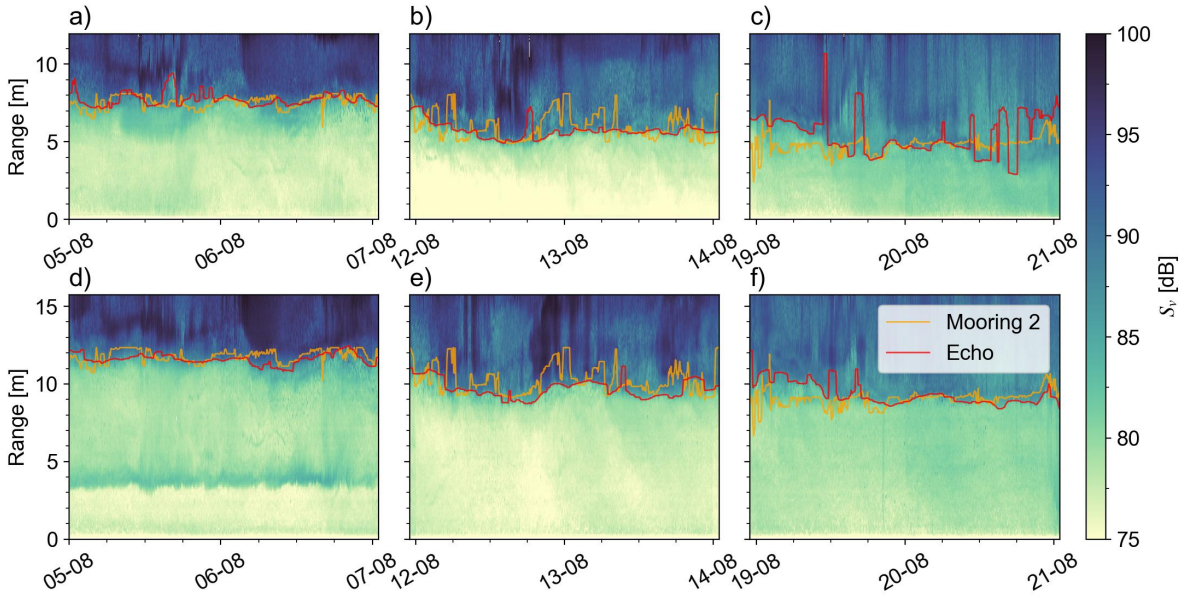


**Figure 4.10:** Interface between the top and bottom layer determined through the maximum gradient in volume backscatter. The interfaces that were tracked through the acoustic data are shown in red and the one tracked through mooring 2 in orange. We specifically selected several days based on the frequency analysis, but a version of the full record (showing each mooring) is provided in Figure F.5.

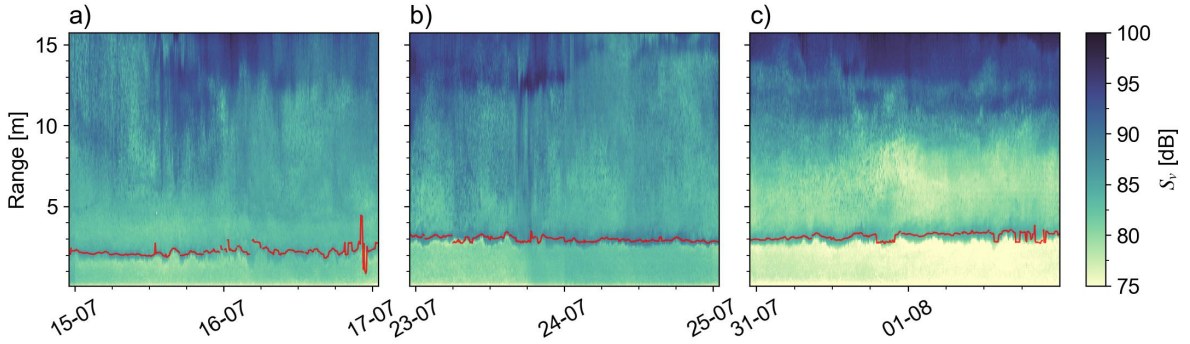


**Figure 4.11:** Lower interface recorded by ADCP6, determined through the maximum in volume backscatter. The interface that was tracked through the acoustic data is shown in red. Several days were specifically selected based on the frequency analysis, but a version of the full record is shown in Figure F.5.

internal seiching, respectively.

Finally, Figure 4.11 shows the layer close to the bottom, identified through maximum backscatter, and its performance over several days. A full version is provided in Figure F.5. Over the summer, it slowly increased in height before slowly disappearing from around August 5, causing this analysis to only include data up until August 1. At the start of the record on June 12, this layer seems relatively thick, with the backscatter maximum spread out over around $2$ meters. It gradually narrowed and became better pronounced, reaching a steady thickness on June 17. We noted in the previous section that, in one instance between July 20 and July 23, the bottom layer was accompanied by a second layer just above it, seemingly following it closely. We also observe this simultaneous occurrence when tracking the bottom layer, with a few jumps where the second layer constitutes a stronger maximum than the original layer. These jumps are negligible compared to other sets of outliers that sporadically occur from July 1 to July 18, one of which is shown in Figure 4.11a.

In summary, the interface was reliably detected and tracked under several conditions. The first condition is that a single well-defined thermocline must divide the water column into two layers (with no secondary layers). Secondly, this interface should exhibit the dominant gradient or maximum backscat-

**Table 4.1:** Phase speeds ($c$) and vertical velocity amplitudes ($\hat{w}$) derived from the CTD casts at TSO measurement points. We computed phase speeds for the first three internal seiching modes by solving Equation (2.11).

| Date | TSO location | $[c_1, c_2, c_3]$ [m/s] | | | $\hat{w}$ [m/s] |
|---|---|---|---|---|---|
| 24-06-2024 | 1 | $[0.121$ | $0.057$ | $0.035]$ | $0.205$ |
| | 2 | $[0.080$ | $0.034$ | $0.022]$ | $0.287$ |
| | 2 | $[0.099$ | $0.049$ | $0.033]$ | $0.224$ |
| | 2.5 | $[0.144$ | $0.070$ | $0.046]$ | $0.205$ |
| | 3 | $[0.156$ | $0.078$ | $0.049]$ | $0.174$ |
| 22-07-2024 | 1 | $[0.138$ | $0.055$ | $0.040]$ | $0.241$ |
| | 2 | $[0.121$ | $0.050$ | $0.032]$ | $0.246$ |
| | 2.5 | $[0.134$ | $0.063$ | $0.038]$ | $0.257$ |
| | 2.5 | $[0.140$ | $0.069$ | $0.046]$ | $0.275$ |
| | 3 | $[0.187$ | $0.083$ | $0.052]$ | $0.212$ |
| | 100 | $[0.162$ | $0.077$ | $0.046]$ | $0.202$ |
| | 101 | $[0.157$ | $0.060$ | $0.036]$ | $0.182$ |
| | 102 | $[0.161$ | $0.073$ | $0.046]$ | $0.165$ |
| 05-09-2024 | 1 | $[0.099$ | $0.037$ | $0.024]$ | $0.208$ |
| | 2 | $[0.106$ | $0.035$ | $0.021]$ | $0.222$ |
| | 2.5 | $[0.062$ | $0.022$ | $0.017]$ | $0.247$ |
| | 3 | $[0.150$ | $0.058$ | $0.035]$ | $0.238$ |
| | 100 | $[0.028$ | $0.015$ | $0.009]$ | $0.297$ |
| | 101 | $[0.069$ | $0.031$ | $0.017]$ | $0.256$ |
| | 102 | $[0.071$ | $0.032$ | $0.023]$ | $0.177$ |

ter. Tracking accuracy decreases when surface-induced spikes or other backscattering mechanisms interfere. Lastly, noisy spikes inherent in acoustic measurements must be removed ahead of tracking the interface and from the thermocline height series. We address the latter in the next section.

## 4.3. Oscillations of the thermocline

The interfaces found in the previous section show time-varying oscillatory behaviour. We analyze the signals in the time-frequency domain using continuous wavelet transform. We combine these separate analyses using the wavelet coherence transform. Firstly, we find the theoretical bandwidths of frequencies for specific oscillations.

### 4.3.1. Expected oscillation frequencies based on density profiles

In the previous chapter, we distinguished basin-scale internal waves and high-frequency internal waves. These are estimated as follows.

#### Basin-scale internal waves

As discussed in Section 2.2, internal seiching consists of two phases: 1) forced tilting and 2) free seiching. The characteristic frequency of 1) forced behaviour depends on the forcing. Resonant forcing is possible, but not necessary for tilting to occur. Phase speeds for 2) internal seiching were derived from the cast by numerically solving Equation (2.11). The phase speeds of the first three internal seiching modes are shown in Table 4.1. These phase speeds increase with stratification, as seen in the second campaign where phase velocities were largest (22-07-20204). The vertical velocity amplitude is $0.27$ m/s.

Since these phase speeds do not coincide with our analyzed time period (August), we also computed phase speeds using a two-layer model. The assumed temperatures, salinity, and layer heights are shown in Table 4.2, along with the computed phase speeds. The phase speeds computed using the two-layer model are generally higher than the numerically computed phase speeds. This is in part due to the assumed discrete jump, but also due to the increased layering that is generally present during August compared to other months.

We use the approximate minimum and maximum phase speeds to estimate a conservative bandwidth

**Table 4.2:** Phase speeds of the first internal seiching mode estimated using the two-layer model in Equation (2.10) for moorings 1, 2, and 3 on August 5 and 16, 2024.

| Date | Mooring | $T_1$ [°C] | $h_1$ [m] | $T_2$ [°C] | $h_2$ [m] | $S$ [PSU] | $c$ [m/s] |
|---|---|---|---|---|---|---|---|
| 05-08-2024 | 1 | 22 | 6 | 20 | 9 | 27 | 0.19 |
| | 2 | 21 | 6 | 19 | 9 | 27 | 0.18 |
| | 3 | 22 | 6 | 19 | 11 | 27 | 0.24 |
| 16-08-2024 | 1 | 23 | 9 | 20 | 6 | 27 | 0.24 |
| | 2 | 22 | 9 | 19 | 6 | 27 | 0.23 |
| | 3 | 23 | 9 | 19 | 8 | 27 | 0.29 |

for internal seiching. We use a minimum and maximum phase speed of $0.15$ m/s and $0.30$ m/s. These seem reasonable since phase speeds are expected to be higher than those in Table 4.1 due to the increased stratification during August as compared to the moments of the casts. The 2-layer model generally overestimates phase speeds due to the discrete density step, so this formed an upper bound for the phase speed. In summary, the seiching periods are estimated using a lower and upper bound of $0.15$ m/s and $0.30$ m/s alongside basin dimensions $2.5$ km and $500$ m (see Section 3.3), respectively. We round this to seiching periods between $1$–$10$ hours. We did not include estimates for the seiching period of the lower layer measured by ADCP6, as it did not appear in the mooring data or the CTD casts.

The inertial frequency is readily computed using a latitude of $51.55°$ and Equation (2.13) as $1.1 \times 10^{-4}$ rad/s, corresponding to a period of $15.3$ hours. While rotary currents at this frequency are not likely to be represented in the thermocline oscillations and geostrophic currents rarely occur in long, narrow basins, knowledge of the (near-)inertial frequency may still be important. Using the conservative seiching phase speed $0.15$ m/s, basin length $2.5$ km, and an inertial frequency $1.1 \times 10^{-4}$ rad/s, we find a Burger number

$$S_i = \frac{c}{fL} \approx 3.4,$$

indicating that Coriolis is unlikely to affect internal seiching. If we instead used the cross-lake length scale, $S_i$ would only increase, further confirming that Coriolis will not play a significant role.

#### High-frequency internal waves

High-frequency internal waves may principally take up any frequency between the buoyancy frequency and the inertial frequency. When approaching this higher bound, they are hard to distinguish from other internal wave types and/or forcing mechanisms, so we focus on the lower bounds of this bandwidth. The buoyancy frequency at the thermocline usually lies around

$$N = \sqrt{-\frac{g}{\rho_0}\frac{\Delta\rho}{\Delta z}} \approx 4 \times 10^{-2} \text{ rad/s},$$

corresponding to a period of $157$ seconds. This period is too small (compared to the sampling interval after averaging) to be resolved globally but may be identified during/after specifically identified events.

### 4.3.2. Frequency components in observed thermocline motions

We investigate the contribution of internal frequency components in the time-frequency domain through continuous wavelet analysis. Due to the required averaging and band-passing for outlier removal, we do not resolve high-frequency internal waves with a lower bound wave period of $157$ seconds, so this analysis is split into a daily component and the approximate bandwidth of basin-scale oscillations, which was established at $1$–$10$ hours. For each of these bandwidths, we first discuss instances of high wavelet power in the wavelet spectra (Figures 4.12 to 4.16) at the frequency band of interest. We then consider the coherence and phase between different signals by treating several examples but refer to Appendix G for a comprehensive overview of the coherence between all the signals.

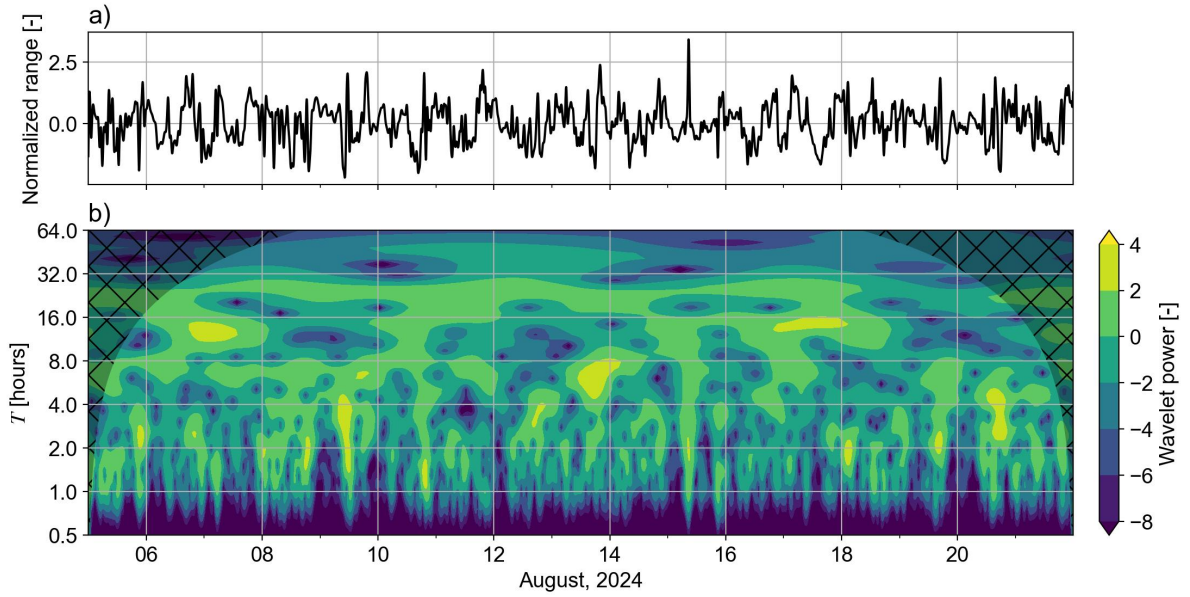


**Figure 4.12:** CWT of the tracked interface time series measured by ADCP3. We show the a) outlier-removed, de-trended, normalized time series of interface heights and b) the wavelet spectrum, indicating Fourier periods on the vertical axis and time on the horizontal axes.

### Daily oscillations

A daily oscillation is expected in each signal, corresponding to the solar forcing cycle. The strength of this component likely depends on the solar forcing itself or the oscillation of a related scatterer.

This frequency component appears in all signals, though more prominently in some than others. The strongest daily oscillation is expected at mooring 3, located in the shallower part of the lake. We confirm this with Figure 4.16, which shows the continuous presence of wavelet power around the daily frequency during the first half of the record. Interestingly, mooring 2 also exhibits a daily component (Figure 4.15), though not necessarily simultaneously with mooring 3. ADCP3 shows it as well, particularly during early August, peaking on August 11 (Figure 4.12). Similarly, ADCP6 displays a daily component, strongest between August 12 and 18 (Figure 4.13). Mooring 1 exhibits this oscillation throughout most of the record (Figure 4.14) while mooring 2 primarily shows it in the latter half of August.

If solar insolation is the dominant forcing mechanism of the thermocline, the signals should exhibit a coherent daily component with the same phase, as heat input from the sun is uniform across the lake. We proceed by analyzing this coherence.

Here, we provide several examples of strong coherence at the daily frequency. The bulk of the visualizations corresponding with these is found in Appendix G. We observe a strong coherence at the daily frequency between August 10 and 14 between ADCP3 and mooring 1 (Figure 4.18a), with both signals in phase—despite these devices being the farthest apart. Other instances of in-phase, increased coherence, though slightly weaker, include August 10–12 (ADCP3–mooring 3; Figure 4.17a), August 12–14 (ADCP3–ADCP6), and August 18 (ADCP6–mooring 2). Between August 18 and 20, moorings 2 and 3 show a coherent daily oscillation, but with an out-of-phase difference of $\pi$ rad. Additional coherent daily oscillations occur at other phase lags and are summarized in Table G.1.

### Higher frequencies

The second frequency band of interest is the band associated with internal seiching. We estimated the free oscillation frequency of internal seiching between $1$–$10$ hours. We focus primarily on the first mode and, where possible, cautiously consider the second mode, since identifying higher modes in the signal becomes increasingly difficult due to wavelet power leakage from high frequencies (i.e., noisy peaks at the lower end of wavelet spectra, for example on August 15 in Figure 4.12). We expect free oscillations to be preceded by a forced oscillation. Previous research has shown a large variation in forcing periods, ranging from $20$ to $400$ % of the first internal seiching mode. As a result, we do not explicitly analyze

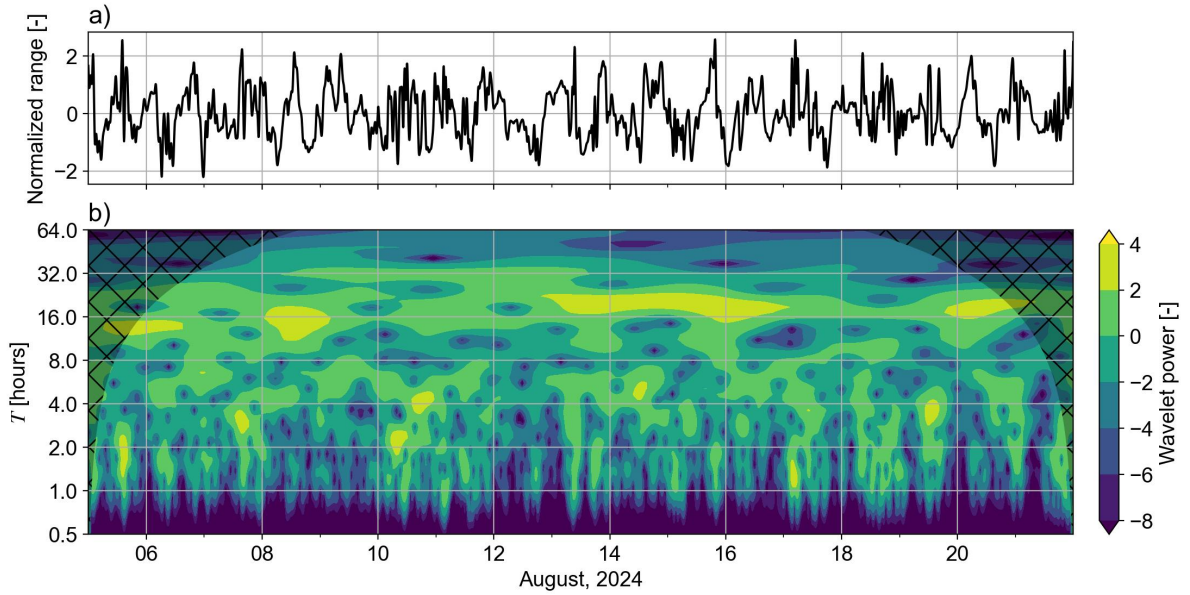


**Figure 4.13:** CWT of the tracked interface time series measured by ADCP6. We show the a) outlier-removed, de-trended, normalized time series of interface heights and b) the wavelet spectrum, indicating Fourier periods on the vertical axis and time on the horizontal axes.

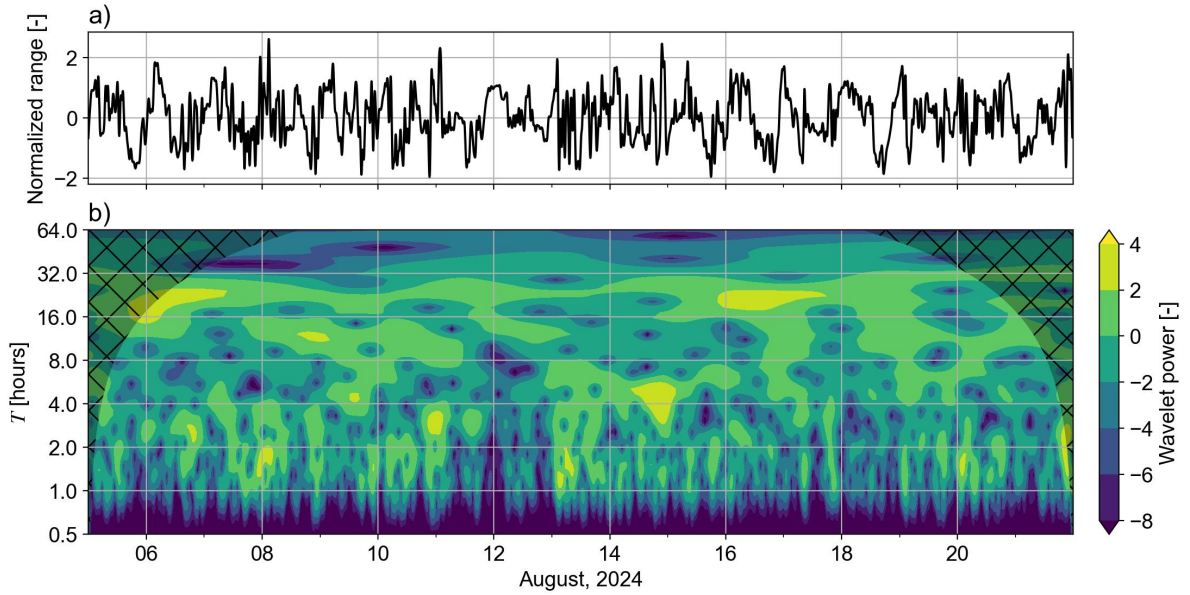


**Figure 4.14:** CWT of the tracked thermocline time series measured by mooring 1. We show the a) outlier-removed, de-trended, normalized time series of interface heights and b) the wavelet spectrum, indicating Fourier periods on the vertical axis and time on the horizontal axes.

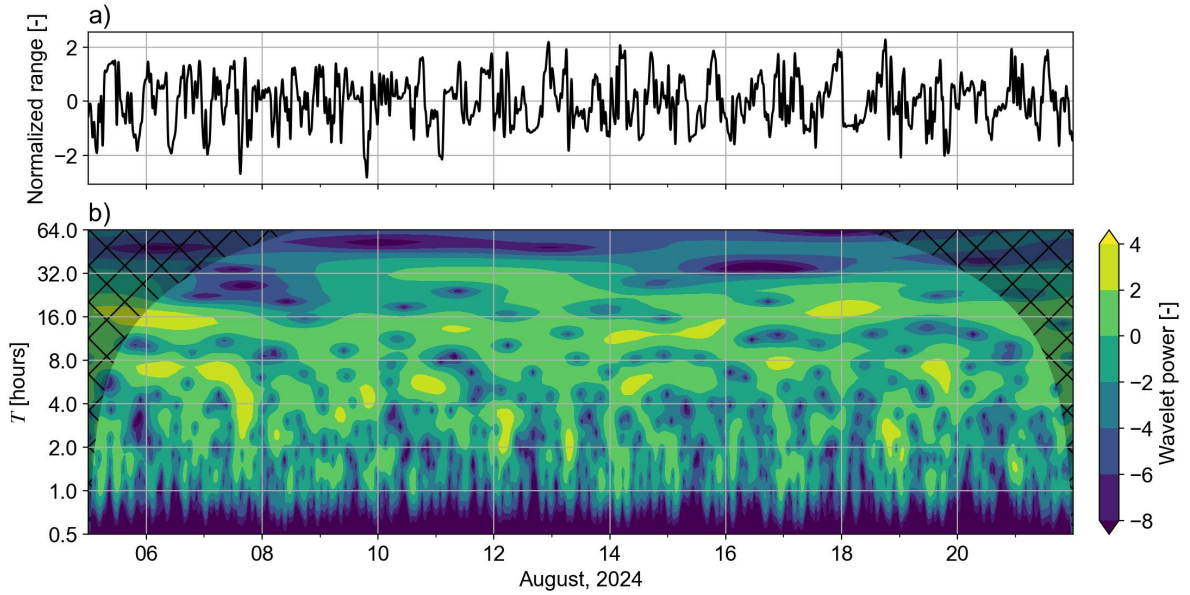


**Figure 4.15:** CWT of the tracked interface time series measured by mooring 2. We show the a) outlier-removed, de-trended, normalized time series of interface heights and b) the wavelet spectrum, indicating Fourier periods on the vertical axis and time on the horizontal axes.

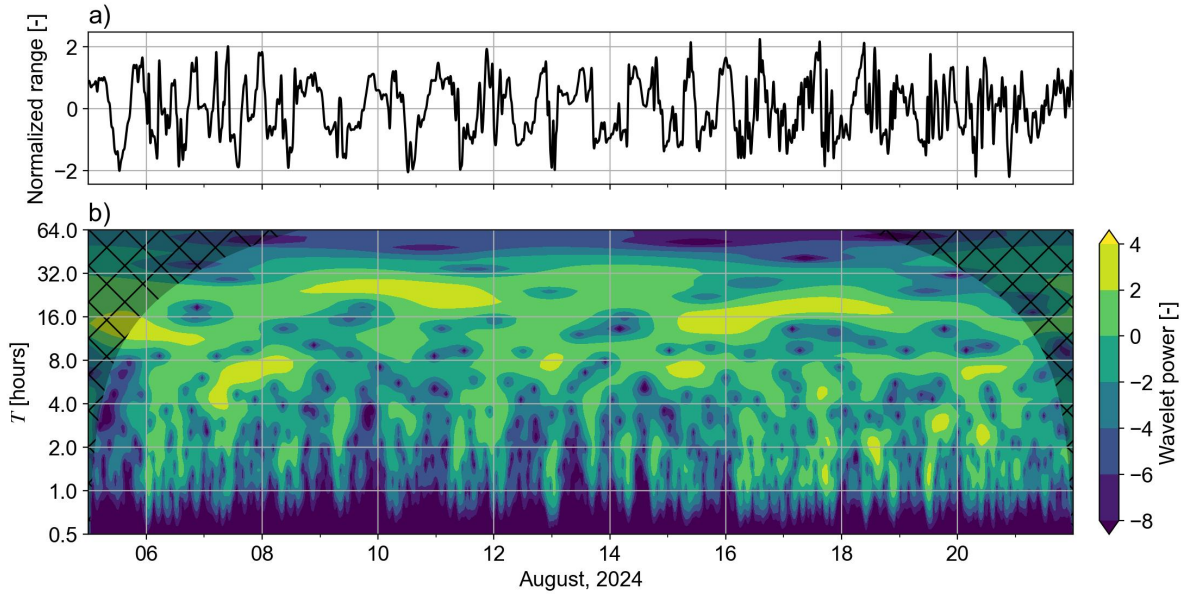


**Figure 4.16:** CWT of the tracked interface time series measured by mooring 3. We show the a) outlier-removed, de-trended, normalized time series of interface heights and b) the wavelet spectrum, indicating Fourier periods on the vertical axis and time on the horizontal axes.

this period but verify its presence in hindsight in the volume backscatter (and/or wavelet spectra).

We observe many instances of increased wavelet power for each signal in the $1$–$10$ h band. We summarize the most important findings. ADCP3 exhibits increased wavelet power at approximately $7$ hours for a large part of the record (see Figure 4.12). We find this increase in ADCP6, too, albeit at approximately $6$ hours (see Figure 4.13). This component is also often seen in moorings 2 and 3 (see Figures 4.15 and 4.16), but not in mooring 1 (see Figure 4.14).

The large bandwidth leads to many examples of high coherence, which we summarized in Table G.1. We now diverge into cross-lake and along-lake internal seiching, which we identified through coherent and out-of-phase frequency components between mooring 3 and ADCP3 and between mooring 1 and ADCP3, respectively. We validate these observations with velocities in the next section.

We hypothesized that cross-lake internal seiching would occur between mooring 3 and the ADCPs or mooring 2. Wavelet coherence and phase between ADCP3 and mooring 3 reveal several instances of increased coherence with a $\pi$ rad phase lag, which we highlighted in Figure 4.17a,b. Notably, from August 6–8, an 8-hour component exhibits strong coherence and a $\pi$ phase lag (Figure 4.17), aligning with backscatter patterns (Figure 4.17c) that suggest oscillations following a downward interface movement on August 6. Similar patterns appear on August 11–13 and August 20–21. While backscatter in Figure 4.17d,e confirms oscillations during these periods, they are not always reflected in coherence with other cross-lake signals. The August 20–21 event lacks coherence in cross-lake signals but appears between mooring 1 and 3 (Figure G.11e,f), suggesting an along-lake component. Other instances of high coherence (e.g., August 9 at $T = 4$ h, August 16 at $T = 2$–$4$ h) have near-zero phase lag and are not classified as internal seiching.

In the along-lake direction, internal seiching is expected to occur along the main channel, most likely between mooring 1 and the ADCPs or mooring 2. Similarly to our cross-lake analysis but using mooring 1 and ADCP3, we show the wavelet coherence and corresponding phases in Figure 4.18a and b, respectively. Again, we highlighted several areas of increased coherence. On August 10, an $8$-hour oscillation appears with a $\frac{3}{4}\pi$ phase lag. On August 16, two simultaneous oscillations (12- and $6$-hour periods) emerge but are not clearly seen in other signals. Between August 19–21, two consecutive $6$-hour oscillations are observed, first out-of-phase, then in-phase. These oscillations are also evident between mooring 1 and ADCP6 and between moorings 1 and 2 (Figure 4.14c–f).

In summary, we observed presumed cross-lake internal seiching with periods of approximately $4$–$6$ hours and along-lake internal seiching with longer periods of $6$–$8$ hours. We highlighted these in Figures 4.17 and 4.18 and in the windowed Fourier spectra of the signals which we added as supplementary material (see Figures G.1 to G.5). We proceed by validating the internal seiching events through velocity measurements.

### 4.3.3. Consistency of thermocline motions with flow velocities

In previous sections, we identified key periods and bandwidths of interest, highlighting events of increased wavelet coherence. We now analyze measured velocities during these periods, first directly and then after band-passing ($1$–$10$ hours) to isolate internal processes. In theory, internal seiching is caused by velocities above and below the thermocline being out of phase (i.e., being positive and negative or vice versa; Figure 2.3). After analyzing the periods of cross/along-lake seiching, we examine velocities near the bottom layer (ADCP6). Finally, we explore the coincidence of shear with the thermocline.

#### Internal seiching

In the cross-lake direction (Figure 4.17f–h), following a thermocline descent on August 6, we observe slightly out-of-phase velocities measured by ADCP3 above and below the thermocline, confirmed after band-passing (Figure 4.17i). This is further supported by the band-passed cross-lake flow velocities measured by ADCP6 (Figure 4.19a). The velocities above and below the thermocline are out of phase, suggesting a more complex vertical structure than a simple two-layer system. During August 11–14 (Figure 4.17g), a large thermocline displacement is followed by out-of-phase velocities, persisting for 1–2 oscillations after which a longer-period motion dominates. Band-passed velocities (Figure 4.17j) suggest the oscillation dissipates quickly, consistent with wavelet coherence findings. Between August 19–21, another thermocline descent (Figure 4.17e) is followed by brief oscillations, also seen in the

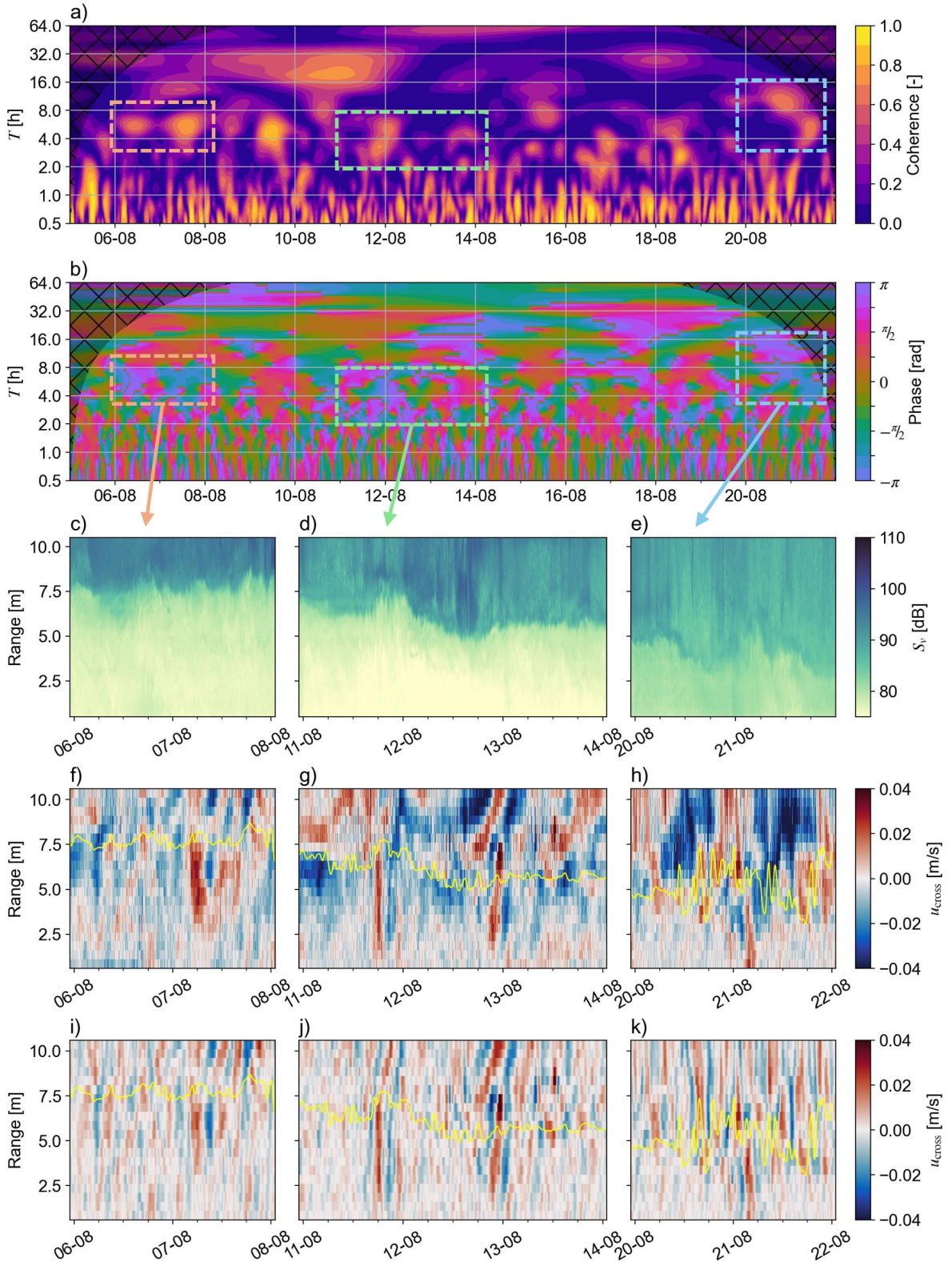


**Figure 4.17:** Cross-lake internal seiching analysis, consisting of a) the wavelet coherence spectrum between ADCP3 and mooring 3 and b) the corresponding phase lags. Plots c), d), and e) show the volume backscatter recorded by ADCP3 during the highlighted periods and plots f), g), and h) the corresponding cross-lake velocities (positive northeast). We band-passed these velocities between $1–10$ hours and show them in plots i), j), and k). In plots f)–k), we indicate the interface tracked through the volume backscatter in yellow.

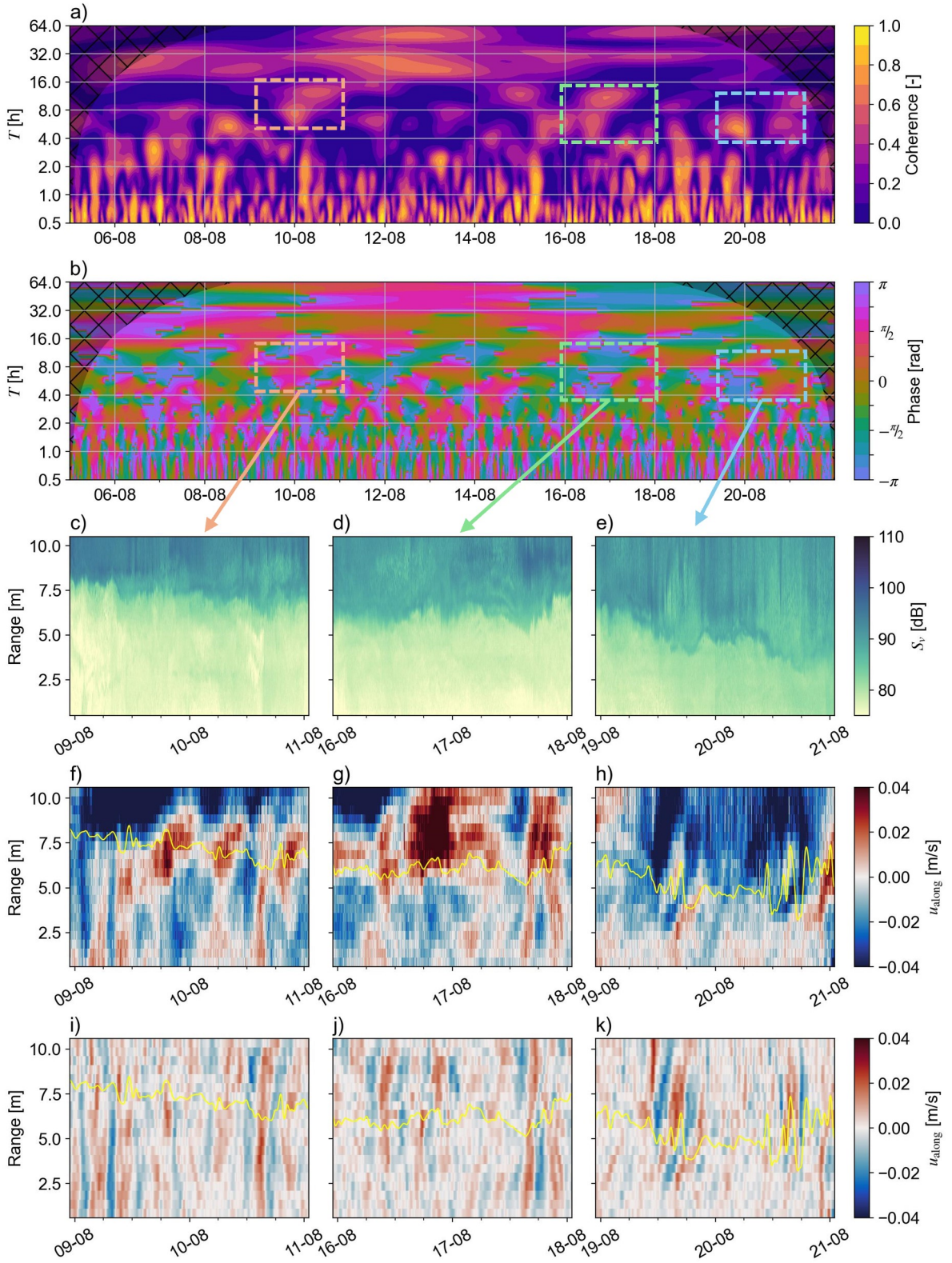


**Figure 4.18:** Along-lake internal seiching analysis, consisting of a) the wavelet coherence spectrum between ADCP3 and mooring 1 and b) the corresponding phase lags. Plots c), d), and e) show the volume backscatter recorded by ADCP3 during the highlighted periods and plots f), g), and h) the corresponding along-lake velocities (positive northwest). We band-passed these velocities between 1–10 hours and show them in plots i), j), and k). In plots f)–k), we indicate the interface tracked through the volume backscatter in yellow.

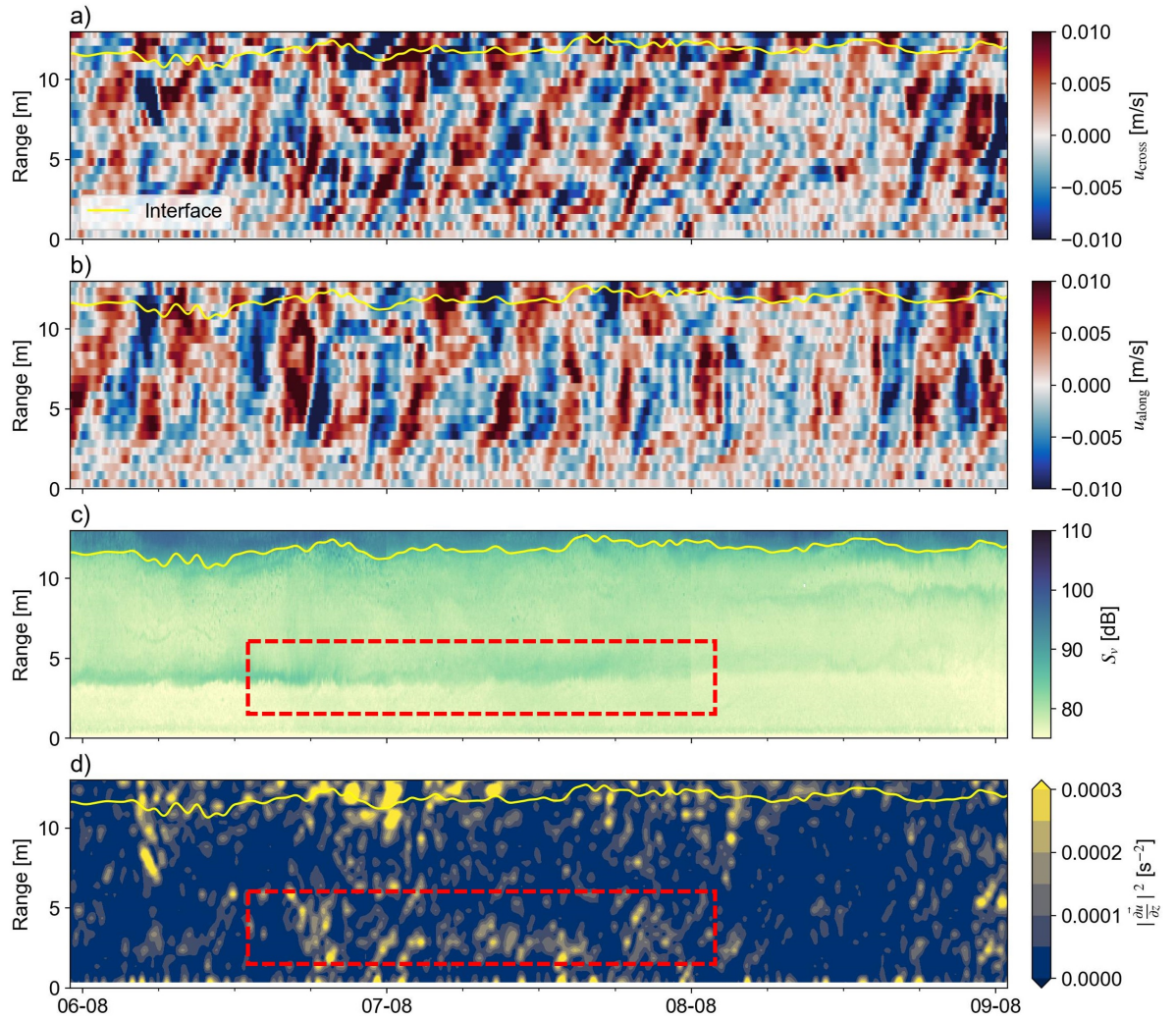


**Figure 4.19:** a) Cross-lake (northeast positive) and b) along-lake (northwest positive) velocities band-passed at 1–10 hours on August 6–8. This period was selected based on wavelet coherence and likely contains internal seiching. The tracked interface is shown in yellow. We also show c) the volume backscatter and d) the magnitude of the vertical velocity shear during the same period. Coincidentally, August 6–8 was the period during which the bottom layer disappeared, which we highlight in red.

band-passed data (Figure 4.17k), again consistent with our previous findings. We observe negative velocities above the thermocline, consistent with the larger period motion in the third highlighted area in Figure 4.17a, followed by a shorter period oscillation that is subsequently observed in the coherence spectrum, too.

In the along-lake direction, we show the measured velocities in Figure 4.18f–h. Generally, along-lake velocities are larger than cross-lake. Between August 9–11, we observe out-of-phase velocities, but without 2-layer behaviour (Figure 4.18f,i). After band-passing, the water column behaves uniformly, inconsistent with the hypothesized internal seiching for which velocities should be out-of-phase above and below the thermocline. From August 16–18, we observe out-of-phase velocities for a longer duration, followed by a shorter duration motion that is also observed after band-passing (Figure 4.18g,j). Finally, on August 19, we observed a larger downward motion (Figure 4.18e). Here, a large thermocline descent coincides with a back-and-forth motion confined to the upper water column, suggesting the thermocline rebounded after being forced downward.

### Oscillations of the bottom layer

We proceed with a brief analysis of the velocities we observed near the bottom layer. The continuous wavelet analysis of the bottom layer indicated wavelet power in a daily component, sporadically in a

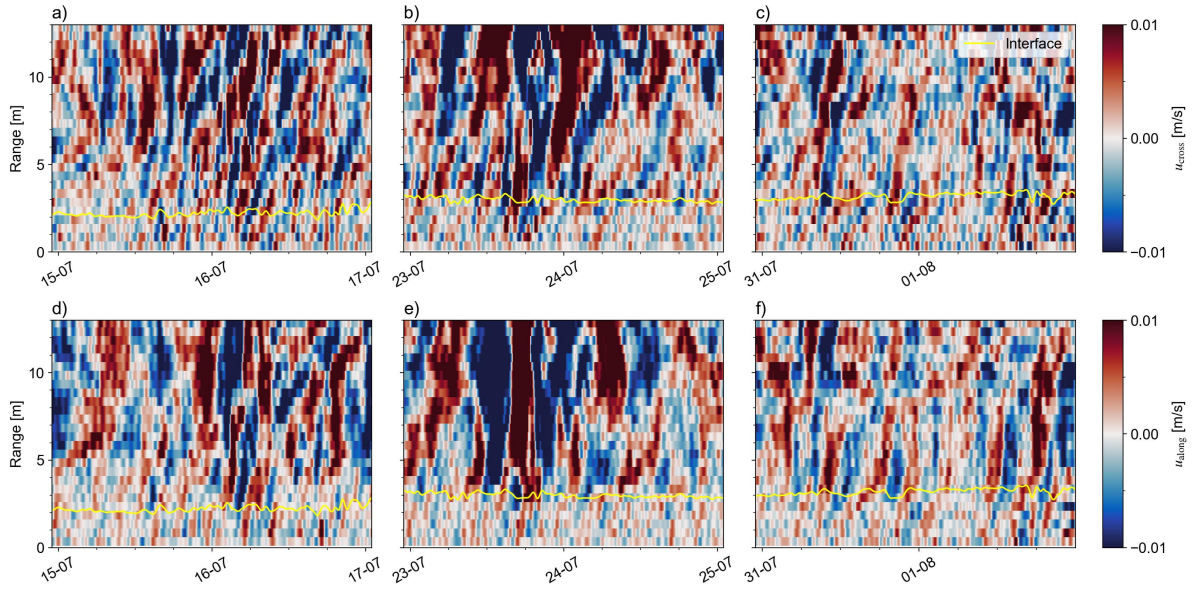


**Figure 4.20:** Cross-lake (a, b, c; positive northeast) and along-lake (c, d, e; positive northwest) velocities in the presence of a deeper layer. The deeper, tracked interface is plotted in yellow. Velocities are band-passed at $1$–$16$ hours.

semi-daily component, and in the band between $2$–$8$ hours (also refer to Figure G.6). We only include observations of this layer when it reaches above $1$ m from ADCP6 because velocities in the first bin are often artificially high. This complicates observations when the lower interface measured by ADCP6 is close to the bottom but is somewhat circumvented by band-passing the velocity signal between $1$–$16$ hours.

Generally, surface-driven velocities rarely reach the bottom, but several exceptions exist (Figure 4.20). Large velocities often do not penetrate the interface, indicating strong stratification. On July 15 and June 16 (Figure 4.20a), the interface moves upward when cross-lake velocities are negative (southwest), and downward with positive (northeast) velocities, consistent with ADCP6's location on a pit's southwestern side. During this time, we observe increased wavelet power at a period of $5$ hours. Similar patterns appear in the velocities on July 24 and 31 (Figure 4.20b,c) also with wavelet power at a period of $5$ hours. Conversely, Figure 4.20d,f show interface displacement opposite to expectations for along-lake velocities, which we discussed in the next chapter. Here, wavelet power was increased in $6$–$8$ hours–band.

We highlighted the disappearance of the lower layer from acoustic measurements in Figure 4.19c,d. During this time, increased shear is observed around this layer, either eroding the stratification or re-suspending the accumulated matter. Despite its disappearance, we still observe the dampening of velocities towards the right of Figure 4.19a,b.

# 5
# Discussion

In this chapter, we provide interpretations of the results obtained in the previous section and place them into the scientific context. We divide this into two parts. Firstly we discuss the potential for acoustic observations in former estuaries, focusing on monitoring thermal stratification. Secondly, we analyze the observed internal processes and hypothesize about forcing mechanisms, while also reflecting on using continuous wavelet analysis to identify these internal processes.

## 5.1. Acoustically observing stratification in former estuaries

Former estuaries, where dynamics resemble lake dynamics but are influenced by estuarine bathymetry and salinity, are complex sites with many potential processes responsible for acoustic backscatter. We found that the thermocline could be tracked well through acoustic backscatter but have established that the backscatter gradients are not directly associated with thermal stratification. In this section, we first discuss the applied method for inferring interfaces from acoustic backscatter, exploring caveats and possible improvements. We then discuss the responsible backscatter mechanisms (and other interfering mechanisms), how these affected our measurements and methods, and the implications for measuring stratification by leveraging these backscatter mechanisms and how this extends to other sites. Finally, we discuss the distinction between thermal and salinity stratification in acoustic measurements.

### 5.1.1. Inferring interface heights from acoustic data

We tracked multiple interfaces based on two possible mechanisms (also see next section): either a difference in suspended material concentration between layers (indicated by the maximum backscatter gradient) or the accumulation of suspended material at a pycnocline (indicated by a maximum backscatter). These interfaces served as proxies for thermocline height. The accuracy of this approach depends on several factors, including how well these constituents represent interface height, the assumptions involved in dividing the water column into two layers, the impact of noise (by other layers or scatterers), and deviations in the speed-of-sound profile. Finally, we briefly discuss alternative acoustic methods based on vertical velocity shear, which we were unable to consistently use for tracking the thermocline height.

In Section 4.2.2, we observed the relatively close correspondence between the interfaces from the acoustic and the mooring data. The largest deviations between interfaces were generally at sub-daily timescales, and interfaces generally converged to the same heights. At larger timescales, the different signals often exhibit high coherence with zero phase lag (see Figures G.7, G.8 and G.10), demonstrating long-term agreement between signals and forcing mechanisms. Short-term discrepancies are often observed as discrete steps, likely caused by the accidental tracking of a sporadic layer in the acoustic method (or the direct temperature method) or by the vertical resolution of temperature sensors on the thermistor chain.

We divided the water column into two layers, both when deriving interface heights from the acoustic data and the temperature moorings. While other interfaces were sporadically visible in the acoustic data, none persisted for long enough to warrant separate tracking besides the long-term lower layer. The division of the water column into two layers seems reasonable when considering the casts in Figures D.1 to D.3. A thermocline generally divides the water column into two parts, especially in the northwestern part of the lake. The maintenance of a strong thermal stratification is hampered by the frequent overturning during the summer, with two large overturns recorded (June 10 and late August),

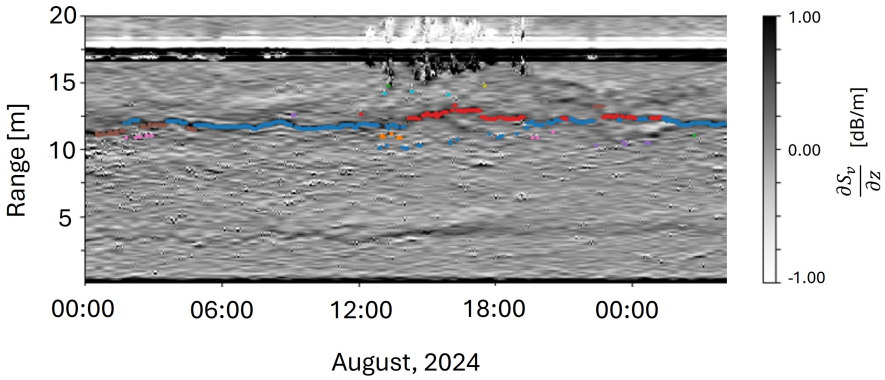


**Figure 5.1:** One of our earlier attempts at distinguishing interfaces in echograms. We plotted the vertical gradient of volume backscatter at $1000$ kHz recorded by ADCP6 on August 7–8. We show each interface in a different colour. We distinguished between interfaces using makeshift thresholds for the maximum time between an interface disappearing and a new point being added and the maximum vertical distance before a "new" interface is constructed. Points were sorted by vertical differences with the previous interface to find the next point most likely associated with an interface.

decreasing the chance of a strong stratification developing and thereby complicating the tracking of the thermocline. As mentioned, the sporadic existence of additional layers in both the acoustic and temperature observations was responsible for many of the discrepancies and noise in the tracked interfaces. In summary, the stronger the (main) thermocline, the more it dominates over secondary layers, leading to more robust tracking, especially in the direct method of inferring thermocline heights from temperature measurements.

The sporadic interfaces in the acoustic data were often noisy and hardly stood out from the rest of the profile. This introduced another challenge when automatically tracking the thermocline. Much literature has focused on deriving the thermocline height from temperature data, while little has focused on tracking interfaces from acoustic data. Tracking the interfaces based on arbitrary thresholds for prominence and minimum peaks (in the dB domain) often faced issues due to the non-stationarity of the signal, likely requiring some form of adaptive thresholding. We approached this through time-dependent thresholds based on the geometrical standard deviation (Shibley et al., 2020), but our scaling factors remained constant.

To incorporate the distinction between separate layers (i.e., secondary layers), we require, again, arbitrary thresholds for the distance between layers, the minimum duration (to filter out fish), and the maximum time between subsequent points. This is illustrated in Figure 5.1, which showcases how maximum gradient tracking performs under these arbitrary thresholds. In tracking these, we did not leverage the value of the backscatter, only the peak location. The exact value of the gradient maxima was prone to large variations, especially in the presence of storms, complicating this problem. In the end, we opted to low-pass the time series to reduce the effect of outliers and noise in global maxima, but this operation did not always reduce the effect of a sporadic layer, which may exist for longer than the higher frequency threshold of this filter.

Our method for inferring internal oscillations was similar to methods by Shibley et al. (2020) but, as mentioned, complicated by the difficulty of discerning interfaces. While isotherms have historically been used directly for frequency analysis (e.g., Saggio and Imberger, 1998, 2001), frequency analysis of thermoclines has seen fewer applications. This is likely because thermocline tracking can be inconsistent due to temperature fluctuations or the presence of stronger gradients elsewhere. In many cases, oscillations resulting from the temporary tracking of a different gradient dominated the wavelet spectra, necessitating confirmation through velocity measurements. Noisy peaks often occurred simultaneously in different signals, leading to increased (but spurious) wavelet coherence. Consequently, our method would likely be ineffective when relying on a single echosounder without concurrent validation data (i.e., velocities).

High-frequency outliers, such as those in Figure 4.10c were filtered using a low-pass filter. These outliers were introduced when other mechanisms than plankton (see next section) concentration dom-

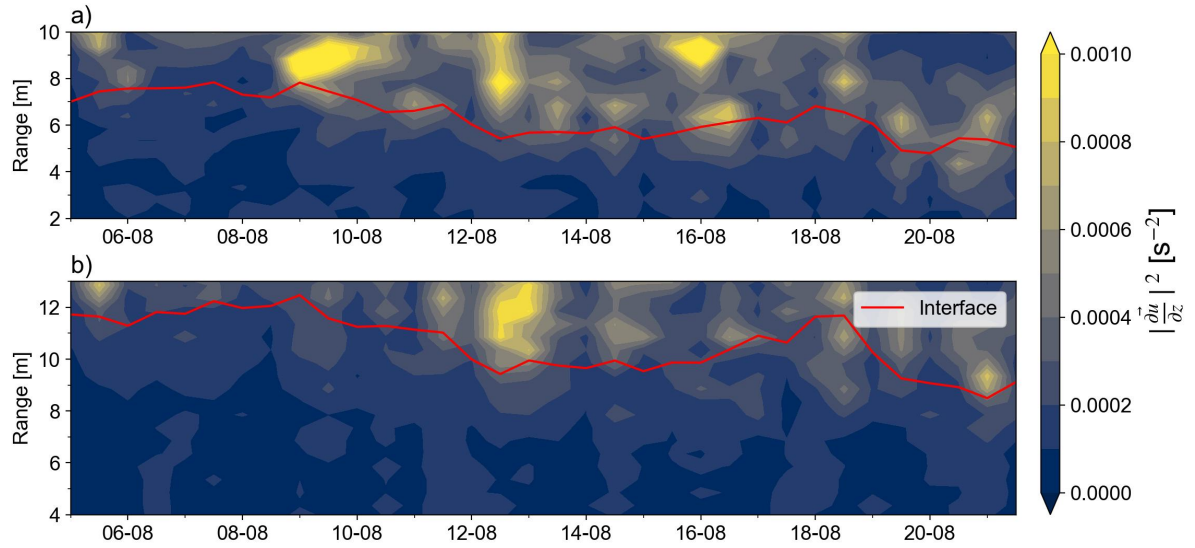


**Figure 5.2:** Semi-daily averaged shear in August, measured by a) ADCP3 and b) ADCP6. We excluded parts of the water column that were influenced by sidelobe interference and the parts close to the ADCPs. In red, we indicated the interfaces as determined from the acoustic backscatter.

inated the backscatter. We mainly attribute this to storms, i.e., bubbles in combination with increased shear. The shear erodes the thermocline, reducing the magnitude of the gradient. Simultaneously, bubbles are injected into the water column, leading to increased gradients above the thermocline, also visible in Figure 4.10c,f, where a reduced gradient combined with noise in the upper water column introduced an increased number of outliers. The high-frequency noise also introduced high wavelet power in the spectra, complicating inferring internal processes with periods smaller than several hours.

Speed-of-sound gradients effectively change the cell size used in acoustic measurements, causing a misalignment between the assumed and actual grid of several meters in deep ocean applications (see Appendix C.1). We found a maximum cell size variation of $1.5$ %, mainly a decrease, amounting to $15$ cm over the full water column. The largest deviation occurs at the top, where temperatures are highest and most uncertain. While precise speed-of-sound corrections may improve certain highly accurate measurables (e.g., bathymetry; Mohammadloo et al., 2019), discrepancies in the variable grid relative to the inferred thermocline height (and its noise) are minor and do not affect the subsequent frequency analysis. Future improvements may warrant the use of accurate temperature data at the echosounder location or apply standard corrections (that is, $r_{\text{new}} = r \times \frac{\text{nominal sound speed}}{\text{estimated sound speed}}$) to improve estimations.

Other acoustic methods for monitoring stratification have utilized maximum shear, leveraging the dominance of the thermocline in the shear distribution (Macrander et al., 2007; Simpson et al., 2021) or isolating specific frequencies through band-passing (Brenner et al., 2023). Furthermore, Simpson et al. (2021) found that daily averaged vertical shear aligns well with the thermocline, suggesting longer averages can still indicate its general location, albeit with lower temporal resolution. However, these methods remain unconfirmed, as shear maxima often appear above the thermocline (especially for ADCP6, see Figure 5.2b). We observed shear generally confined between the surface and thermocline, though ADCP3 occasionally showed maximum shear at the thermocline (see Figure 5.2a), suggesting different dominant forcing mechanisms between the ADCPs, likely due to ADCP6's proximity to the tidal channel.

In summary, the largest challenge in our method of inferring the thermocline height from acoustic data is the relative importance of coexisting scattering mechanisms and layers. Minor improvements could be made using speed-of-sound profiles, but major benefits could be attained through a more robust algorithm that leverages the backscatter magnitude and height, which we discuss in Section 7.2. In the next sections, we discuss the different scattering mechanisms which contributed (and/or convoluted) the measurements and thereby affected the thermocline observations.

### 5.1.2. Dominant backscatter processes

We found that backscatter by the $1000$ kHz pulses is best received by the ADCPs. This is attributed to several (potential) factors. First and foremost, the water column contains more scatterers specific to this frequency. Secondly, the transmission of acoustic pulses by the Signature1000 is optimized for $1000$ kHz and is less efficient at the other frequencies. This seems plausible due to the $1000$ kHz-specific transducer but lies outside the scope of this research. Finally, the noise floor of the $500$ kHz signal is relatively high compared to other studies using the same device (e.g., Jaarsma, 2023), leading to a larger portion of the signal being marked as noise.

During August, the volume backscatter of the $1000$ kHz signal shows a large step between the upper and lower layers, indicating an increase in the concentration of a specific constituent between these layers. This is also observed in the raw $500$ kHz signal, but is apparently frequency dependent. The minimum scattering size for a $1000$ kHz pulse is $24$ µm and increases by a factor 2 as frequency decreases with a factor 2 (refer back to Table 2.1). At this frequency, the (relatively smaller) scatterers are often identified as types of plankton. For example, very close to (but below) the surface, Warren et al. (2003) also recorded an increase in backscatter with frequency, which they associated with biological targets through direct measurements. Primary production (i.e., photosynthesizing phytoplankton) in Lake Veere is generally at a maximum in August (Prins et al., 2023). In parallel, backscatter in the upper water column increases towards (and into) August, following a temperature increase after a generally cold, wet summer. Therefore, backscatter in this layer is likely associated with an increasing phytoplankton concentration.

Phytoplankton occupies a diameter range of around $20$–$200$ µm (Gro Vea Salvanes et al., 2018) and are therefore a likely explanation of the increase in backscatter with frequency in the upper layer, an observation also made by Lavery et al. (2010). This is in line with available measurements of phytoplankton, with phytoplankton most abundant in the diameter range $< 10$ µm (see Section 2.4). Most observed plankton species are only observed through the $1000$ kHz channel, of which $24$ µm is the smallest resolvable scale, demonstrating that an increase in frequency may benefit the observations. The raw data from the $250$ and $500$ kHz channels was excluded from further analysis, as they exhibited the same trends as the $1000$ kHz channel but with relatively more noise (or a relatively weaker signal). At this point, we conclude that this was due to low concentrations of scatterers with diameters of at least $48$ µm (see Table 2.1). Wetsteyn (2004b) showed that (before the commissioning of Katse Heule), the zooplankton size distribution remained almost exclusively below $60$ µm, with most zooplankton even below $40$ µm and phytoplankton generally smaller still. Given these findings, the $250$ and $500$ kHz channels are unlikely to be effective for monitoring stratification through plankton in future lake studies.

Despite the generally low signal strength in the $250$ and $500$ kHz channels, we can still qualitatively infer scattering mechanisms using frequency-dependent scattering. For example, surface width increases with frequency, likely due to enhanced scattering by strong acoustic impedance gradients (between water and air). We previously established the expected increase of backscatter by impedance gradients with decreasing frequency. Similarly, bubbles constitute large impedance gradients, which explains why the lower frequencies record a wider surface, especially during storms when surface waves inject more bubbles into the water column. These bubbles resonate at frequencies of 10s and 100s of kHz (Bassett et al., 2023), which explains the increased sensitivity of lower frequencies to the surface. While turbulence-induced backscatter theoretically diminishes beyond $100$ kHz and nears zero at $400$ kHz (Goodman, 1990; Warren et al., 2003), a passing boat triggered a $10$-minute period of increased backscatter in the $1000$ kHz signal (see Figure F.4). This suggests that injected bubbles, rather than turbulence, were responsible.

The persistent lower layer recorded by ADCP6 represented a local backscatter maximum rather than a gradient. Over the summer, the lake became progressively saltier, pointing to a net import of saltwater. CTD measurements from this study, along with TSO data from RWS, indicated that dense salt water from the Eastern Scheldt intruded into Lake Veere, propagating along the bottom and accumulating in local pits (Figures 1.2 and 4.1 to 4.3). ADCP6 is situated in one such pit, near the deep tidal channel that transports this saline water. This suggests that the observed backscatter maximum corresponds to a halocline. Impedance gradients (which also constitute backscatter maxima) are an unlikely explanation for the backscatter maximum at this hypothesized halocline. The measured backscatter could not be attributed to the theoretical reflection coefficients, even though these are generally of the same or a

higher order of magnitude than in literature (Bassett et al., 2023; Stranne et al., 2017). This is at least in part attributed to a lack of co-located data, but a more plausible explanation for the backscatter maximum is the accumulation of sinking suspended matter or plankton on the strong density gradient. This aligns with findings by Haught et al. (2024), who observed an accumulation of algae and nekton on a pycnocline in an estuary. A similar backscatter maximum on August 23–25 may have resulted from a storm-induced increase in sedimentation, with turbulence mixing suspended particles downward onto the pycnocline. However, the gradual disappearance of this layer in early August remains unclear.

Besides the observed frequency-dependence of the backscatter, several seemingly interfering patterns are recorded by the ADCPs. ADCP3 records a line at a range of approximately $19$ meters ($= r_{\text{surface}} + 6$ m) on the $250$ and $500$ kHz channels (Figure 4.5). This line is not contained to periods of stratification but occurs continuously throughout the entire record and its height seems to increase during periods of increased backscatter at the surface. It may be an interference pattern caused by the pulses being reflected between the surface and the bed, but the exact process is unclear, and it is not expected to affect our method of deriving thermocline height, since it is located above the surface. Besides this, an interference pattern is recorded close to the echosounder by, again, the $250$ and $500$ kHz channels. We observe this pattern as several straight, parallel bands of increased backscatter, occurring for a few tens of centimetres for ADCP6 (a little further for $250$ than $500$ kHz) and up to several meters for ADCP3. We hypothesize that, at times, the ADCP was submerged by mud and these lines constitute the reflection between the mud and water, which is measured several times as the pulse is echoing between the ADCP and this interface. However, mud-water transitions are generally gradual, so other factors may also be responsible. We did not find occurrences where this interference affected the tracking of the deep layer from ADCP6. However, since the interference was strongest for ADCP3, this may affect future measurements, if a deep layer coincides with the interference.

As discussed, the $500$ kHz channel operated close to the noise floor, with even conservative estimates (e.g., $12$ dB) introducing problems with low $SNR$s (refer to Figure F.3). Bassett et al. (2023) encountered a similar problem with a high noise floor in broadband measurements. Here, narrowband electrical noise resulted in spikes, increasing the noise floor. These spikes were not necessarily found in our data, which can be attributed to the small possibility of overlap between a narrowband noise spike and a narrowband acoustic pulse. However, a possible interaction of electrical noise with the $250$ and $500$ kHz channels cannot be ruled out.

As discussed, only a small range-dependence is observed in the raw $500$ kHz channel, close to the ADCP, but the signal does not reduce beyond this. This behaviour is expected, since the $500$ kHz attenuates slower. After conversion to volume backscatter, it seems like we introduce a range-dependence, instead of removing it (compare, for example, Figures F.1 and F.2). The spherical spreading $20 \log_{10} r$, an established term, introduces the range-dependence of this channel but the reason for this remains unclear.

In Chapter 2, we demonstrated the approximately equal contribution of temperature and salinity to acoustic impedance in the ranges relevant to Lake Veere (see Figures 2.1 and 4.1 to 4.3). This is, in fact, situational, with large variations regarding the relative contribution of temperature and salinity to impedance, making it practically impossible to differentiate between the two when impedance gradients are the dominant source of backscatter (Ruddick et al., 2009; Sallarès et al., 2009). We have established that this is not the case, with backscatter actually dominated by plankton concentrations. The height at which these occur is not determined by impedance or sound speed but by density, which we established to be mainly governed by temperature near the surface and both temperature and salinity near the bed. The surface layer is generally well-mixed, which may be one of the reasons that plankton does not accumulate on the upper thermocline but remains entrained, while the bottom layer is expected to be subjected to less turbulent mixing, which is dampened by the thermocline, therefore allowing suspended matter to stably accumulate on the pycnocline. It makes sense that the damping of turbulence requires a stronger density gradient, provided by halocline. Therefore, we conclude that in Lake Veere, a backscatter gradient will generally constitute a thermocline, while a backscatter maximum is a stronger pycnocline, often associated with salinity, thus, a halocline. This also depends on the place in the water column, with saltwater generally accumulating near the bottom and the heat input mainly confined to the epilimnion.

## 5.2. Internal processes in a former estuary

We have analyzed the spatial and temporal behaviour of stratification, the behaviour of two thermoclines and one halocline, and the velocities measured by the ADCP. In this section, we reflect on the results and our methods, first discussing the observed stratification and then internal processes.

### 5.2.1. Evolution of stratification

The summer of 2024 was relatively cold with no recorded instances of fish mortality, possibly marking this year as less representative when investigating the direct cause of hypoxia near the bottom and the role of thermal stratification. Temperature gradients were highest during the start of July and the start of August, with $TSI$s generally around $0.7\,^{\circ}$C/m. This decreased as a larger portion of the water column was heated throughout August, indicating that the thermocline height as determined from the moorings is probably most accurate during the start of August, which is important for comparison with the acoustic method. Indeed, both the mooring-derived and the acoustically derived thermocline heights appear least noisy and show the closest agreement during this time period (see Figures 4.10 and F.5). Even though no fish mortality events were recorded, oxygen depletion was recorded during the summer (E. van Zanten, personal communication, November 19, 2024; also see Figure 1.2). This reinforces the belief that while thermal stratification may not be the direct cause of hypoxia, it could be a catalyst.

Through CTD and TSO measurements, it was found that the stratification in the northwest part of Lake Veere is governed by temperature near the surface and by salinity near the bed. The layer near the bed eluded the moorings and ADCP3 but was recorded by ADCP6. The CTD casts and TSO measurements recorded a salinity increase near the bottom of approximately $0.5$ PSU. This can have the same effect on density as a temperature difference of $2\,^{\circ}$C (see Figure 2.1a). This lower layer, on which suspended material was hypothesized to accumulate, could therefore well be a halocline between brackish water in Lake Veere and saline water from the Eastern Scheldt, even though it would constitute a limited salinity difference of only $0.5$ PSU.

The temporal growth of the bottom layer points to the net import of salt water from the Eastern Scheldt over the summer, likely caused by the decreased drainage from surrounding polders and the increased surface evaporation. The reason for the increased height of this layer after the June 10 storm remains unclear. However, it was likely influenced by circulation induced by the storm. This circulation appears to have been strong enough to mix the thermally stratified portion of the water column while leaving the salinity stratification largely intact. Consequently, it may have triggered an additional influx of salt-water from the east to this location. This mechanism is discussed by (Kranenburg et al., 2023), where increased flow in the main channel can lead to the set-up of a pycnocline in underlying pits. This would have allowed the salt water to spill over the sill into the pit where ADCP6 was placed. This should be confirmed through the use of additional salinity sampling near the bed, either continuous or at a higher frequency. These should also be specifically co-located with the ADCP, allowing for a close estimate of the Richardson number to investigate the temporal stability of this layer. For now, the cause for its disappearance remains unclear, but we hypothesized a period of increased shear to erode the stratification or re-suspend the accumulated matter(see Figure 4.19).

As discussed in Section 2.4, we classify Lake Veere as a discontinuous warm polymictic lake. This is confirmed by the temperature measurements. Frequent summer overturns likely prevented a strong thermocline. We analyze two mixing events: June 10 and August 23. On June 10, strong northwestern flow velocities recorded by both ADCPs likely caused the overturning, followed by reversed flow velocities in the following days, at which point the backscatter already showed full mixing. Velocities recorded by ADCP6 show that the large flow velocities generated at the surface do not penetrate down to the bed, though. On August 23, the ADCPs recorded southeastern flow, opposite to the June event. ADCP3 saw dominant along-lake flow, while ADCP6 had near-equal along- and cross-lake contributions. This suggests mixing is driven by northwestern/southeastern winds, which should be validated by meteorological data.

### 5.2.2. Oscillations of the thermocline

Thermocline depth (i.e., epilimnion thickness) is influenced by solar radiation, long-wave radiation of atmosphere and surface waters, sensible heat exchange, and heat flux associated with evaporation and precipitation, while also being forced by wind (Boehrer and Schultze, 2008). Several of these likely

contribute to a daily oscillation (e.g., atmospheric heat exchange, evaporation, and solar radiation), while others require further study for periodicity (e.g., wind). Most tracked interfaces exhibit a daily oscillation, with mooring 3 showing the strongest signal. Notably, it is also observed in the bottom layer, despite this layer likely being unaffected by solar radiation or atmospheric heat exchange (Boehrer and Schultze, 2008; Prins et al., 2023).

The moorings show little coherence at a daily frequency, except on August 18–20, when we observed a $\pi$ rad phase lag (while in-phase behaviour would be expected). This lack of coherence is attributed to daily insolation not being strong enough to drive large oscillations consistently, with other processes such as daily wind or circulation patterns likely playing a role. Backscatter data indicates that winds typically strengthen by midday, potentially making them a more significant driver than solar forcing. Similarly, this may have also influenced ADCP data. Future research should validate the role and timing of wind through local wind data analysis.

The daily oscillation measured by the ADCPs could also be influenced by a daily migration of phytoplankton, which can move through the upper water column by controlling their buoyancy (Macdonald et al., 2014). The capacity for migration depends on the plankton type. If observed plankton is capable of actively migrating, the ADCP may have detected their movement rather than passive vertical shifts associated with the thermocline. This would explain a high coherence between the ADCPs (and zero phase lag) at the daily frequency, but this is only observed between August 12–14. This oscillation may have been forced by a daily migration, but it is unlikely since this migration should be present in the rest of the signal, too. Typically, phytoplankton ascends during the day and descend at night, mirroring the expected daily oscillation of the thermocline, which rises with daytime surface heating and sinks at night as atmospheric cooling occurs. Thus, if phytoplankton migration aligns with the strength of insolation, it could serve as a useful indicator of daily forcing. We did not observe it, however. The type of plankton and whether it can move across the thermocline should be subject to future studies.

Most signals showed a strong semi-diurnal oscillation between August 5–7 Figures 4.12 to 4.16. This coincided with a spring tide, which occurred between August 5–7 and 21–23 (Rijkswaterstaat, 2025). This contribution was not observed during the latter, though. The reason for this is unclear. A semi-diurnal oscillation is also observed in the along-lake velocities shown in Figure 4.20e (bottom layer; June-July), which also coincided with spring tide. The back-and-forth is relatively uniform over the entire water column, which strengthens the belief that it is a tide. Currents do not penetrate this interface, though, demonstrating a strong stratification. Here, we even observe a seemingly out-of-phase motion with the tide. We therefore hypothesized that the tide does influence the tilting within the pits, possibly in the same way that wind might generate tilt at the surface of a lake.

Based on the frequency analysis and velocity measurements, cross-lake seiching was found on August 6 and 7 between mooring 3 and the ADCPs. Interestingly, an increased period was observed between ADCP3 and mooring 3 compared to ADCP6 and mooring 3, even though ADCP3 and mooring 3 are closer together. We hypothesize two possible explanations. Firstly, the seiching process is complicated by bathymetry, and the seiche is attenuated as it oscillates over the lake, somehow experiencing an increased resistance between ADCP3 and mooring 3. Secondly, the event between ADCP6 and mooring 3 happened slightly earlier, leaving time for mixing in between these events. An erosion of stratification would have reduced the phase speed, possibly increasing the internal seiching period. Other instances of increased coherence were found for cross-lake oscillations, but these may have been spurious, or not related to internal seiching. Along-lake internal seiching was found on August 19 and 21 between mooring 1 and ADCP6 and mooring 1 and mooring 2. This had a period of around $6$ hours and followed a period of large along-lake velocities.

Our methods were unable to detect high-frequency internal waves due to wavelet power leakage from high-frequency noise to periods of up to several hours. This is an artefact of noise, in which unremoved outliers are represented by wavelets of a high frequency and a large magnitude. This is observed as elongated, vertical peaks in the wavelet spectrum. This wavelet power leaks into the lower frequencies, but is mainly contained below periods of $4$ hours and occasionally leaks into the $4$–$8$ hours band. To mitigate high-frequency wavelet leakage, we reduced noise by burst-averaging, applying a median filter, and band-passing to sharpen gradients and remove outliers, which in the end limited our analysis to periods over $1$ hour.

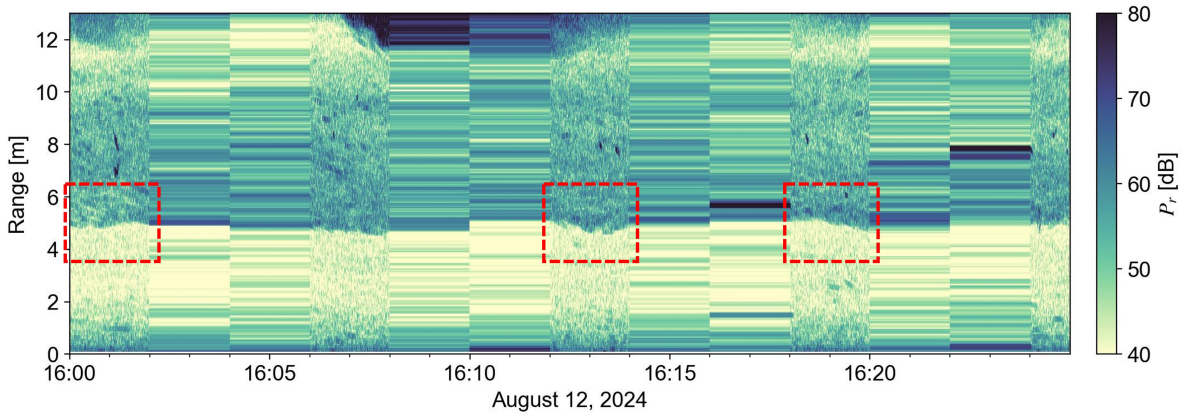


**Figure 5.3:** High-frequency internal wave passing ADCP3 on August 12, 2024. The highlighted areas represent high-frequency internal oscillations on the thermocline.

Our observations still indicate the presence of higher-frequency internal waves, as shown in Figure 5.3. Apparently, high-frequency oscillations of the thermocline are also well-represented in oscillations of the plankton. In this figure, a high-frequency internal wave passes by ADCP3 around 16:13h and has an amplitude of approximately $0.5$ meter. The $2$-minute measurement interval seems just short of fully capturing the wave period, in line with our estimations of the buoyancy frequency of $0.04$ rad/s ($157$ seconds). A more robust method of inferring the thermocline height that does not require averaging may be able to capture these oscillations.

Beyond wavelet power leakage from higher frequencies, outliers also complicated the statistical interpretation of frequency analysis. Wavelet and wavelet coherence transforms can incorporate significance testing through Monte Carlo methods and assumed red noise background spectra (Grinsted et al., 2004; Torrence and Compo, 1998). Low bias is crucial for this. However, in our case, significance testing primarily highlighted outliers, which often dominated thermocline heights at transitions between scattering mechanisms (i.e., storm-injected bubbles, secondary layers). Therefore, we omitted it from our analysis and instead validated the observed oscillations using the measured echograms and velocities. In the future, more robust algorithms are expected to improve statistical interpretation and enhance the reliability of frequency analysis.

# 6
# Conclusions

In this chapter, we present conclusions in line with the research questions outlined in Chapter 1.

1. Which thermocline dynamics are expected in Lake Veere?

Seasonal thermoclines in stratified lakes are influenced primarily by heat input and wind, which together control their sharpness and depth. Wind forcing, in particular, plays a crucial role in internal dynamics by tilting the thermocline, leading to internal seiching once the wind subsides or changes direction. In extreme cases, strong winds can induce upwelling and complete overturn, mixing the water column—a process often characterized using the Wedderburn and Lake numbers. Beyond large-scale tilting and seiching, wind forcing generates high-frequency internal waves (with the buoyancy frequency as an upper limit) and inertial oscillations.

Lake Veere exhibits multiple stratification regimes, with thermal stratification dominating the upper water column in the northwest, while salinity-driven stratification plays a more significant role near the lakebed and towards the east. During summer, periodic overturning events occur, classifying Lake Veere as a discontinuous warm polymictic lake, where alternating periods of increased and reduced stratification are observed. Given the limited exchange with the sea, we expect thermal stratification to be the dominant process in the northwest of Lake Veere, especially during periods of extended stability. The estuarine bathymetry likely introduces complex circulation patterns that may be difficult to quantify without numerical modelling. The system appears relatively uniform in the cross-lake direction, suggesting that classical thermocline tilting and internal seiching may still occur. Similarly, tilting may occur along the tidal channel, representing a longer and more uniform lake section. Phase speed computations suggest that these thermocline dynamics are unlikely to be affected by Coriolis.

2. How have acoustic instruments historically been used to measure (thermal) stratification and what are the most important factors determining their effectiveness?

Thermal stratification has rarely been directly measured with acoustic instruments outside of the laboratory. This is because impedance gradients by (thermal) stratification are rarely the dominant scatterer, especially close to the surface and in the highly dynamic environments of estuaries (compared to the ocean). In the absence of other scattering mechanisms (e.g., at large depths in the Arctic Ocean), stratification has been measured as a dominant backscatter mechanism, but rarely in estuaries or lakes. In general, attributing backscatter to stratification relies on its relatively weak frequency dependence compared to other scatterers. However, backscatter by stratification is generally minimal compared to other mechanisms and difficult to distinguish from noise. It has been isolated and distinguished from other mechanisms through comprehensive studies measuring many different physical scatterers in combination with backscattering. Still, isolating backscatter by stratification remains a major challenge due to the many inherent assumptions in models that predict scattering by stratification interfaces (and other mechanisms), which are therefore difficult to validate. Furthermore, distinguishing weak scattering from background noise requires precise noise estimates, which are difficult to obtain from an up-looking ADCP. Finally, scatterers (e.g., plankton) often aggregate around density interfaces, obscuring the detection of backscatter from stratification, but presenting a potential solution for tracking the interfaces when backscatter from such interfaces is weak.

Backscatter is commonly attributed to specific scatterers by analyzing spectral slopes—the variation of backscatter with frequency—which differ based on scatterer size, density, and abundance in the water column. Accurate backscatter measurements and spectral slope computations require echosounder calibration and independent measurements of scatterers to establish site-specific spectral slopes for

each contributing mechanism. Traditionally, spectral slopes have been determined using multiple narrowband frequencies. However, the recent surge in broadband echosounding applications has enabled spectral slope estimation from a single signal, although multiple frequency bands may still be preferred due to their coverage of a larger bandwidth. Broadband echosounding has improved spatial resolution at the cost of increased complexity and a higher risk of sidelobe interference and has seen multiple instances of successfully measuring stratification. Despite these successes, past studies have, in most cases, only succeeded in actually distinguishing scatterers using bandwidths of several hundred kHz, even though the individual signals within this range may be broadband. This demonstrates the need for echosounding at multiple frequencies or multiple ranges for both narrow- and broadband applications, respectively.

3. To what extent can thermal stratification be observed through acoustic backscatter and velocity measurements in Lake Veere?

Over the summer of 2024, we measured acoustic backscatter at narrowband frequencies $250$, $500$, and $1000$ kHz using the new multi-frequency mode of the Nortek Signature1000 ADCP in Lake Veere. While previous research successfully used the same device (and multi-frequency mode) to measure sediment in the Wadden Sea at these frequencies, we found that the $250$ and $500$ kHz channels detected too few scatterers in the lake, therefore operating too close to the noise floor. Consequently, these channels only sporadically measured significant backscatter and, even then, provided little additional information beyond what the $1000$ kHz channel captured. Qualitatively, we used the $250$ and $500$ kHz channels to infer responsible backscatter mechanisms, facilitating the attribution of backscatter to bubbles during periods of increased backscatter just below the water surface and to phytoplankton in the upper water column during August.

Thermal stratification was strongest in early July and early August. In August, we observed backscatter gradients across the thermocline, the location of which was validated using temperature moorings. Rather than a backscatter maximum, we found a strong backscatter gradient at the thermocline, suggesting that temperature-induced acoustic impedance differences were not the dominant scattering mechanism. Instead, we hypothesize phytoplankton to be the responsible scatterer. While stratification is strongest at the onset of warming (when the bottom layer is still cold), the detectability of the backscatter gradient increases as the warm period progresses, presumably due to the rapid bloom of phytoplankton over warm periods. We found that plankton stays above the thermocline and that by tracking the strong gradient in plankton concentration, we could effectively track the thermocline location, but only during the extended warm period during August. On average, this thermocline location corresponded well with the maximum temperature gradient derived from temperature moorings.

In addition to thermal stratification (i.e., a gradient in plankton concentration), we recorded a second interface with ADCP6 in one of the pits. Unlike the thermocline, this appeared as a local backscatter maximum rather than a strong backscatter gradient. We hypothesize that this interface is a halocline and that the responsible scatterer is an accumulation of sediment on this halocline. This layer, observed throughout June and July, suppressed flow velocities, prohibiting them from penetrating to the bottom, reinforcing that this interface constitutes a strong density gradient. It disappeared from acoustic backscatter at the onset of August, coinciding with increased velocity shear around this layer. Despite its disappearance from the acoustic backscatter, increased flow velocities at the surface still exhibited difficulty penetrating to the bottom, suggesting the continued presence of stratification. Whether this was due to the thermocline or remaining halocline remains unclear. If the latter, we attribute its disappearance from acoustic backscatter to the re-entrainment of suspended matter caused by the increased shear, which was (in that case) strong enough to resuspend sediment but insufficient to fully erode the stratification.

Tracking interfaces from acoustic backscatter was occasionally complicated by noise, leading to outliers and abrupt jumps in our estimates. Some of these outliers persisted for durations comparable to our averaging periods (i.e., fish), while others lasted for several hours (i.e., persisting secondary layers, bubble intrusions). This occurred because our algorithm identified global (gradient) maxima, meaning that if a sharper secondary layer temporarily emerged, it could override the original layer for extended periods. These secondary layers were likely transition zones where dominant scattering mechanisms shifted, such as bubble intrusions or sharp plankton gradients not indicative of the thermocline. Since our method divided the water column into two distinct layers by tracking only one layer, simultaneous

occurrences of multiple interfaces introduced abrupt changes in the detected thermocline depth.

> 4. Which internal oscillations are observed in Lake Veere (and how do these compare across the measurements by the ADCPs and the temperature moorings)?

Most thermocline height time series occasionally exhibited a daily component, most notably at the third mooring. However, coherence at this frequency was rare, especially at zero phase lag, suggesting it was unlikely driven by daily heat input and more likely influenced by a daily wind component. Heat forcing is instead expected in lower-frequency oscillations with periods $> 1$ day, which more consistently show coherence and zero-phase lag.

We identified cross-lake internal seiching of the thermocline on August 6–7, 12–13, and 21, 2024, using complex wavelet coherence (i.e., coherence magnitude and phase) between thermocline height time series from opposing sides of Lake Veere (ADCP3–mooring 3, ADCP6–mooring 3). Velocity measurements confirmed this, showing out-of-phase velocities above and below the thermocline. The cross-lake seiching period was approximately $4$ hours, often preceded by longer-period tilting, with tilting amplitudes reaching several meters and seiching amplitudes around one meter.

We identified along-lake seiching on August 9–11, 16–17, and 19–21, through thermocline height time series along the lake (mooring 1, mooring 2, ADCP3, ADCP6) with periods of $6$ hours. Overall, along-lake currents were not dominated by predicted seiching modes but appeared as background motion, often only observable after band-passing. When out-of-phase velocities above and below the thermocline dominated, they were typically of a lower frequency and thus more likely associated with tilting than seiching.

The halocline, present in acoustic measurements through June and July, sporadically exhibited a daily component—unexpected given its depth. This may result from the daily migration of plankton, the presumed scatterer accumulating at this layer or a daily wind component. A semi-diurnal oscillation appeared throughout the record, likely influenced by the tidal cycle, with greater presence around spring tide. Velocity measurements suggest that the flow, which does not penetrate the halocline, induces a set-down rather than a set-up.

Noise in the inferred thermoclines from both mooring and acoustic data complicated the interpretation of continuous wavelet analysis. While the wavelet transform proved valuable for its time-frequency resolution, required averaging and high-frequency noise restricted resolvable frequencies to periods $\gtrsim 2$ hours. Given these challenges, we manually investigated the presence of high-frequency internal waves, highlighting one example that suggests they may still be trackable via plankton concentration gradients if the thermocline inference methods were more robust.

We hypothesize that the discussed secondary layers, formed by transitions in dominant scattering mechanisms (e.g., bubble intrusions), interfere with tracking the primary thermocline and obscure higher frequencies in the wavelet analysis. These transitions may occur simultaneously across, for example, due to wind forcing that is uniform across the lake. This induces simultaneous noise spikes and/or signal jumps that artificially inflate coherence. The duration of these secondary layers is situational, complicating the distinction with internal seiching in wavelet spectra if we do not validate it with velocity data.

Finally, we address our main research question:

> To what extent can thermal stratification and corresponding internal oscillations be measured with acoustic instruments in low-dynamic former estuaries?

Acoustic observation of stratification is well-established through various indicators. In estuaries, this is often a difference in suspended sediment between river outflow and seawater inflow. Former estuaries are more similar to lakes and rely on the scattering through other mechanisms that often dominate over the impedance gradients by stratification that can be directly observed in the ocean, for instance, phytoplankton (which we assume is the scatterer we detect in our present analysis). The sensitivity to the periodic dominion of other scatterers (besides the one that purposely is tracked) makes thermal stratification hard to observe automatically through simple makeshift algorithms. Moreover, tracking thermocline height through phytoplankton requires extended periods of warm weather to allow for phytoplankton bloom. Under these conditions, we found that phytoplankton can serve as a reliable indicator

of thermocline height, allowing effective monitoring through acoustic backscatter.

We identified a halocline near the bottom of the lake, presumably due to the leakage of dense salt water from the Eastern Scheldt into Lake Veere. It was detected through a backscatter maximum rather than a gradient, which we attribute to the accumulation of suspended matter, facilitated by the dampening of velocity shear by the density gradient. It inhibited mixing and effectively closed off the bottom of one of the pits from the rest of the lake. We therefore expected it to contribute to the periodic hypoxia during the summer.

We successfully used continuous wavelet analysis to identify periods of internal seiching, which proved useful due to the non-stationarity of the signal. Wavelet coherence facilitated the identification of forcing processes by including phase information. However, this analysis was complicated by the noise in the thermocline height series, requiring validation with velocity data. This proved to be an essential step, ruling out spurious instances of observed oscillations while confirming others. A more robust tracking algorithm, which would introduce fewer periods of outliers or secondary layers and improve the thermocline height estimates, would reduce the need for this validation.

Finally, we were unable to consistently determine thermocline height through velocity shear. While surface velocities were often bounded by the thermocline depth, isolating specific frequency bands did not yield a reliable measure of thermocline height, especially at a high temporal resolution. This suggests that internal seiching was often not the dominant flow component. Nonetheless, long-term shear may serve as a useful indicator of the average thermocline height.

# 7
# Recommendations

In this chapter, we conclude this research with recommendations for future studies. The nature of this research was largely exploratory, with a focus on characterizing stratification and acoustic backscatter using the large amount of data gathered over the summer of 2024. In anticipation of a 2025 measurement campaign, we make recommendations regarding potential knowledge gaps identified through the present research and link this to recommendations for these campaigns. We structure these recommendations in line with our methods, first presenting recommendations for measurements, then for tracking thermocline height, and finally for inferring internal processes in the lake.

## 7.1. Acoustic measurements

We encountered practical difficulties using the $250$ and $500$ kHz channels due to the lack of scatterers associated with these frequencies in Lake Veere, decreasing the $SNR$ and thereby decreasing the reliability of measurements. We propose a dual mitigation method: 1) collecting accurate noise data and 2) optimizing the frequency of the acoustic pulses.

1. First, future campaigns should carefully measure system noise at each frequency in listening mode. Rather than using conservative noise estimates that artificially inflate the $SNR$, we can work closer to the noise floor and utilize more data. Measuring system noise could be achieved via a dedicated measurement mode running parallel to data collection or by suspending the ADCP from the vessel before/after the campaign. The former is more accurate but firmware-dependent, whereas the latter is simpler but susceptible to ship-induced noise and temporal variations in system noise during the deployment.
2. Secondly, to optimize pulse frequency, identifying site-specific dominant scatterers is crucial. In low-dynamic former estuaries, large suspended particles are less common than in more dynamic systems, resulting in reduced backscatter from lower-frequency signals—except near the bed, where sediment accumulates, or at the surface at the water-air interface. When tracking thermoclines (i.e., phytoplankton), higher frequencies are generally preferable but frequencies greater than $1000$ kHz are increasingly attenuated and are effective at smaller ranges, complicating measuring with inverted (uplooking) echosounders in deep former estuaries.

   Lower-frequency backscatter is expected to increase in areas with high concentrations of larger suspended material, such as estuaries and foreshores, or in the presence of biological scatterers like larger zooplankton and euphausiids in the open ocean (see Figure 1b in Lavery et al., 2007). However, while these may aggregate on pycnoclines (Haught et al., 2024; Lennert-Cody and Franks, 1999), they are not necessarily confined to the epilimnion like phytoplankton, which may limit the effectiveness of our thermocline detection method.

In summary, while using three narrowband frequencies allowed broad sampling capabilities, the lack of scatterers limited their effectiveness. In future campaigns, the optimal measurement frequency strongly depends on the scatterer and its relation to a pycnocline, with measurements in former estuaries likely benefiting from measurement frequencies $\geq 1000$ kHz and more dynamic sites from a lower bandwidth (i.e., $250$–$500$–$1000$ kHz). In former estuaries, future campaigns with this device would benefit from broadband measurements at $1000$ kHz for greater scatterer presence, improved resolution, and potential spectral slope derivation if calibrated. Additionally, including noise measurements will increase the amount of usable data.

We also consider using the fifth ADCP beam to measure velocities instead of acoustic backscatter. We

evaluate the following considerations: 1) the reduction of vertical resolution and 2) the requirements for measuring vertical velocities.

1. Measuring velocities instead of backscatter with the fifth beam reduces the range resolution from $0.048$ meter to $0.5$ meter, though backscatter data is still collected alongside velocities. This reduction limits the detection of small-amplitude oscillations but still allows monitoring of thermocline and bottom layer evolution. While future applications may benefit from integrating backscatter over larger volumes to decrease noise, this can also be done retrospectively.
2. Accurate vertical velocity measurements require precise horizontal alignment, as even small tilts introduce inaccuracies (i.e., $\gtrsim 10\,°$; Nortek Support, 2022). Bottom-mounted ADCPs were difficult to align perfectly, causing the spreading of shear and vertical velocity bias. While bin mapping mitigates shear effects, vertical velocity bias is unavoidable. Given the steep slopes in former estuaries, correct ADCP placement remains challenging, complicating highly accurate vertical velocity measurements.

Given the difficulty in mitigating misalignment, we recommend using the fifth beam for echosounding. Additionally, we recommend bin-mapping of velocities in future research to mitigate the spreading of shear.

## 7.2. Interface tracking

We hypothesized that acoustically tracked phytoplankton serves as a proxy for thermocline height. Strong agreement between plankton gradients and the thermocline suggests both long- and short-term trends are well represented. Whether this extends to other sites is up for debate, so, ideally, acoustic backscatter is supplemented by temperature data to validate the long-term coincidence of gradients in plankton concentrations and epilimnion height. The extension to other sites would also benefit from comprehensive plankton measurements (the last ones were by Wetsteyn, 2004a,b), ideally over an entire summer, to assess conditions for which this method has worked and to which sites it can be extended. Coincidentally, this would benefit the research on degrading water quality in Lake Veere, with decomposing organic material hypothesized to be the largest contributor to hypoxia.

Calibration was unnecessary for tracking interface depth estimation since we worked in logarithmic space, where calibration ($G_{\text{int}}$, see Equation (2.20)) is an added constant and does not influence gradients. However, in the presence of calibration, the robustness of interface tracking can be improved by quantifying the scattering mechanisms through spectral slopes (see Figure 5 in Warren et al., 2003). Spectral slopes facilitate the distinction between scattering by plankton and scattering by, for example, secondary layers, bubble intrusions, or fish and can therefore improve robustness by excluding backscatter associated with the wrong mechanisms. Whether to calibrate depends on whether scattering mechanisms (e.g., spectral slope, reflection coefficients) require quantification. Besides calibration, quantification often requires concurrent measurements to inform scattering models.

Beyond obtaining data on the tracked constituent, the tracking algorithm should be optimized for future applications. We recommend 1) a stronger black-box model, 2) creating a ground-truth dataset to inform interface-detection algorithms, and 3) tracking interfaces through visual scrutiny.

1. Recent developments in machine learning have enabled powerful edge detection algorithms. These are trained, validated, and tested with a labelled (i.e., ground-truth) dataset.
2. A ground-truth dataset for model training can be obtained by co-locating a temperature mooring and an echosounder. Co-location is crucial for the interface height to be accurately coupled to the thermocline. Still, directly estimating thermocline heights is prone to secondary layers and (temporary) erosion by increased surface shear.
3. Another option is tracking interfaces through visual scrutiny, which can be used to circumvent the need for make-shift tracking algorithms or to create a ground-truth dataset for model training. Manual tracking circumvents threshold arbitrariness, high acoustic noise, and difficulties distinguishing short-lived interfaces and secondary layers from the main thermocline. While prone to human errors, visual identification leverages backscatter strength (often through colour) and knowledge of expected thermocline heights and oscillations, aiding event recognition ahead of

frequency analysis. Noise can often be intuitively ignored, and thresholds loosened, increasing method applicability beyond periods of consistent layering.

## 7.3. Internal processes and forcing

The discussed improvements of interface tracking facilitate wavelet analysis; improving the robustness of tracking the thermocline height reduces the noise and thereby the leakage of wavelet power from high-frequencies into the spectra, improving observations of internal seiching (or higher-frequency oscillations) in the thermocline height signal. This requires a continuous time series with a higher temporal resolution than burst averages (every $6$ minutes). The highest frequency internal waves have periods of approximately $2$ minutes, so averaging every $1$ minute satisfies the Nyquist criteria while also smoothing the data, allowing frequency analysis to cover the full bandwidth of the internal wave spectrum if facilitated by a more robust tracking algorithm.

Identifying internal processes from wavelet spectra can be improved by narrowing the bandwidth by which we quantify internal processes. We used a broad bandwidth ($1$–$10$ hours) as an initial estimate of the seiching period. Future research should refine this bandwidth using numerical modelling, allowing localized frequency analysis for each instrument rather than applying a single broad bandwidth to all instruments. Additionally, numerical models would help analyze circulation patterns in former estuaries, which may be more complex than simple thermocline seiching (Kranenburg et al., 2023). We were unable to capture all dynamics, such as horizontal circulations or circulation cells during tilting. For future research, we recommend an event-based approach to quantify these circulations, possibly utilizing our globally focused analysis.

This study focused on internal process observations rather than their forcing mechanisms, leading to broad data collection but limited validation. Internal oscillations were validated through velocity data, but this provided limited insight into forcing mechanisms. Therefore, future studies should incorporate wind data to compute the Wedderburn and Lake numbers, facilitating event prediction and resolving whether observed signals represent thermocline tilting, bubble formation, or both.

# Bibliography


Antenucci, J. P. and Imberger, J. (2001). On internal waves near the high-frequency limit in an enclosed basin. *Journal of Geophysical Research: Oceans*, 106(C10):22465–22474.

Antenucci, J. P., Imberger, J., and Saggio, A. (2000). Seasonal evolution of the basin-scale internal wave field in a large stratified lake. *Limnology and Oceanography*, 45(7):1621–1638.

Assunção, R. V., Lebourges-Dhaussy, A., Da Silva, A. C., Bourlès, B., Vargas, G., Roudaut, G., and Bertrand, A. (2021). On the use of acoustic data to characterise the thermohaline stratification in a tropical ocean.

Bassett, C., Lavery, A. C., Ralston, D., Geyer, W. R., Jurisa, J. T., Thomson, J., Honegger, D. A., Simpson, A., Scully, M. E., and Haller, M. C. (2023). Acoustic backscattering at a tidal intrusion front. *Progress in Oceanography*, 219:103167.

Bassett, C. and Zeiden, K. (2023). Calibration and Processing of Nortek Signature1000 Echosounders. Technical Report APL-UW TR 2307, University of Washington, Seattle.

Battjes, J. A. and Labeur, R. J. (2017). *Unsteady Flow in Open Channels*. Cambridge University Press, Cambridge, United Kingdom ; New York, NY.

Bauer, S. W., Graf, W. H., Mortimer, C. H., and Perrinjaquet, C. (1981). Inertial motion in Lake Geneva (Le Léman). *Archives for meteorology, geophysics, and bioclimatology, Series A*, 30(3):289–312.

Black, K., Ibrahim, J., Helsby, R., McKay, J., Clark, T., Pearson, N., Moore, R., and Hernon, J. (2015). Turbulence: Best practices for measurement of turbulent flows. Technical Report MRCF-TiME-KS9a, Partrac Ltd, Ocean Array Systems Ltd, ABP Marine Environmental Research Ltd.

Boegman, L., Imberger, J., Ivey, G. N., and Antenucci, J. P. (2003). High-frequency internal waves in large stratified lakes. *Limnology and Oceanography*, 48(2):895–919.

Boegman, L., Ivey, G. N., and Imberger, J. (2005). The degeneration of internal waves in lakes with sloping topography. *Limnology and Oceanography*, 50(5):1620–1637.

Boehrer, B. and Schultze, M. (2008). Stratification of lakes. *Reviews of Geophysics*, 46(2).

Brenner, S., Thomson, J., Rainville, L., Torres, D., Doble, M., Wilkinson, J., and Lee, C. (2023). Acoustic Sensing of Ocean Mixed Layer Depth and Temperature from Uplooking ADCPs. *Journal of Atmospheric and Oceanic Technology*, 40(1):53–64.

Chaudhuri, D., Sengupta, D., D'Asaro, E., and Shivaprasad, S. (2021). Trapping of Wind Momentum in a Salinity-Stratified Ocean. *Journal of Geophysical Research: Oceans*, 126(12):e2021JC017770.

Chen, C.-T. A. and Millero, F. (1977). Speed of sound in seawater at high pressures. *Journal of The Acoustical Society of America*, 62(5):1129–1135.

Chen, C.-T. A. and Millero, F. J. (1986). Precise thermodynamic properties for natural waters covering only the limnological range. *Limnology and Oceanography*, 31(3):657–662.

Chu, P. C. and Fan, C. (2010). Optimal Linear Fitting for Objective Determination of Ocean Mixed Layer Depth from Glider Profiles. *Journal of Atmospheric and Oceanic Technology*, 27(11):1893–1898.

Craeymeersch, J. and De Vries, I. (2007). Waterkwaliteit en ecologie Veerse Meer: het tij is gekeerd. Technical report, Rijkswaterstaat Rijksinstituut voor Kust en Zee, Middelburg.

Csanady, G. T. (1967). Large-scale motion in the Great Lakes. *Journal of Geophysical Research (1896-1977)*, 72(16):4151–4162.

D'Asaro, E. A. (1985). The Energy Flux from the Wind to Near-Inertial Motions in the Surface Mixed Layer. *Journal of Physical Oceanography*, 15(8):1043–1059.

Daugharty, M. (2024). Theoretical Acoustic Sensitivity.

De Boyer Montégut, C., Madec, G., Fischer, A. S., Lazar, A., and Iudicone, D. (2004). Mixed layer depth over the global ocean: An examination of profile data and a profile-based climatology. *Journal of Geophysical Research: Oceans*, 109(C12).

De Carvalho Bueno, R., Bleninger, T., Boehrer, B., and Lorke, A. (2023). Physical mechanisms of internal seiche attenuation for non-ideal stratification and basin topography. *Environmental Fluid Mechanics*, 23(3):689–710.

Duda, T. F., Lavery, A. C., and Sellers, C. J. (2016). Evaluation of an acoustic remote sensing method for frontal-zone studies using double-diffusive instability microstructure data and density interface data from intrusions. *Methods in Oceanography*, 17:264–281.

Farge, M. (1992). Wavelet transforms and their applications to turbulence. *Annual Review of Fluid Mechanics*, 24(Volume 24, 1992):395–458.

Fisher, F. H. and Squier, E. D. (1975). Observation of acoustic layering and internal waves with a narrow-beam 87.5-kHz echo sounder. *The Journal of the Acoustical Society of America*, 58(6):1315–1317.

Flood, B., Wells, M., Dunlop, E., and Young, J. (2020). Internal waves pump waters in and out of a deep coastal embayment of a large lake. *Limnology and Oceanography*, 65(2):205–223.

Fofonoff, N. and Millard, R. (1983). Algorithms for Computation of Fundamental Properties of Seawater. Technical 44, UNESCO, Paris.

Foote, K. G. (2009). Acoustic Methods: Brief Review and Prospects for Advancing Fisheries Research. In Beamish, R. J. and Rothschild, B. J., editors, *The Future of Fisheries Science in North America*, pages 313–343. Springer Netherlands, Dordrecht.

Francois, R. E. and Garrison, G. R. (1982a). Sound absorption based on ocean measurements: Part I: Pure water and magnesium sulfate contributions. *The Journal of the Acoustical Society of America*, 72(3):896–907.

Francois, R. E. and Garrison, G. R. (1982b). Sound absorption based on ocean measurements. Part II: Boric acid contribution and equation for total absorption. *The Journal of the Acoustical Society of America*, 72(6):1879–1890.

Galperin, B., Sukoriansky, S., and Anderson, P. S. (2007). On the critical Richardson number in stably stratified turbulence. *Atmospheric Science Letters*, 8(3):65–69.

Gill, A. (1982). *Atmosphere-Ocean Dynamics*. Academic Press.

Goodman, L. (1990). Acoustic scattering from ocean microstructure. *Journal of Geophysical Research: Oceans*, 95(C7):11557–11573.

Gostiaux, L. and Van Haren, H. (2010). Extracting Meaningful Information from Uncalibrated Backscattered Echo Intensity Data. *Journal of Atmospheric and Oceanic Technology*, 27(5):943–949.

Greenwood, N., Parker, E. R., Fernand, L., Sivyer, D. B., Weston, K., Painting, S. J., Kröger, S., Forster, R. M., Lees, H. E., Mills, D. K., and Laane, R. W. P. M. (2010). Detection of low bottom water oxygen concentrations in the North Sea; implications for monitoring and assessment of ecosystem health. *Biogeosciences*, 7(4):1357–1373.

Grinsted, A., Moore, J. C., and Jevrejeva, S. (2004). Application of the cross wavelet transform and wavelet coherence to geophysical time series. *Nonlinear Processes in Geophysics*, 11(5/6):561–566.

Gro Vea Salvanes, A., Devine, J., Jensen, K. H., Hestetun, J. T., Sjøtun, K., and Glenner, H. (2018). *Marine Ecological Field Methods: A Guide for Marine Biologists and Fisheries Scientists*. John Wiley & Sons, Incorporated, Newark, United Kingdom.

Gupta, R. N. (1965). Reflection of plane waves from a linear transition layer in liquid media. *Geophysics*, 30(1):122–132.

Gupta, R. N. (1966). Reflection of Sound Waves from Transition Layers. *The Journal of the Acoustical Society of America*, 39(2):255–260.

Haught, D. R. W., Stumpner, P., Burau, J., Violette, T., and Conlen, A. (2024). Suspended particulate matter mixing in the Low Salinity Zone of the San Francisco Estuary, California. In *Bay-Delta Conference Proceedings*, Sacramento, California.

Haury, L. R., Briscoe, M. G., and Orr, M. H. (1979). Tidally generated internal wave packets in Massachusetts Bay. *Nature*, 278(5702):312–317.

Hodges, B. R., Imberger, J., Saggio, A., and Winters, K. B. (2000). Modeling basin-scale internal waves in a stratified lake. *Limnology and Oceanography*, 45(7):1603–1620.

Holland, A. M. B. M., Berrevoets, C. M., Consemulder, J., Peperzak, P. L., Stikvoort, E. C., Twisk, F., Wetsteyn, L. P. M. J., and Wolfstein, K. (2004). Toestand ecosysteem Veerse Meer vóór ingebruikname doorlaatmiddel. Technical report, Rijksinstituut voor Kust en Zee, Middelburg.

Howard, L. N. (1961). Note on a paper of John W. Miles. *Journal of Fluid Mechanics*, 10(04).

Imberger, J. and Patterson, J. C. (1989). Physical Limnology. In *Advances in Applied Mechanics*, volume 27, pages 303–475. Elsevier.

Jaarsma, R. A. J. (2023). *Quantifying Suspended Sediment Using Multi-Frequency Echosounder Measurements*. MSc, Delft University of Technology, Delft.

Joosten, L. (2021). Landschapsanalyse van het Veerse Meer. Technical report, Provincie Zeeland, Middelburg.

Jung, N. W., Lee, G.-h., Dellapenna, T. M., Jung, Y., Jo, T.-C., Chang, J., and Figueroa, S. M. (2024). Economic Development Drives Massive Global Estuarine Loss in the Anthropocene. *Earth's Future*, 12(4):e2023EF003691.

Kirillin, G. and Shatwell, T. (2016). Generalized scaling of seasonal thermal stratification in lakes. *Earth-Science Reviews*, 161:179–190.

Klink, J. (1999). DYNMODES. Woods Hole (MA): Woods Hole Science Center.

Kranenburg, C., Pietrzak, J. D., and Abraham, G. (1991). Trapped internal waves over undular topography. *Journal of Fluid Mechanics*, 226:205–217.

Kranenburg, W. M. (2023). StratiFEst: Verslag 2023. Technical report, TU Delft, Delft.

Kranenburg, W. M., Tiessen, M., Veenstra, J., De Graaff, R., Uittenbogaard, R., Bouffard, D., Sakindi, G., Umutoni, A., Van De Walle, J., Thiery, W., and Van Lipzig, N. (2020). 3D-modelling of Lake Kivu: Horizontal and vertical flow and temperature structure under spatially variable atmospheric forcing. *Journal of Great Lakes Research*, 46(4):947–960.

Kranenburg, W. M., Tiessen, M. C., Blaas, M., and Van Veen, N. P. (2023). Circulation, stratification and salt dispersion in a former estuary after reintroducing seawater inflow. *Estuarine, Coastal and Shelf Science*, 282:108221.

Krieger, S. and Freij, N. (2023). PyCWT: Spectral analysis using wavelets in Python.

Lavery, A., Chu, D., and Moum, J. (2010). Observations of broadband acoustic backscattering from nonlinear internal waves: Assessing the contribution from microstructure. *IEEE Journal of Oceanic Engineering*, 35(4):695–709.

Lavery, A. C., Bassett, C., Lawson, G. L., and Jech, J. M. (2017). Exploiting signal processing approaches for broadband echosounders. *ICES Journal of Marine Science*, 74(8):2262–2275.

Lavery, A. C., Geyer, W. R., and Scully, M. E. (2013). Broadband acoustic quantification of stratified turbulence. *The Journal of the Acoustical Society of America*, 134(1):40–54.

Lavery, A. C. and Ross, T. (2007). Acoustic scattering from double-diffusive microstructure. *The Journal of the Acoustical Society of America*, 122(3):1449–1462.

Lavery, A. C., Wiebe, P. H., Stanton, T. K., Lawson, G. L., Benfield, M. C., and Copley, N. (2007). Determining dominant scatterers of sound in mixed zooplankton populations. *The Journal of the Acoustical Society of America*, 122(6):3304–3326.

LaZerte, B. D. (1980). The dominating higher order vertical modes of theinternal seiche in a small lake. *Limnology and Oceanography*, 25(5):846–854.

Lennert-Cody, CE. and Franks, P. (1999). Plankton patchiness in high-frequency internal waves. *Marine Ecology-progress Series - MAR ECOL-PROGR SER*, 186:59–66.

Lewandowska, A. M., Breithaupt, P., Hillebrand, H., Hoppe, H.-G., Jürgens, K., and Sommer, U. (2012). Responses of primary productivity to increased temperature and phytoplankton diversity. *Journal of Sea Research*, 72:87–93.

Lewis, Jr., W. M. (1983). A Revised Classification of Lakes Based on Mixing. *Canadian Journal of Fisheries and Aquatic Sciences*, 40(10):1779–1787.

Li, Q., Farmer, D. M., Duda, T. F., and Ramp, S. (2009). Acoustical Measurement of Nonlinear Internal Waves Using the Inverted Echo Sounder. *Journal of Atmospheric and Oceanic Technology*, 26(10):2228–2242.

Macdonald, R., Bowers, D., McKee, D., Graham, G., and Nimmo-Smith, W. (2014). Vertical migration maintains phytoplankton position in a tidal channel with residual flow. *Marine Ecology Progress Series*, 509:113–126.

Maclennan, D., Fernandes, P., Dalen, J., and Fernandes, D. (2002). A consistent approach to definitions and symbols in fisheries acoustics. *ICES Journal of Marine Science*, 59:365–369.

Macrander, A., Käse, R. H., Send, U., Valdimarsson, H., and Jónsson, S. (2007). Spatial and temporal structure of the Denmark Strait Overflow revealed by acoustic observations. *Ocean Dynamics*, 57(2):75–89.

McManus, M. A., Alldredge, A. L., Barnard, A. H., Boss, E., Case, J. F., Cowles, T. J., Donaghay, P. L., Eisner, L. B., Gifford, D. J., F.Greenlaw, C., Herren, C. M., Holliday, D. V., Johnson, D., MacIntyre, S., McGehee, D. M., Osborn, T. R., Perry, M. J., Pieper, R. E., B.Rines, J. E., Smith, D. C., Sullivan, J. M., Talbot, M. K., Twardowski, M. S., Weidemann, A., and Zaneveld, J. R. (2003). Characteristics, distribution and persistence of thin layers over a 48 hour period. *Marine Ecology Progress Series*, 261:1–19.

McManus, M. A., Cheriton, O. M., Drake, P. T., Holliday, D. V., Storlazzi, C. D., Donaghay, P. L., and Greenlaw, C. F. (2005). Effects of physical processes on structure and transport of thin zooplankton layers in the coastal ocean. *Marine Ecology Progress Series*, 301:199–215.

Medwin, H. and Clay, C. S. (1998). *Fundamentals of Acoustical Oceanography*. Applications of Modern Acoustics. Academic Press, Boston.

Meyers, S. D., Kelly, B. G., and O'Brien, J. J. (1993). An Introduction to Wavelet Analysis in Oceanography and Meteorology: With Application to the Dispersion of Yanai Waves. *Monthly Weather Review*, 121(10):2858–2866.

Miles, J. W. (1961). On the stability of heterogeneous shear flows. *Journal of Fluid Mechanics*, 10(4):496–508.

Mohammadloo, T. H., Snellen, M., Renoud, W., Beaudoin, J., and Simons, D. G. (2019). Correcting Multibeam Echosounder Bathymetric Measurements for Errors Induced by Inaccurate Water Column Sound Speeds. *IEEE Access*, 7:122052–122068.

Mohammadloo, T. H., Snellen, M., and Simons, D. G. (2020). Assessing the Performance of the Multi-Beam Echo-Sounder Bathymetric Uncertainty Prediction Model. *Applied Sciences*, 10(13):4671.

Mortimer, C. H., Longuet-Higgins, M. S., and Pearsall, W. H. (1952). Water movements in lakes during summer stratification; evidence from the distribution of temperature in Windermere. *Philosophical Transactions of the Royal Society of London. Series B, Biological Sciences*, 236(635):355–398.

Munk, W. H. and Garrett, C. J. R. (1973). Internal wave breaking and microstructure (The chicken and the egg). *Boundary-Layer Meteorology*, 4(1):37–45.

Nortek Support (2022). *Principles of Operation*. Norway.

Nortek Support (2024a). How is a coordinate transformation done? https://support.nortekgroup.com/hc/en-us/articles/360029820971-How-is-a-coordinate-transformation-done.

Nortek Support (2024b). What is sidelobe interference? Why does it occur? https://support.nortekgroup.com/hc/en-us/articles/360029830091-What-is-sidelobe-interference-Why-does-it-occur.

Nortek Support (2025). How do I find the equivalent two-way beam angle $\Psi$ for my echo sounder? https://support.nortekgroup.com/hc/en-us/articles/360021299299-How-do-I-find-the-equivalent-two-way-beam-angle-%CE%A8-for-my-echo-sounder.

Ou, H. W. and Bennett, J. R. (1979). A Theory of the Mean Flow Driven by Long Internal Waves in a Rotating Basin, with Application to Lake Kinneret. *Journal of Physical Oceanography*, 9(6):1112–1125.

Patterson, B. D., MacRae, E. A., and Ferguson, I. B. (1984). Estimation of hydrogen peroxide in plant extracts using titanium(IV). *Analytical Biochemistry*, 139(2):487–492.

Penrose, J. D. and Beer, T. (1981). Acoustic reflection from estuarine pycnoclines. *Estuarine, Coastal and Shelf Science*, 12(3):237–249.

Pietrzak, J. D., Kranenburg, C., Abraham, G., Kranenborg, B., and Van der Wekken, A. (1991). Internal Wave Activity in Rotterdam Waterway. *Journal of Hydraulic Engineering*, 117(6):738–757.

Pollard, R. T. and Millard, R. C. (1970). Comparison between observed and simulated wind-generated inertial oscillations. *Deep Sea Research and Oceanographic Abstracts*, 17(4):813–821.

Pomar, L., Morsilli, M., Hallock, P., and Bádenas, B. (2012). Internal waves, an under-explored source of turbulence events in the sedimentary record. *Earth-Science Reviews*, 111(1):56–81.

Prins, T., Nolte, A., Buckman, L., and Stolte, W. (2023). Systeemanalyse Veerse Meer. Technical Report 11208079-000, Deltares, Delft.

Prins, T., Nolte, A., Rodriguez, S. C., Van der Heijden, L., and Buckman, L. (2024). Het ecologisch functioneren van het Veerse Meer 2005-2023. Technical Report 11209251-000, Deltares, Delft.

Prins, T., Vergouwen, S. A., Nolte, A. J., and Schipper, C. A. (2015). Bekkenrapport Veerse Meer 2000-2014. Technical Report 1220248-000, Deltares, Delft.

Rijkswaterstaat (2024). Lucht. https://waterinfo.rws.nl/thema/Waterbeheer.

Rijkswaterstaat (2025). Getij. https://www.rijkswaterstaat.nl/water/waterdata-en-waterberichtgeving/waterdata/getij.

Robertis, A. and Higginbottom, I. (2007). A post-processing technique to estimate signal-to-noise ratio and remove echosounder background noise. *ICES. J. Mar. Sci*, 64.

Ross, T. and Lavery, A. (2010). Acoustic Detection of Oceanic Double-Diffusive Convection: A Feasibility Study. *Journal of Atmospheric and Oceanic Technology*, 27(3):580–593.

Ross, T. and Lavery, A. C. (2011). Acoustic scattering from density and sound speed gradients: Modeling of oceanic pycnoclines. *The Journal of the Acoustical Society of America*, 131(1):EL54–EL60.

Rossby, T. (1969). On monitoring depth variations of the main thermocline acoustically. *Journal of Geophysical Research*, 74(23):5542–5546.

Ruddick, B., Song, H., Dong, C., and Pinheiro, L. (2009). Water Column Seismic Images as Maps of Temperature Gradient. *Oceanography*, 22:192–205.

Saggio, A. and Imberger, J. (1998). Internal wave weather in a stratified lake. *Limnology and Oceanography*, 43(8):1780–1795.

Saggio, A. and Imberger, J. (2001). Mixing and turbulent fluxes in the metalimnion of a stratified lake. *Limnology and Oceanography*, 46(2):392–409.

Sallarès, V., Biescas, B., Buffett, G., Carbonell, R., Dañobeitia, J. J., and Pelegrí, J. L. (2009). Relative contribution of temperature and salinity to ocean acoustic reflectivity. *Geophysical Research Letters*, 36(24).

Shibley, N. C., Timmermans, M.-L., and Stranne, C. (2020). Analysis of Acoustic Observations of Double-Diffusive Finestructure in the Arctic Ocean. *Geophysical Research Letters*, 47(18):e2020GL089845.

Simpson, J., Woolway, R., Scannell, B., Austin, M., Powell, B., and Maberly, S. (2021). The Annual Cycle of Energy Input, Modal Excitation and Physical Plus Biogenic Turbulent Dissipation in a Temperate Lake. *Water Resources Research*, 57.

Simpson, J. H., Wiles, P. J., and Lincoln, B. J. (2011). Internal seiche modes and bottom boundary-layer dissipation in a temperate lake from acoustic measurements. *Limnology and Oceanography*, 56(5):1893–1906.

Sommer, T., Carpenter, J., Schmid, M., Lueck, R., Schurter, M., and Wüest, A. (2013). Interface structure and flux laws in a natural double-diffusive layering. *Journal of Geophysical Research: Oceans*, 118(11):6092–6106.

Stanton, T. K., Wiebe, P. H., Chu, D., and Goodman, L. (1994). Acoustic characterization and discrimination of marine zooplankton and turbulence. *ICES Journal of Marine Science*, 51(4):469–479.

Stevens, C. and Imberger, J. (1996). The initial response of a stratified lake to a surface shear stress. *Journal of Fluid Mechanics*, 312:39–66.

Stranne, C., Mayer, L., Weber, T. C., Ruddick, B. R., Jakobsson, M., Jerram, K., Weidner, E., Nilsson, J., and Gårdfeldt, K. (2017). Acoustic Mapping of Thermohaline Staircases in the Arctic Ocean. *Scientific Reports*, 7(1):15192.

Thompson, R. and Imberger, J. (1980). Response of a numerical model of a stratified lake to wind stress. *Second International Symposium on Stratified Flows*, 1:562–570.

Thomson, R. E. and Emery, W. J. (2024). Chapter 5 - Time Series Analysis Methods. In *Data Analysis Methods in Physical Oceanography (Fourth Edition)*, pages 515–669. Elsevier Science, 4 edition.

Thorpe, S. A. (1973). Turbulence in stably stratified fluids: A review of laboratory experiments. *Boundary-Layer Meteorology*, 5(1):95–119.

Ton, A., Lee, M., Vos, S., Gawehn, M., den Heijer, K., and Aarninkhof, S. (2020). 27 - Beach and nearshore monitoring techniques. In Jackson, D. W. T. and Short, A. D., editors, *Sandy Beach Morphodynamics*, pages 659–687. Elsevier.

Torrence, C. and Compo, G. P. (1998). A Practical Guide to Wavelet Analysis. *Bulletin of the American Meteorological Society*, 79(1):61–78.

Valipour, R., Bouffard, D., Boegman, L., and Rao, Y. R. (2015). Near-inertial waves in Lake Erie. *Limnology and Oceanography*, 60(5):1522–1535.

Van der Kaaij, T. and Kerkhoven, D. (2021). Ontwikkeling zesde-generatie modelschematisatie 3D D-HYDRO Veerse Meer. Technical Report 11206814-000, Deltares, Delft.

Van Rijsen, J., Van Keeken, O., and Leeuw, J. (2022). Vismonitoring Rijkswateren t/m 2021. Deel I, Toestand en trends. Technical Report C085/22, Wageningen Marine Research, IJmuiden.

Velasco, D. W., Nylund, S., and Pettersen, T. (2018). Combined Current Profiling and Biological Echosounding Results from a Single ADCP. In *2018 OCEANS - MTS/IEEE Kobe Techno-Oceans (OTO)*, pages 1–5.

Warren, J. D., Stanton, T. K., Wiebe, P. H., and Seim, H. E. (2003). Inference of biological and physical parameters in an internal wave using multiple-frequency, acoustic-scattering data. *ICES Journal of Marine Science*, 60(5):1033–1046.

Watson, E. R. (1904). Movements of the Waters of Loch Ness, as Indicated by Temperature Observations. *The Geographical Journal*, 24(4):430–437.

Weidner, E., Stranne, C., Sundberg, J. H., Weber, T. C., Mayer, L., and Jakobsson, M. (2020). Tracking the spatiotemporal variability of the oxic–anoxic interface in the Baltic Sea with broadband acoustics. *ICES Journal of Marine Science*, 77(7-8):2814–2824.

Weidner, E. and Weber, T. C. (2021). An acoustic scattering model for stratification interfaces. *The Journal of the Acoustical Society of America*, 150(6):4353–4361.

Wetsteyn, B. (2004a). Fytoplankton Veerse Meer. Technical Report RIKZ/OS/2004.816x, Rijksinstituut voor Kust en Zee, Middelburg.

Wetsteyn, B. (2004b). Zoöplankton Veerse Meer. Technical Report RIKZ/OS/2004.817x, Rijksinstituut voor Kust en Zee, Middelburg.

Wüest, A. and Lorke, A. (2003). Small-scale hydrodynamics in lakes. *Annual Review of Fluid Mechanics*, 35(1):373–412.

Xu, W., Collingsworth, P. D., and Minsker, B. (2019). Algorithmic Characterization of Lake Stratification and Deep Chlorophyll Layers From Depth Profiling Water Quality Data. *Water Resources Research*, 55(5):3815–3834.

Yang, X., Li, Y., Wang, B., Xiao, J., Yang, M., and Liu, C.-Q. (2020). Effect of hydraulic load on thermal stratification in karst cascade hydropower reservoirs, Southwest China. *Journal of Hydrology: Regional Studies*, 32:100748.

Yu, H., Tsuno, H., Hidaka, T., and Jiao, C. (2010). Chemical and thermal stratification in lakes. *Limnology*, 11(3):251–257.

# A
# Water quantities

## A.1. Density

The density of water (Fofonoff and Millard, 1983) is given by

$$\rho = \rho(S, T_{\text{pot}}) = \sum_{i=0}^{5} a_i T_{\text{pot}}^i + S \sum_{i=0}^{4} b_i T_{\text{pot}}^i + S^{3/2} \sum_{i=0}^{2} c_i T_{\text{pot}}^i + S^2 d_0, \tag{A.1}$$

where

$$\begin{aligned} a_i &= [999.842594;\ 6.793952 \times 10^{-2};\ -9.095290 \times 10^{-3};\\ &\quad -1.001685 \times 10^{-4};\ -1.120083 \times 10^{-6};\ 6.536332 \times 10^{-9}],\\ b_i &= [0.824493;\ -4.0899 \times 10^{-3};\ 7.6438 \times 10^{-5};\ -8.2467 \times 10^{-7};\ 5.3875 \times 10^{-9}],\\ c_i &= [-5.72466 \times 10^{-3};\ 1.0227 \times 10^{-4};\ -1.6546 \times 10^{-6}],\\ d_0 &= 4.8314 \times 10^{-4}. \end{aligned} \tag{A.2}$$

Here, $a$, $b$, $c$, and $d$ are coefficients, $S$ denotes oceanic salinity in PSU, and $T_{\text{pot}}$ denotes the potential temperature in °C.

## A.2. Speed of sound

The speed of sound in seawater (Chen and Millero, 1977) is given by

$$c_s(T, S, p) = C_w(T, p) + A(T, p)S + B(T, p)S^{3/2} + D(T, p)S^2, \tag{A.3}$$

where

$$\begin{aligned} C_w(T, p) &= \sum_{i=0}^{3} \sum_{j=0}^{5} C_{ij} T^j p^i,\\ A(T, p) &= \sum_{i=0}^{3} \sum_{j=0}^{4} A_{ij} T^j p^i,\\ B(T, p) &= \sum_{i=0}^{1} \sum_{j=0}^{1} B_{ij} T^j p^i,\\ D(T, p) &= \sum_{i=0}^{1} D_i p^i. \end{aligned}$$

The coefficients are

$$C_{ij} = \begin{bmatrix} 1402.388 & 5.03711 & -5.80852 \times 10^{-2} & 3.3420 \times 10^{-4} & -1.47800 \times 10^{-6} & 3.1464 \times 10^{-9} \\ 0.153563 & 6.8982 \times 10^{-4} & -8.1788 \times 10^{-6} & 1.3621 \times 10^{-7} & -6.1185 \times 10^{-10} & 0 \\ 3.1260 \times 10^{-5} & -1.7107 \times 10^{-6} & 2.5974 \times 10^{-8} & -2.5335 \times 10^{-10} & 1.0405 \times 10^{-12} & 0 \\ -9.7729 \times 10^{-9} & 3.8504 \times 10^{-10} & -2.3643 \times 10^{-12} & 0 & 0 & 0 \end{bmatrix},$$

$$A_{ij} = \begin{bmatrix} 1.389 & -1.262 \times 10^{-2} & 7.164 \times 10^{-5} & 2.006 \times 10^{-6} & -3.21 \times 10^{-8} \\ 9.4742 \times 10^{-5} & -1.2580 \times 10^{-5} & 6.4885 \times 10^{-8} & 1.0507 \times 10^{-8} & -2.0122 \times 10^{-10} \\ -3.9064 \times 10^{-7} & 9.1041 \times 10^{-9} & -1.6002 \times 10^{-10} & 7.988 \times 10^{-12} & 0 \\ 1.100 \times 10^{-10} & -6.649 \times 10^{-12} & -3.389 \times 10^{-13} & 0 & 0 \end{bmatrix},$$

$$B_{ij} = \begin{bmatrix} -1.922 \times 10^{-2} & -4.42 \times 10^{-5} \\ 7.3637 \times 10^{-5} & 1.7945 \times 10^{-7} \end{bmatrix},$$

$$D_i = \begin{bmatrix} 1.727 \times 10^{-3} & -7.9836 \times 10^{-6} \end{bmatrix}.$$

Here, $c_s$ [m/s] is the sound speed in seawater, $T$ [°C] is the temperature, $S$ [PSU] is the salinity, $p$ [bar] is the pressure, and $C_{ij}$, $A_{ij}$, $B_{ij}$, and $D_i$ are the coefficients as provided in the original implementation.

Similarly, speed of sound in freshwater (Chen and Millero, 1986) is given by

$$c_s = \sum_{i=0}^{5} a_i T_{\text{pot}}^i + S \sum_{i=0}^{2} b_i T_{\text{pot}}^i + p \sum_{i=0}^{2} c_i T_{\text{pot}}^i - 5.58 \times 10^{-5} pS + 1.593 \times 10^{-5} p^2 \tag{A.4}$$

with

$$\begin{aligned} a_{\text{i}} &= [1402.388; 5.0371; -5.8085 \times 10^{-2}; 3.342 \times 10^{-4}; -1.478 \times 10^{-6}; 3.146 \times 10^{-9}], \\ b_{\text{i}} &= [1.322; -7.01 \times 10^{-3}; 4.9 \times 10^{-5}], \\ c_{\text{i}} &= [0.15564; 4.046 \times 10^{-4}; -8.15 \times 10^{-7}]. \end{aligned} \tag{A.5}$$

# A.3. Absorption

The absorption (Francois and Garrison, 1982a,b) is given by

$$\alpha = \frac{A_1 P_1 f_1 f^2}{f^2 + f_1^2} + \frac{A_2 P_2 f_2 f^2}{f^2 + f_2^2} + A_3 P_3 f^2, \tag{A.6}$$

where the contributions are defined as follows:

$$\begin{aligned} A_1 &= \frac{8.86}{c_s} \cdot 10^{0.78\,\text{pH}-5}, \\ f_1 &= 2.8\sqrt{\frac{S}{35}} \cdot 10^{4-\frac{1245}{T_{\text{kel}}}}, \\ P_1 &= 1. \end{aligned} \tag{A.7}$$

$$\begin{aligned} A_2 &= 21.44 \cdot \frac{S}{c_s} \cdot (1 + 0.025T), \\ f_2 &= \frac{8.17 \cdot 10^{8-\frac{1990}{T_{\text{kel}}}}}{1 + 0.0018 \cdot (S - 35)}, \\ P_2 &= 1 - 1.37 \cdot 10^{-4} D + 6.2 \cdot 10^{-9} D^2. \end{aligned} \tag{A.8}$$

$$\begin{aligned} A_3 &= \begin{cases} 4.937 \cdot 10^{-4} - 2.59 \cdot 10^{-5} T + 9.11 \cdot 10^{-7} T^2 - 1.50 \cdot 10^{-8} T^3, & \text{if } T \leq 20, \\ 3.964 \cdot 10^{-4} - 1.146 \cdot 10^{-5} T + 1.45 \cdot 10^{-7} T^2 - 6.50 \cdot 10^{-10} T^3, & \text{if } T > 20, \end{cases} \\ P_3 &= 1 - 3.83 \cdot 10^{-5} D + 4.9 \cdot 10^{-10} D^2. \end{aligned} \tag{A.9}$$

Here, $\alpha$ [dB/m] is the total absorption coefficient (converted from dB/km), $c_s$ [m/s] is the sound speed, $S$ [psu] is the salinity, $T_{\text{kel}}$ [K] is the temperature in Kelvin, $D$ [m] is the depth, $T$ [°C] is the temperature in Celsius, $f$ [Hz] is the frequency, and $\text{pH}$ is the acidity of the water, taken as a constant at $8$.

# B

# Conceptual framework

Starting from several measurement types, we find the scattering mechanisms using the theoretical frequency dependence of scatterers and the qualitatively predicted scattering by thermal gradients. We infer the height of the stratification, arriving at a thermocline height time series. Then, we research the presence of internal processes (i.e., high-frequency and basin-scale internal waves) by finding specific frequency components in this signal. We find the frequencies of interest by using the measurements to determine the buoyancy frequency and internal seiching frequencies.

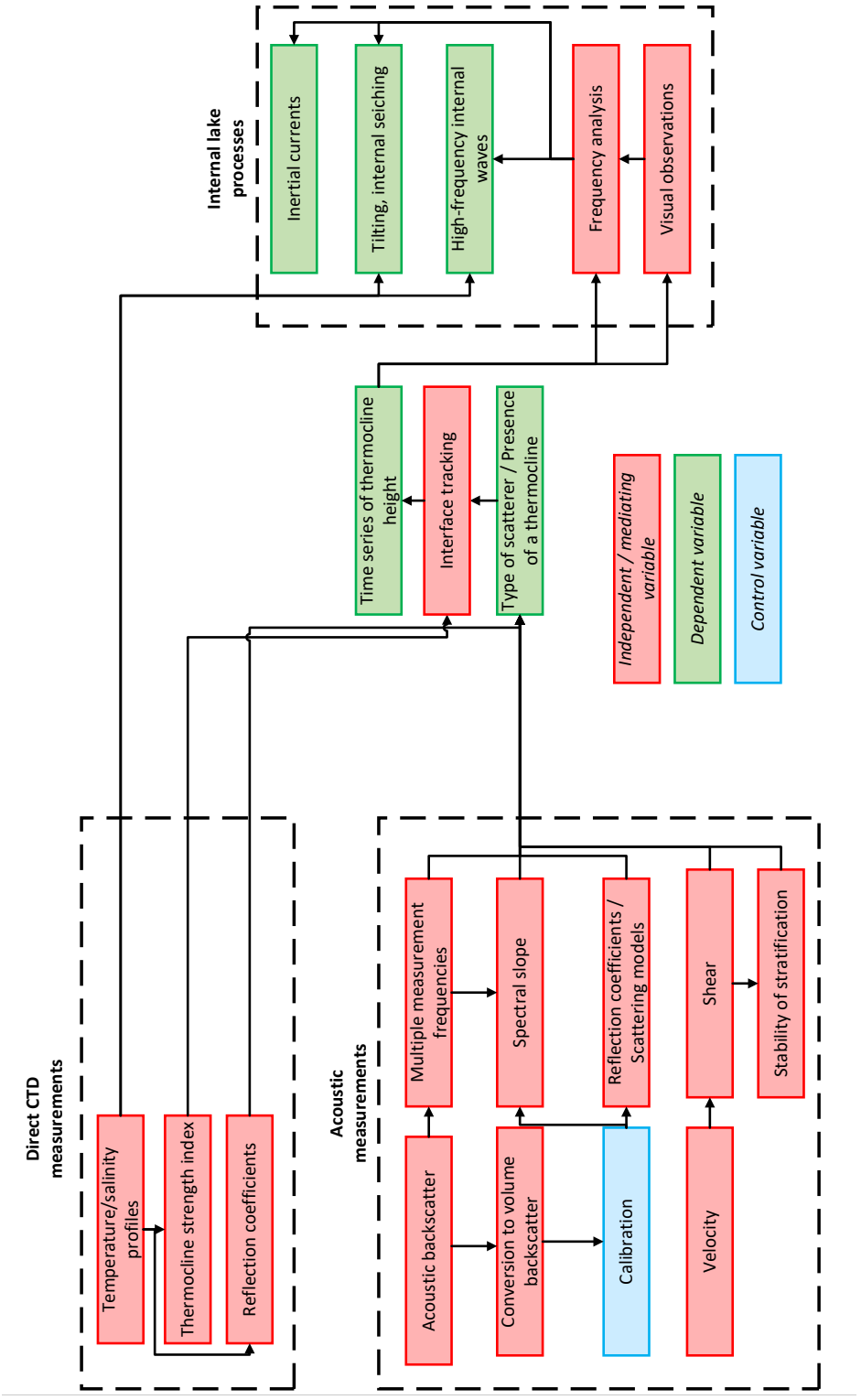


**Figure B.1:** Conceptual framework for this research. Several variable types are distinguished: dependent, independent, and control.

# C
# Acoustic data processing

## C.1. Assessment of variable grid size

The acoustic grid is based on a nominal sound velocity of $1500\,\mathrm{m/s}$, but in reality varies along with variations in the speed of sound, which in turn varies with temperature, salinity, and pressure (in order of importance). The amount of variation (and thus the necessity of including it) is included as part of this research. Besides the research into the influence of this variation on cell size, cell sizes are kept constant after a temporally constant correction. We make a first-order estimate of the actual grid by assuming a temperature, salinity, and pressure distribution to determine the speed of sound. Since pressure has a minor influence on the speed of sound, it is assumed that the surface height is constant at $r_{\mathrm{max}} \in [13.25, 17.49]$ for ADCP3 and ADCP6, respectively, when interpolating the atmospheric pressure at the surface to the bottom pressure measured by the ADCP. Additionally, the pressure distribution is assumed to be linear, implying a constant density and hydrostatic pressure. The atmospheric pressure was obtained from Rijkswaterstaat (2024). Salinity is assumed constant at the value measured by the RBR*concerto*$^3$ of the respective mooring, which seems like a reasonable assumption according to the CastAway and TSO measurements. Finally, we use the temperature profile measured by mooring 2, which lies closest to both ADCPs. The part of the water column that is not covered by the temperature sensors is padded with the temperatures measured at the respective ends of the mooring.

## C.2. Outlier removal and burst averaging

Outliers are removed from the acoustic backscatter using the mean and standard deviation in $\log$-space. The large difference in the linear domain makes the mean susceptible to outliers, which we mitigate by working in the logarithmic domain. We filter outliers using the geometric mean

$$\mu_{\mathrm{geom}} = \left( \prod_{n=1}^{N_{\mathrm{samples}}} P_{r,n} \right)^{1/N_{\mathrm{samples}}} \tag{C.1}$$

plus or minus one geometric standard deviation

$$\sigma_{\mathrm{geom}} = \exp \sqrt{\frac{1}{N} \sum_{n=1}^{N_{\mathrm{samples}}} \left( \ln \frac{P_{r,n}}{\mu_{\mathrm{geom}}} \right)^2}, \tag{C.2}$$

where $N_{\mathrm{samples}}$ is the number of samples per burst.

The handling of a three-month data record is facilitated by averaging to a more tangible time resolution. This also reduces the large amount of noise associated with acoustic backscatter. The acoustic data is burst-averaged (using the geometric mean), which means that the temporal resolution is reduced from $4\,\mathrm{Hz}$ to $0.5\,\mathrm{min}^{-1}$ (for each burst), which in practice reduces to $0.167\,\mathrm{min}^{-1}$ due to the idle period in each burst. The time resolution is then rounded to whole minutes to remove small discrepancies of order $0.1\,\mathrm{s}$.

## C.3. Noise floor correction

The range at which the noise floor is reached is estimated using the asymptote method to estimate the noise threshold ($NT$). Using $P_r\left(t,r\right)=0$, Equation (2.20) is (visually) optimized to find a constant value for $NT$ at which the asymptote is correctly represented. We also refer to Jaarsma (2023) for measurements of the noise threshold at $1000$, $500$, and $250$ kHz. Replacing $P_r$ with $NT$ in Equation (2.20) gives $S_{v,NT}$, which we use to correct our first estimate of $S_v$ using

$$S_{v,c}=10\log_{10}\left(10^{S_v/10}-10^{S_{v,NT}/10}\right). \tag{C.3}$$

We then compute $SNR$ through

$$SNR=20\log\frac{S_{v,\text{signal}}}{S_{v,\text{noise}}}, \tag{C.4}$$

which reduces to

$$SNR=S_{v,\text{signal+noise}}-S_{v,\text{noise}} \tag{C.5}$$

under the assumption that we cannot measure individual contributions of signal or noise.

Finally, we filter low-$SNR$ using thresholding, removing all data where $S_v-S_{v,NT}<SNR_{\text{th}}$. We arbitrarily put the threshold at $3$ dB (Bassett and Zeiden, 2023). "Arbitrarily" is key here, since this is an indiscriminate but arbitrary removal data where $S_v$ is low compared to the estimated noise floor. This process is repeated for each frequency, although estimates may be less accurate for smaller frequencies since the range, at which the noise floor is reached is outside of the ADCP range.

## C.4. Median filter

As mentioned in the previous section, data is burst averaged. This smooths the data, but the echograms are still susceptible to some noise. Even small noise influences the point at which the gradient is at a maximum so it is best to filter them out. Several (combinations of) methods were explored to find a suitable method of smoothing the data before finding the maximum gradient. These methods were based on using different types of window functions and on the discrete wavelet transform.

The most intuitive way of smoothing the data is using a rolling mean. This method smears out gradients, complicating the localization of the sharp gradients associated with a thermocline. A similar but more logical approach is thus to apply median filters, which remove noise by omitting very local peaks but do not smear out values across a sharp interface. These are often used in image processing since they remove noise without affecting borders. Furthermore, they may be applied in both linear or logarithmic space, since this transformation does affect the sorting of values within the median window.

Several types of median filters exist, each with their own added complexity, such as percentile filters (the median being the $50\,\%$ percentile) and the rank filter which is mostly used in image processing. The more complex filters hold great optimizing potential, but a simple median filter of size 5 is chosen for this application, meaning that we use 2 points in all directions to compute the median. An important realization is the non-linearity of this filter. These operations are irreversible and energy is not preserved. This means that efforts at inverse modelling, e.g., backscatter by the pycnocline, will be quantitatively wrong. Since, in this case, only the height is derived from the acoustic backscatter, this does not influence the analysis.

In image processing, another common denoising method is the discrete wavelet transform (DWT). This method allows for analysis at different scales and breaks down a signal by fitting wavelet functions using wavelet coefficients. By thresholding these coefficients, the most important ones are found and used to denoise a signal by representing it more sparsely. This technique is commonly extended to two dimensions for image denoising, though this is less intuitive for spatiotemporal data. Each cell is therefore treated as a single time series and subsequently denoised using DWT. In the $r$-direction, a median filter then provides the necessary smoothing step.

## C.5. Coordinate transformations

Nortek Support (2022, 2024a) provide the general process of converting BEAM coordinates to local cartesian ($xyz$) coordinates and subsequently to Earth (ENU) coordinates. BEAM coordinates are converted to $xyz$ coordinates using a constant transformation matrix specific to each instrument. In the case of a four-beam ADCP with slanted $25^\circ$ beams, the $x$ and the $y$ components are measured by opposing pairs of beams and are computed as

$$u_x = \frac{u_1 - u_3}{2\sin\theta} \tag{C.6}$$

and

$$u_y = \frac{u_2 - u_4}{2\sin\theta}, \tag{C.7}$$

where $\theta = 25^\circ$ is the beam angle. The $z$-component is found similarly, although twice, through

$$u_{z_1} = \frac{u_1 + u_3}{2\cos\theta}, \tag{C.8}$$

and

$$u_{z_2} = \frac{u_2 + u_4}{2\cos\theta}. \tag{C.9}$$

The instrument locally records the heading, pitch, and roll to detect the orientation of the instrument in space. In that respective order, three transformation matrices are combined to arrive at a final transformation matrix of

$$R_4 = \begin{bmatrix} \cos(h)\cos(p) & \cos(h)\sin(p)\sin(r) + \sin(h)\cos(r) & \frac{\cos(h)\sin(p)\cos(r) - \sin(h)\sin(r)}{2} & \frac{\cos(h)\sin(p)\cos(r) - \sin(h)\sin(r)}{2} \\ -\sin(h)\cos(p) & -\sin(h)\sin(p)\sin(r) + \cos(h)\cos(r) & \frac{-\sin(h)\sin(p)\cos(r) - \cos(h)\sin(r)}{2} & \frac{-\sin(h)\sin(p)\cos(r) - \cos(h)\sin(r)}{2} \\ \sin(p) & -\cos(p)\sin(r) & \cos(p)\cos(r) & 0 \\ \sin(p) & -\cos(p)\sin(r) & 0 & \cos(p)\cos(r) \end{bmatrix}, \tag{C.10}$$

where $h$, $p$, and $r$ denote the heading, pitch, and roll as recorded by the instrument. The transformation is then performed using

$$\begin{bmatrix} u_{\mathsf{E}} \\ u_{\mathsf{N}} \\ u_{\mathsf{U};1} \\ u_{\mathsf{U};2} \end{bmatrix} = R_4 \begin{bmatrix} u_x \\ u_y \\ u_{z;1} \\ u_{z;2} \end{bmatrix}. \tag{C.11}$$

Finally, we convert to along-lake and cross-lake coordinates. This is a rotation of the north and east component over an angle $\frac{1}{6}\pi$ rad:

$$\begin{aligned} u_{\mathsf{cross}} &= u_{\mathsf{E}}\cos\tfrac{1}{6}\pi - u_{\mathsf{N}}\sin\tfrac{1}{6}\pi \\ u_{\mathsf{along}} &= u_{\mathsf{E}}\sin\tfrac{1}{6}\pi + u_{\mathsf{N}}\cos\tfrac{1}{6}\pi \end{aligned} \tag{C.12}$$

# D

# CTD casts

## D.1. Exact casts and locations

The figures below show the CTD-cast data as measured in Lake Veere together with their respective locations.

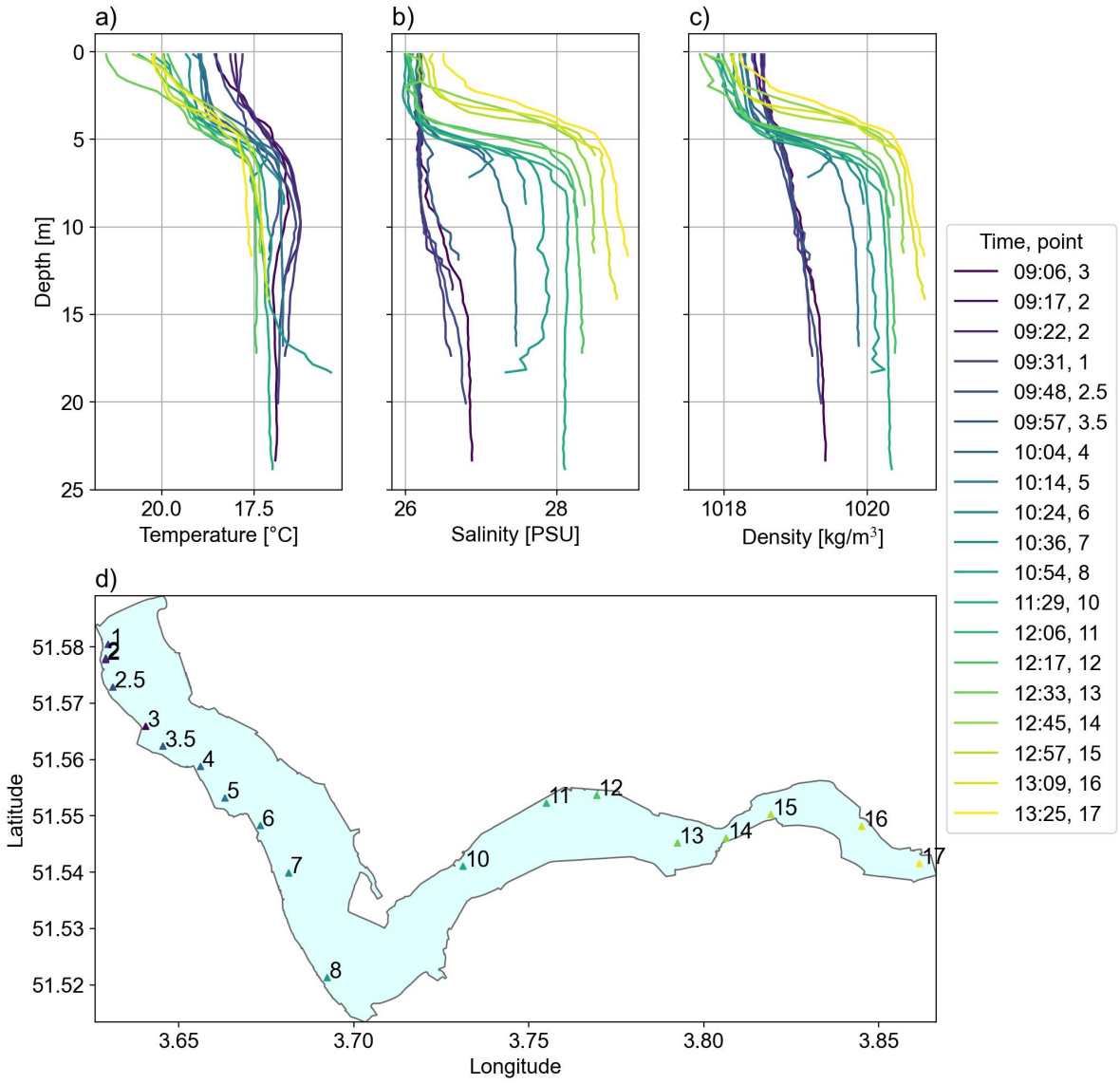


**Figure D.1:** CTD-casts on June 24, 2024, showing a) temperature, b) salinity, c) density, and d) locations. The time of measurement is indicated in the legend.

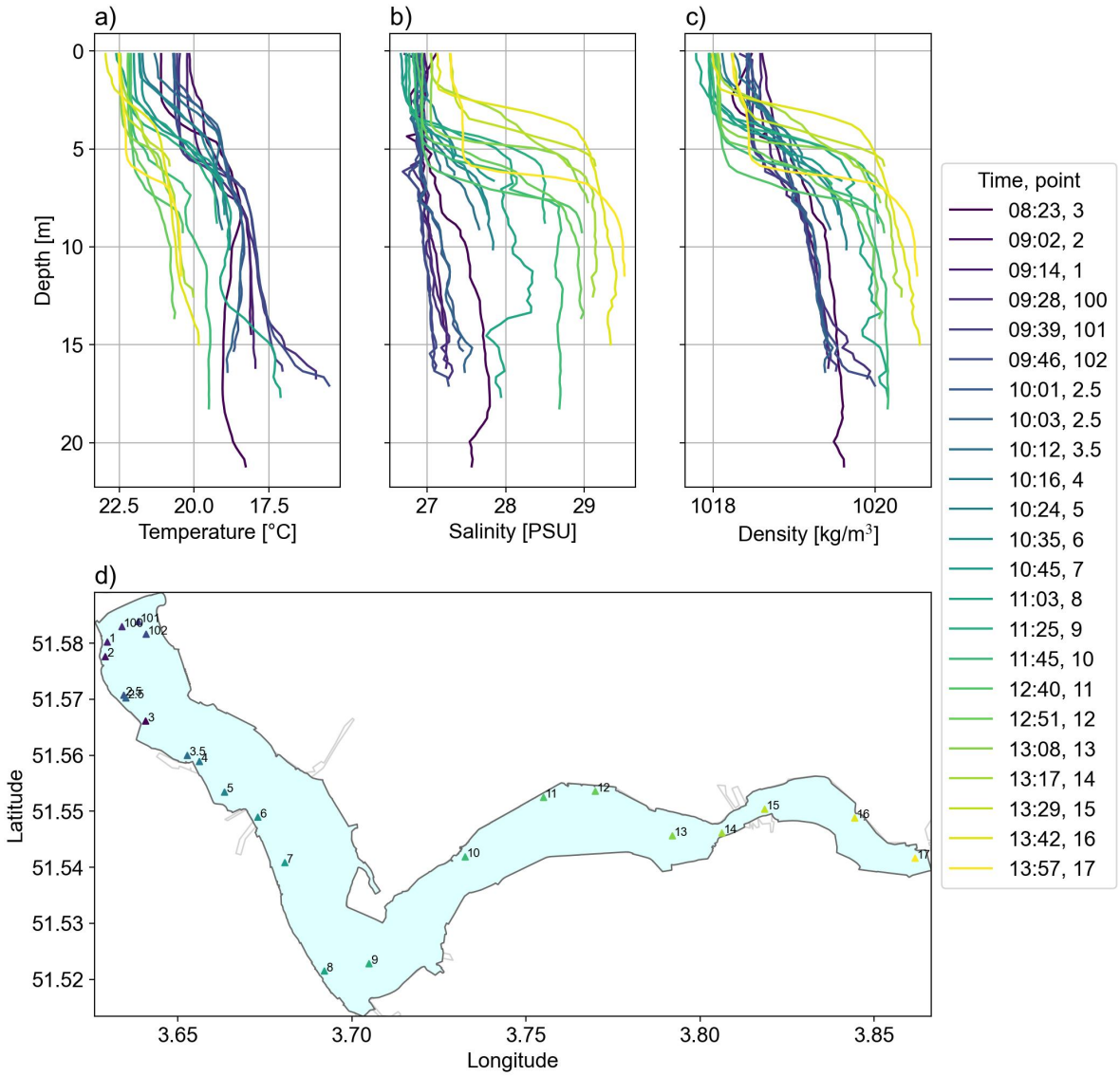


**Figure D.2:** CTD-casts on July 22, 2024, showing a) temperature, b) salinity, c) density, and d) locations. The time of measurement is indicated in the legend.

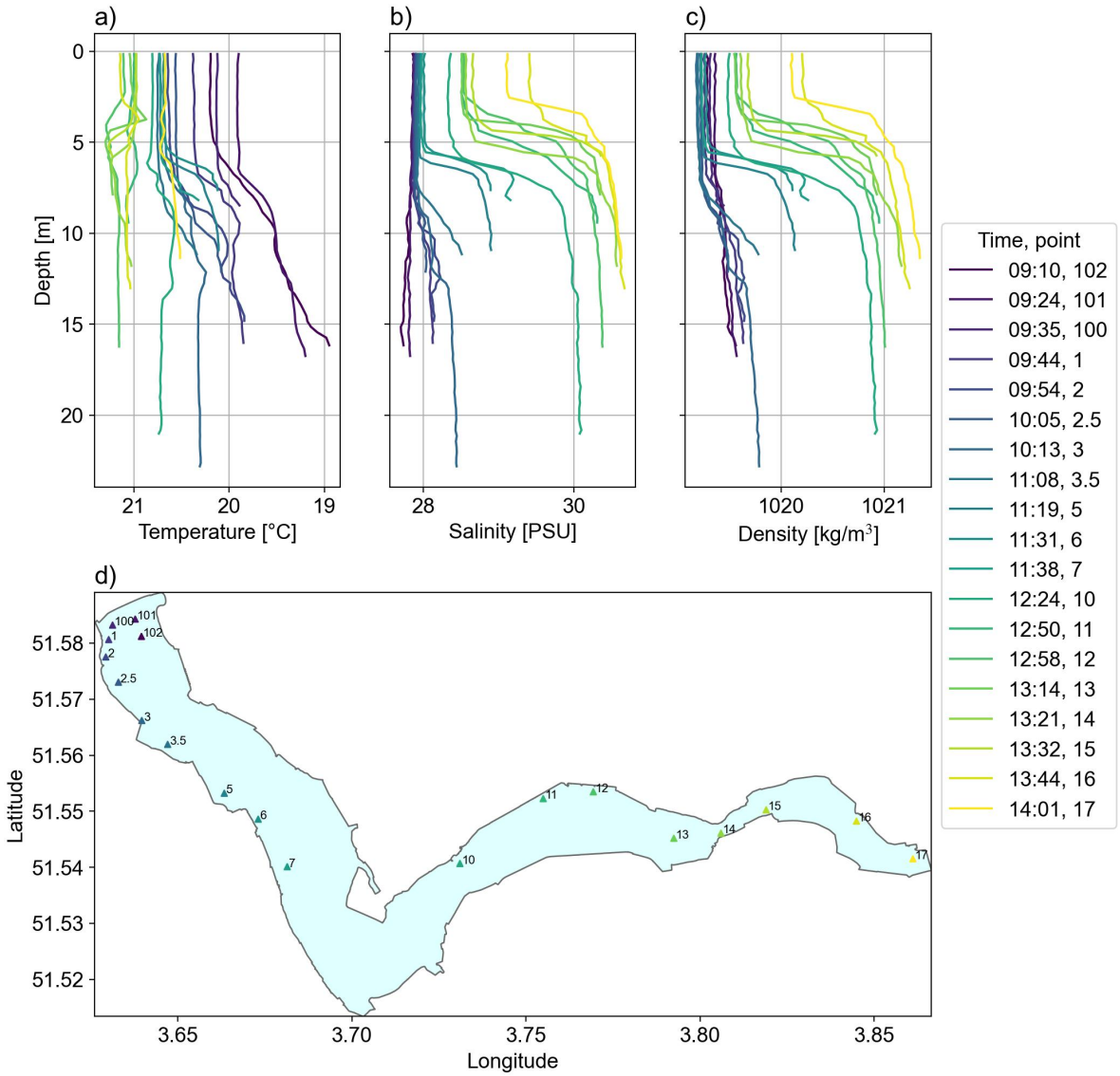


**Figure D.3:** CTD-casts on September 5, 2024, showing a) temperature, b) salinity, c) density, and d) locations. The time of measurement is indicated in the legend.

# D.2. Interpolated transects

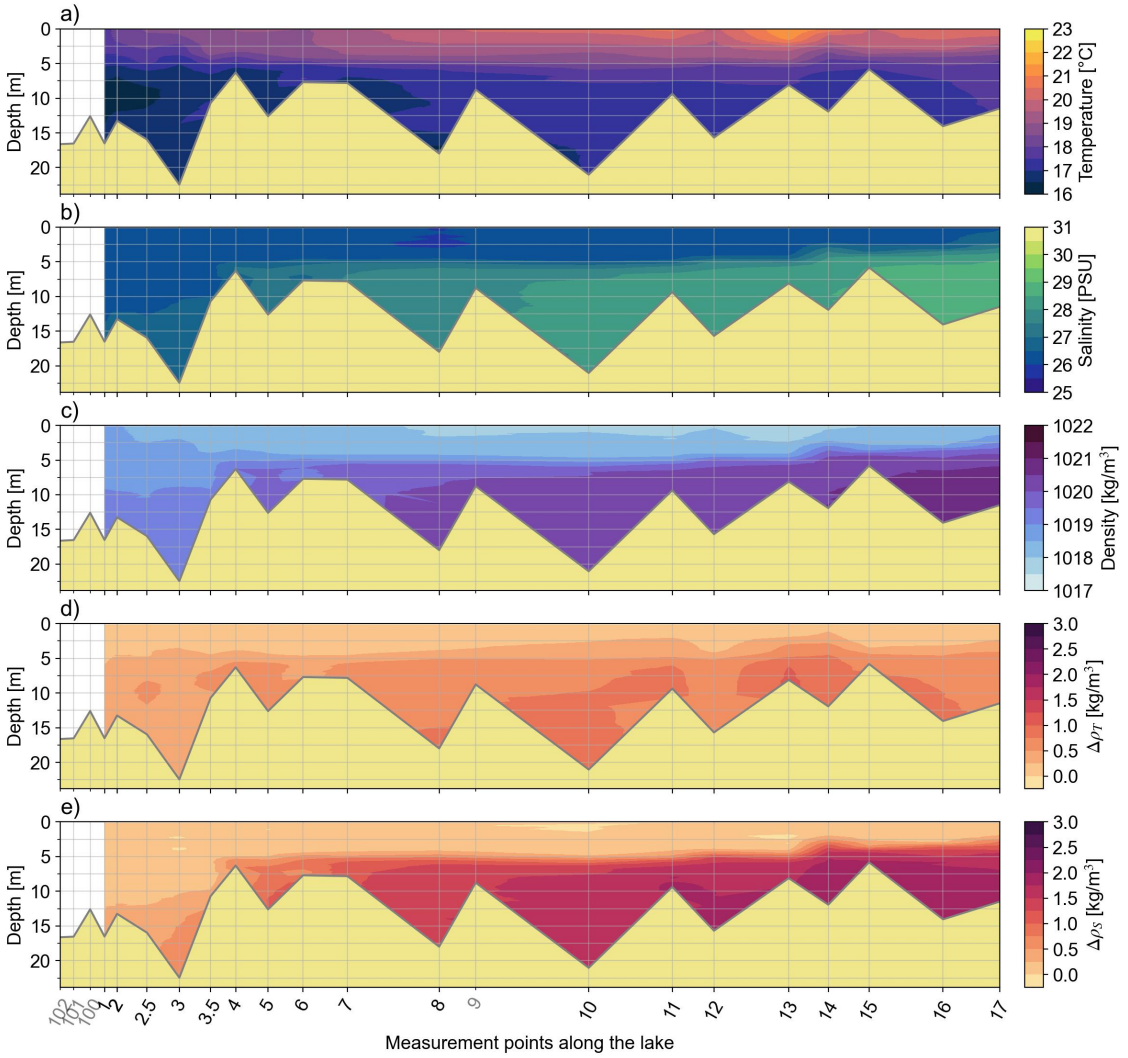


**Figure D.4:** Transects of a) temperature, b) salinity, and c) density of Lake Veere on June 24, 2024. Transect d) shows the contribution of salinity e) and temperature to the density. These constitute the discrepancy between true density and approximate density if d) temperature or e) salinity were taken as constant (i.e., the value at the surface) over the water column. The horizontal axis shows the corresponding RWS measurement points along the lake. Grey labelling indicates that a measurement point was skipped on this day. Data is interpolated between available points. The average location and depth are used for the along lake coordinate and height of the bed, respectively.

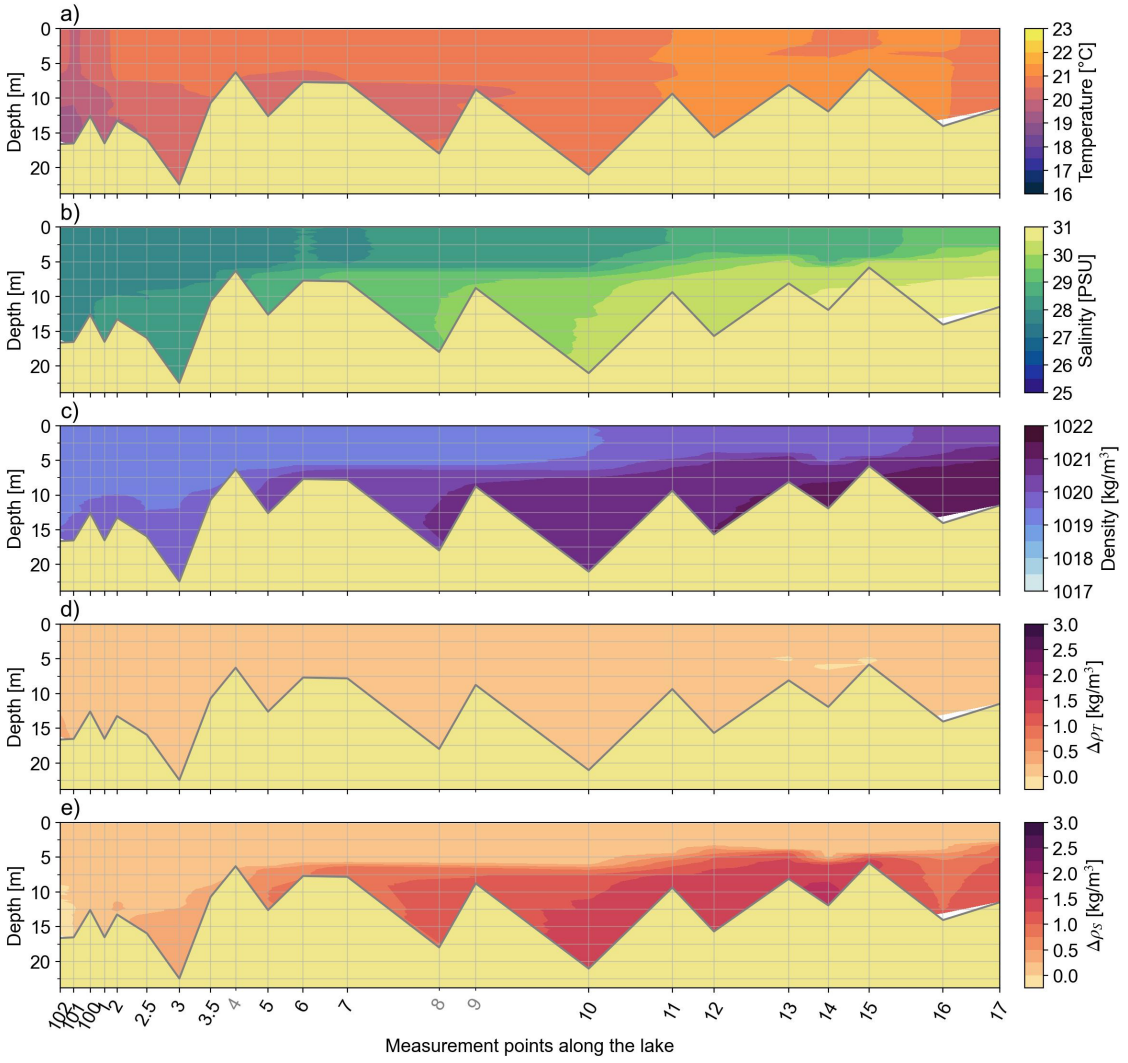


**Figure D.5:** Transects of a) temperature, b) salinity, and c) density of Lake Veere on September 5, 2024. We also show the contributions of d) temperature and e) salinity to the density. These constitute the discrepancy between true density and approximate density if d) temperature or e) salinity were taken as constant (i.e., the value at the surface) over the water column. The horizontal axis shows the corresponding RWS measurement points along the lake. Grey labelling indicates that a measurement point was skipped on this day. Data is interpolated between available points. The average location and depth are used for the along lake coordinate and height of the bed, respectively.

# E

# Richardson numbers

We computed Richardson numbers from the temperature moorings and velocity data. While not exactly co-located, we combined data from mooring 2 and the respective ADCPs. The Richardson numbers are shown in Figures E.1 and E.2. These indicate consistent instability throughout July and August, likely due to the assumption of constant salinity. The lack of salinity measurements obstructs this analysis, but we still observe several events of instability in the upper (thermally stratified) water column during the previously discussed mixing events (e.g., June 10, July 6, July 12, August 24, and more).

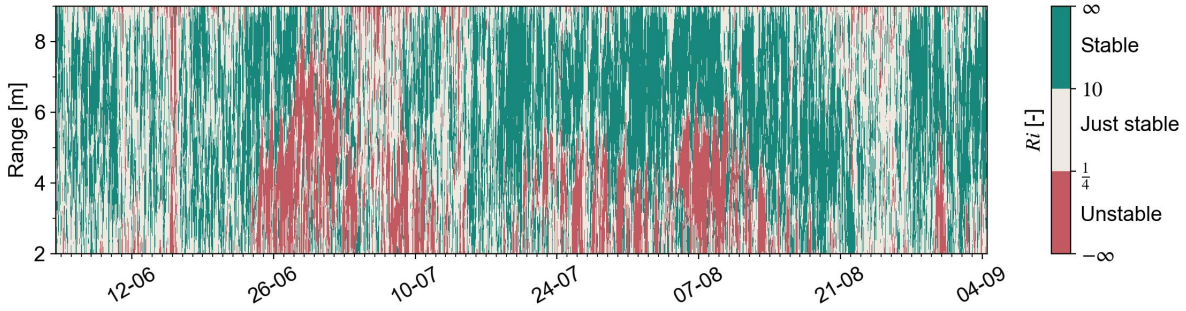


**Figure E.1:** Richardson number during the summer of 2024. Density gradients were computed from temperature and (depth-constant) salinity measured by mooring 2, while velocity data was obtained from ADCP3. We distinguish unstable ($Ri_g < \frac{1}{4}$), just stable ($\frac{1}{4} \leq Ri_g < 10$), and stable ($Ri_g \geq 10$) regimes.

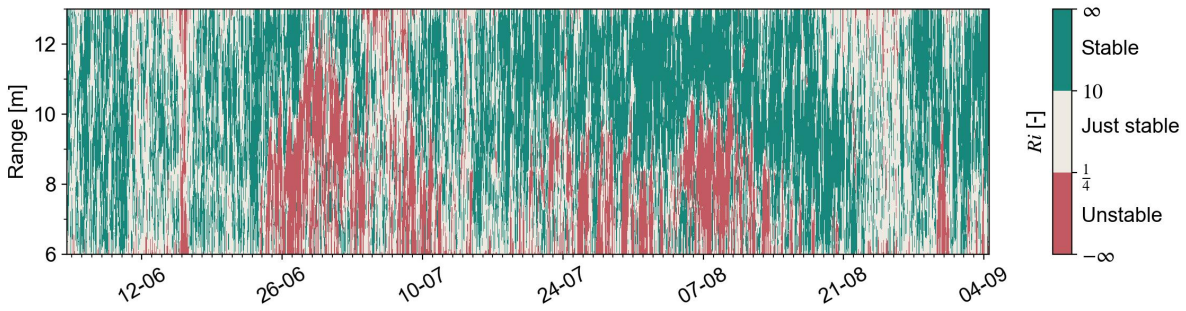


**Figure E.2:** Richardson number during the summer of 2024. Density gradients were computed from temperature and (depth-constant) salinity measured by mooring 2, while velocity data was obtained from ADCP6. We distinguish unstable ($Ri_g < \frac{1}{4}$), just stable ($\frac{1}{4} \leq Ri_g < 10$), and stable ($Ri_g \geq 10$) regimes.

# F

# Acoustic backscatter

## F.1. Raw data

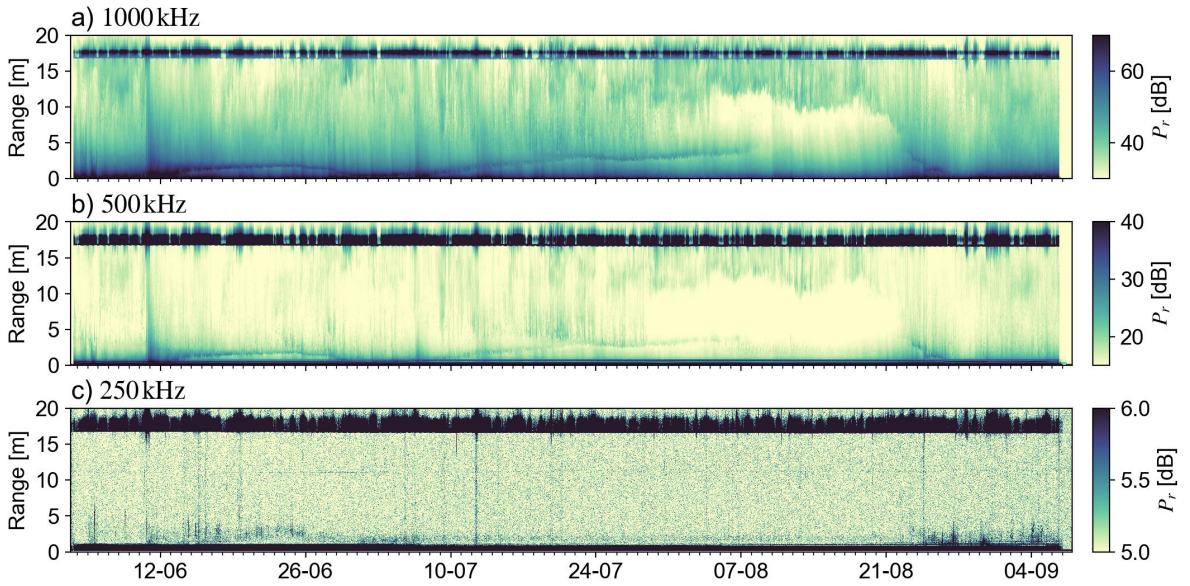


**Figure F.1:** ADCP6: raw acoustic backscatter for measurement frequencies a) $1000$, b) $500$, and c) $250$ kHz, This is pre-processed to remove outliers greater than one daily geometric standard deviation from the daily mean and subsequently averaged per burst.

## F.2. Volume backscatter

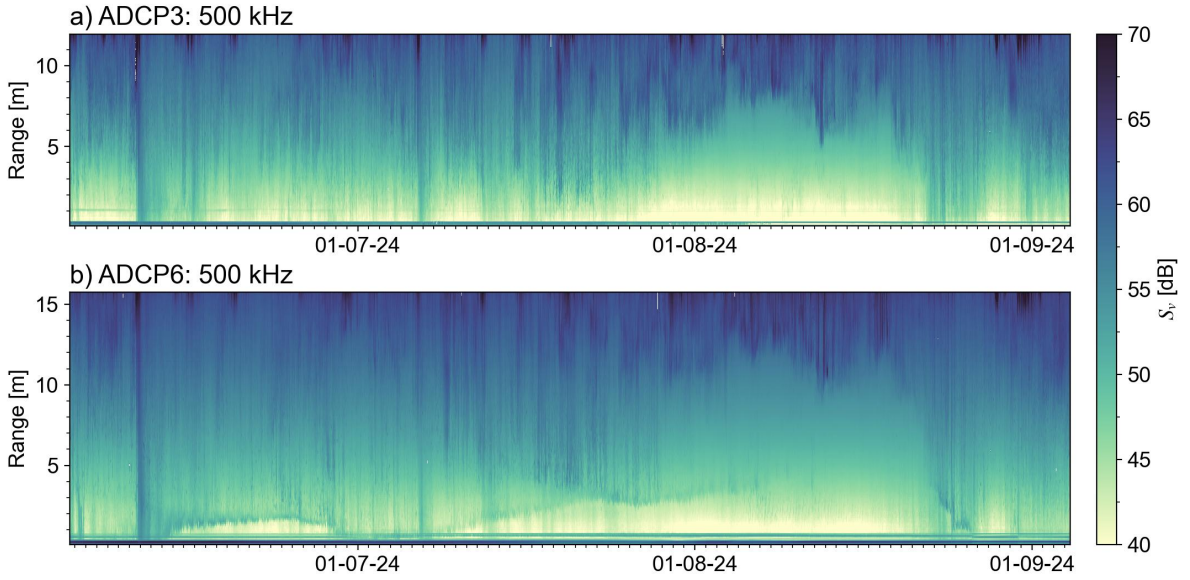


**Figure F.2:** Volume backscatter of the second measurement frequency, $500$ kHz, measured by a) ADCP3 and b) ADCP6.

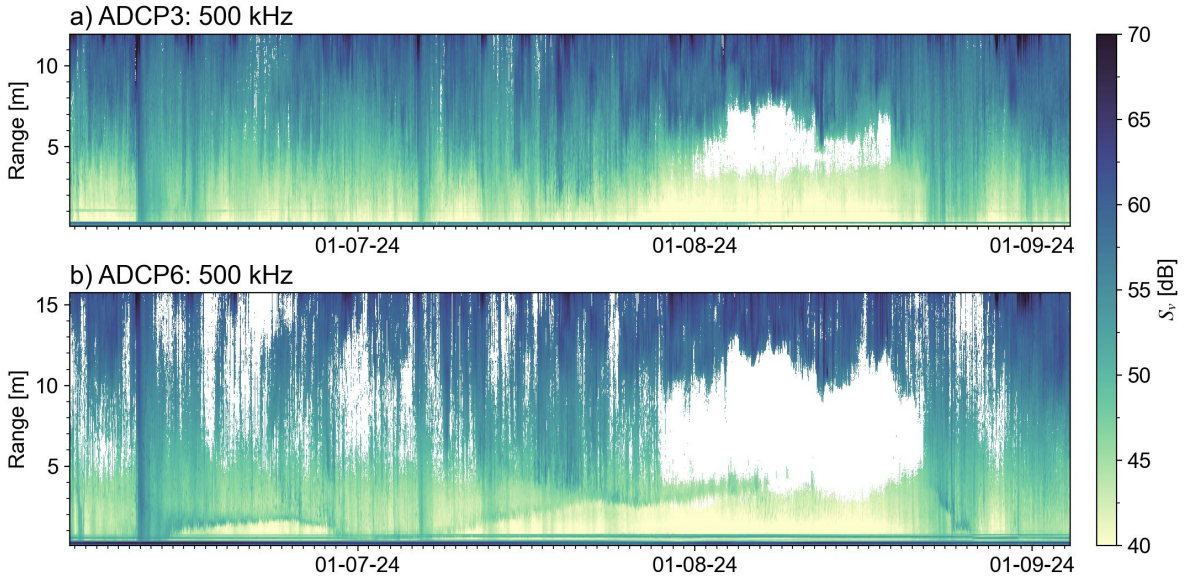


**Figure F.3:** Volume backscatter corrected for noise using an SNR of $3$ dB and a (conservative) noise threshold $12$ dB of the second measurement frequency, $500$ kHz, measured by a) ADCP3 and b) ADCP6. This illustrates the proximity to the noise floor with which the $500$ kHz channel operates.

# F.3. Events

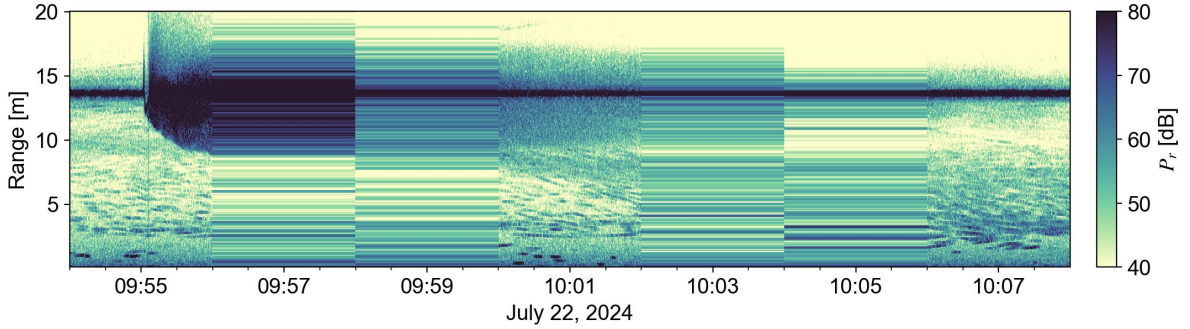


**Figure F.4:** Raw acoustic backscatter by ADCP3 when the TSO measurement vessel (”Roompot”) passed by. Periods of constant backscatter (observed as horizontal bars) occur during the idle period of each measurement burst ($4$ minutes of idling per $6$ minutes measurement burst). One question remains: Patrick or pycnocline?

# F.4. Tracked interfaces

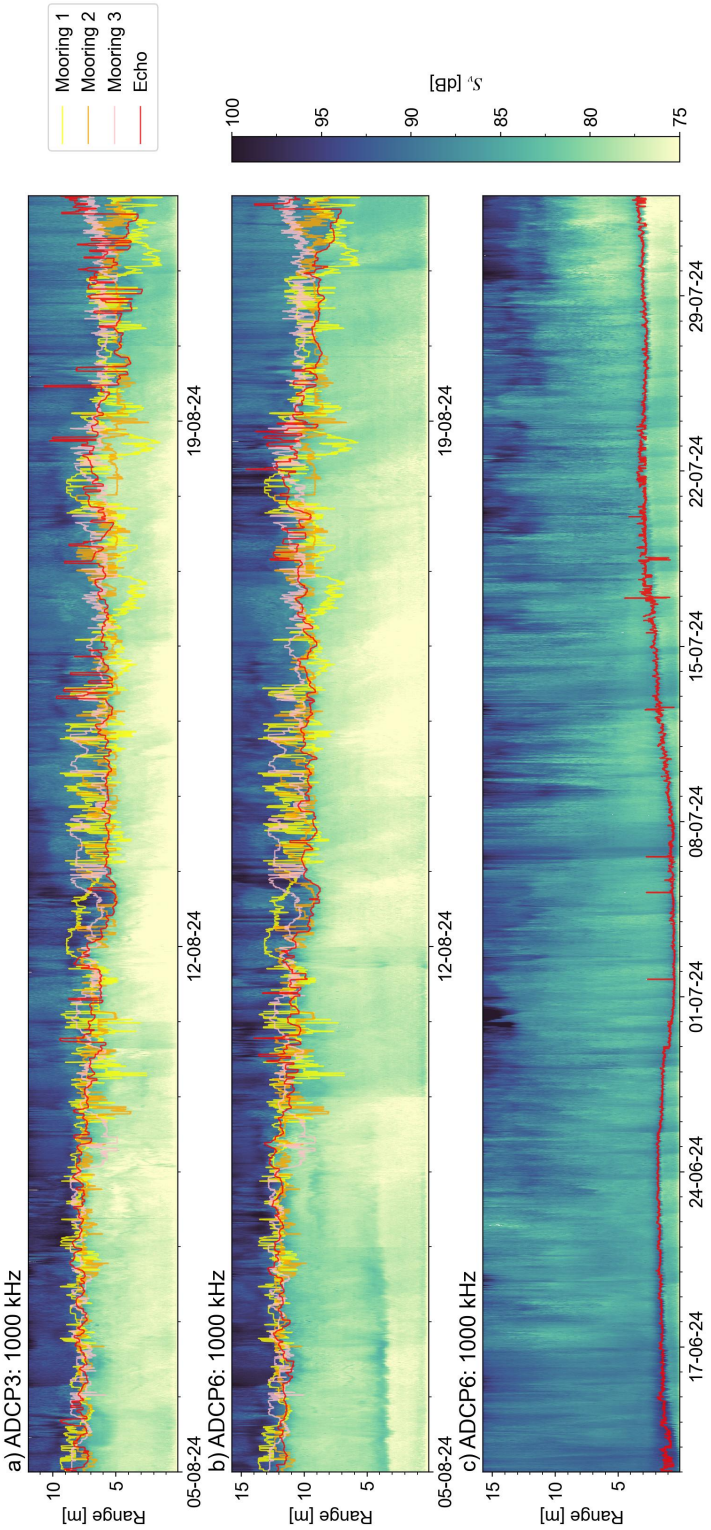


**Figure F.5:** Interface between the top and bottom layer determined through the maximum gradient in volume backscatter (red; different for each plot) and maximum temperature gradient (rest; same for both plots) for the respective moorings. Panels a) and b) show the interface and volume backscatter for ADCP3 and ADCP6, respectively. Panel c) shows the tracked maximum backscatter interface that was observed with ADCP6. Note the different timescales between plots (a, b) and (c).

# G

# Continuous wavelet transforms

## G.1. Windowed Fourier transforms

Here we include the windowed Fourier spectra (spectrograms). We derived these as per the first step of continuous wavelet analysis, i.e., establishing the necessity of a non-stationary analysis (see Section 3.3). We highlighted the same regions as Figures 4.17 and 4.18.

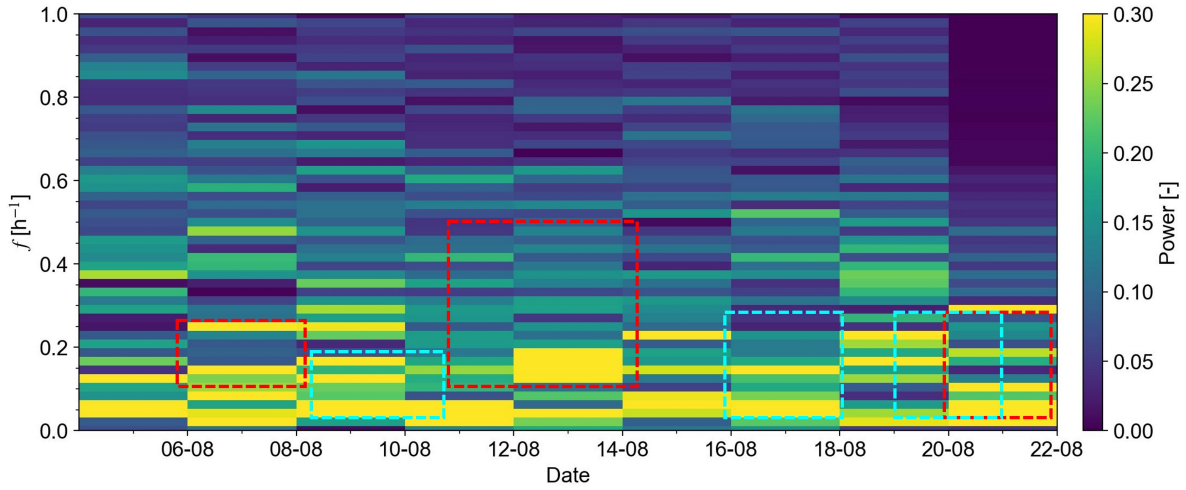


**Figure G.1:** Spectrogram of the tracked interface time series measured by ADCP3. We used a window of 2 days. We highlighted the same regions as in Figures 4.17 and 4.18.

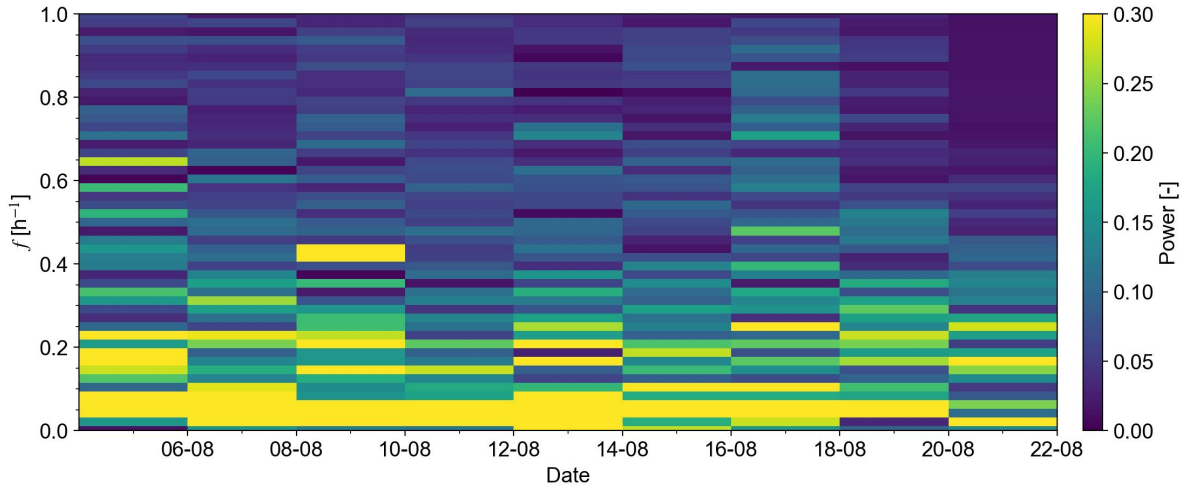


**Figure G.2:** Spectrogram of the tracked interface time series measured by ADCP6. We used a window of 2 days.

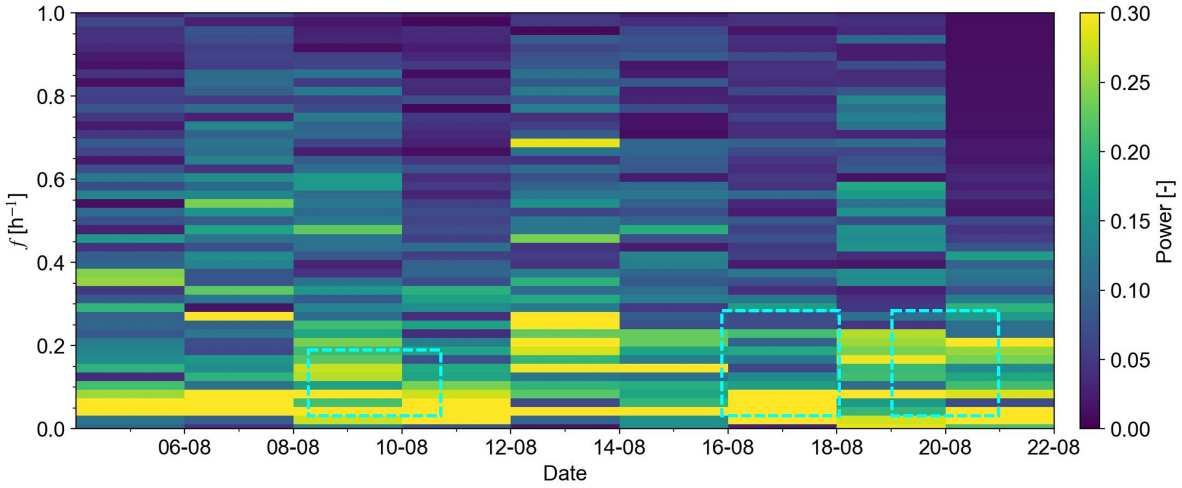


**Figure G.3:** Spectrogram of the tracked interface time series measured by Mooring 1. We used a window of 2 days. We highlighted the same regions as in Figure 4.18.

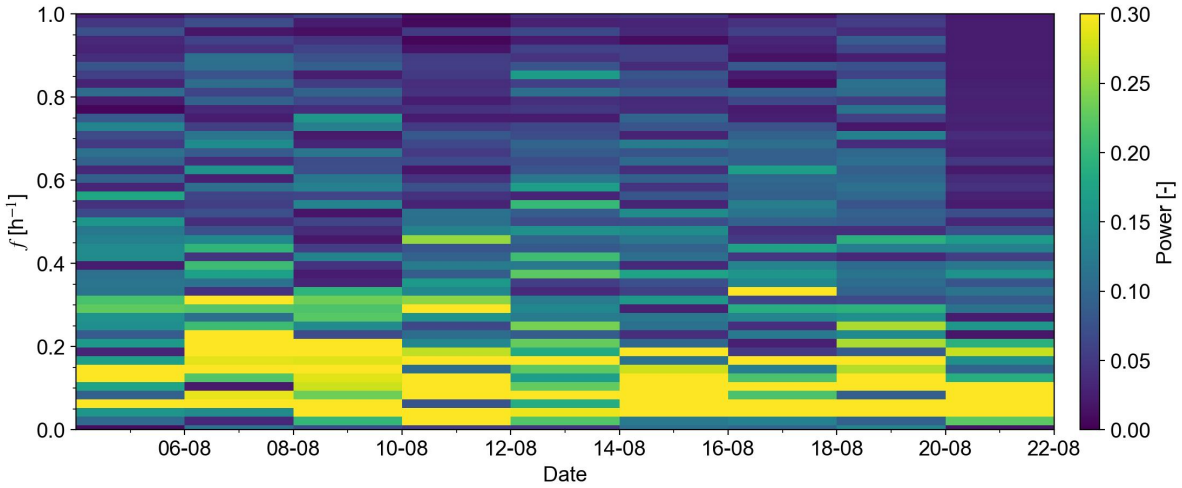


**Figure G.4:** Spectrogram of the tracked interface time series measured by Mooring 2. We used a window of 2 days.

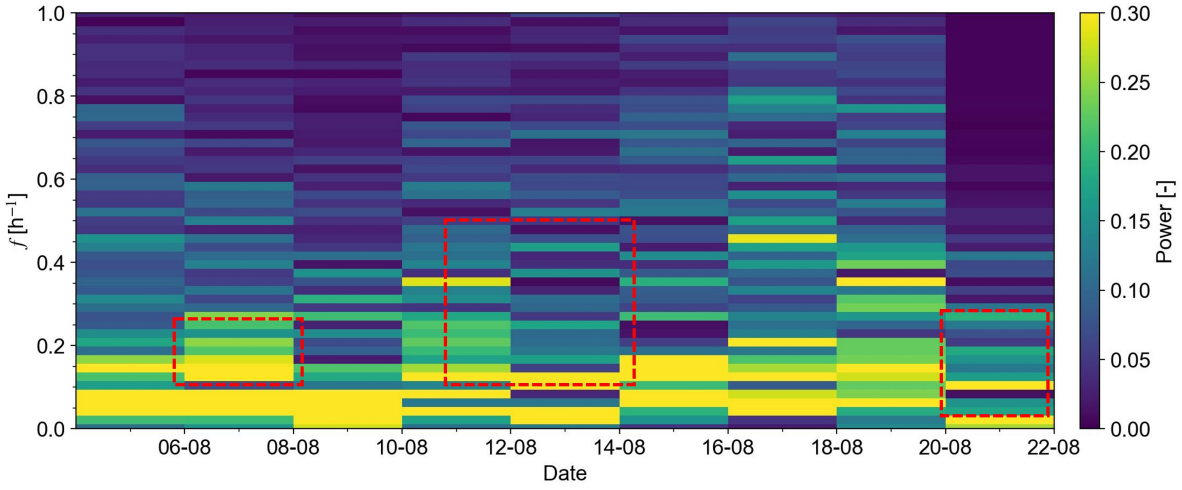


**Figure G.5:** Spectrogram of the tracked interface time series measured by Mooring 3. We used a window of 2 days. We highlighted the same regions as in Figure 4.17.

## G.2. Continuous wavelet transforms

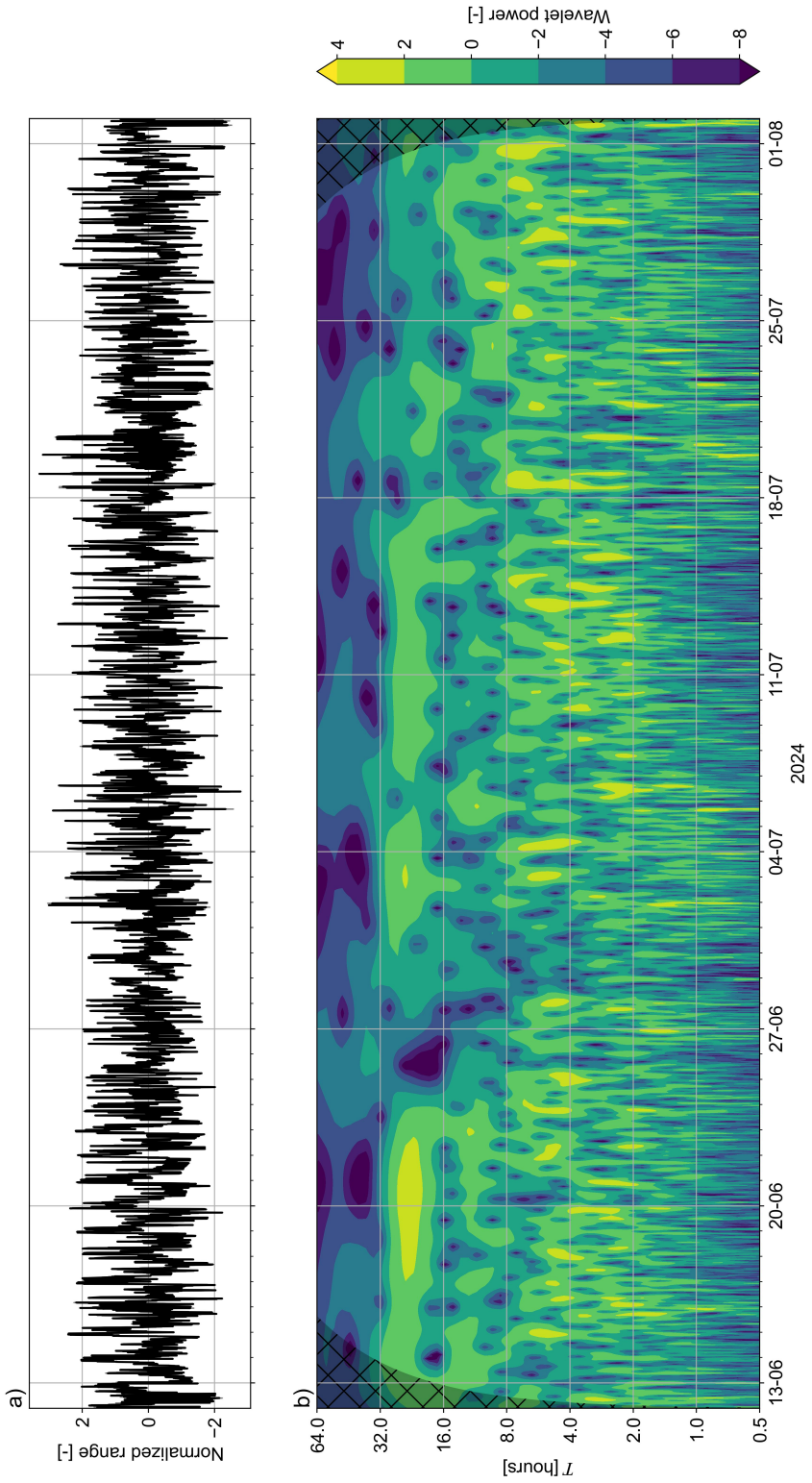


**Figure G.6:** CWT of the lower layer measured by ADCP6. We show the a) outlier-removed, de-trended, normalized time series of interface heights and b) the wavelet spectrum, indicating Fourier periods on the vertical axis and time on the horizontal axes.

# G.3. Wavelet coherence transforms

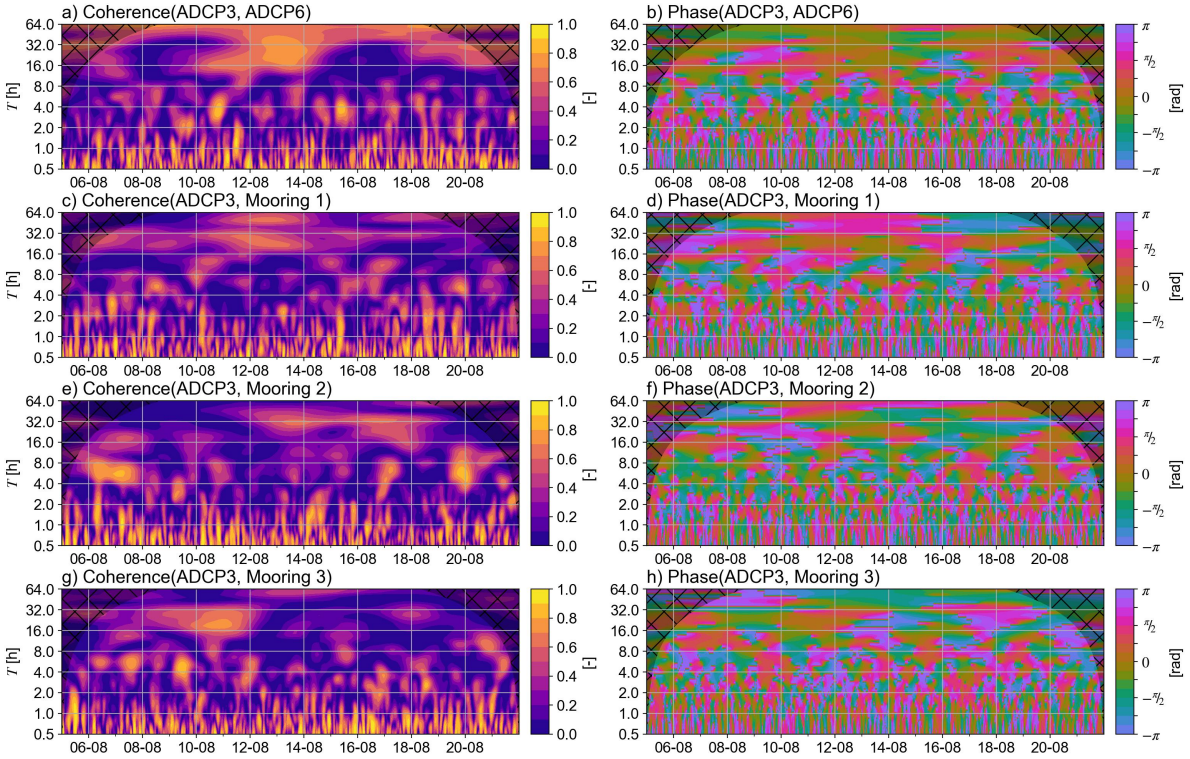


**Figure G.7:** Wavelet coherence transform of the tracked interface time series measured by ADCP3 with each of the other time series. The left plots show the magnitude $[0, 1]$ of the complex coherence, and the right plots show the phase angle $[-\pi, \pi]$ of the complex coherence between the respective signals. Note that phase angles should only be analyzed in areas with increased coherence.

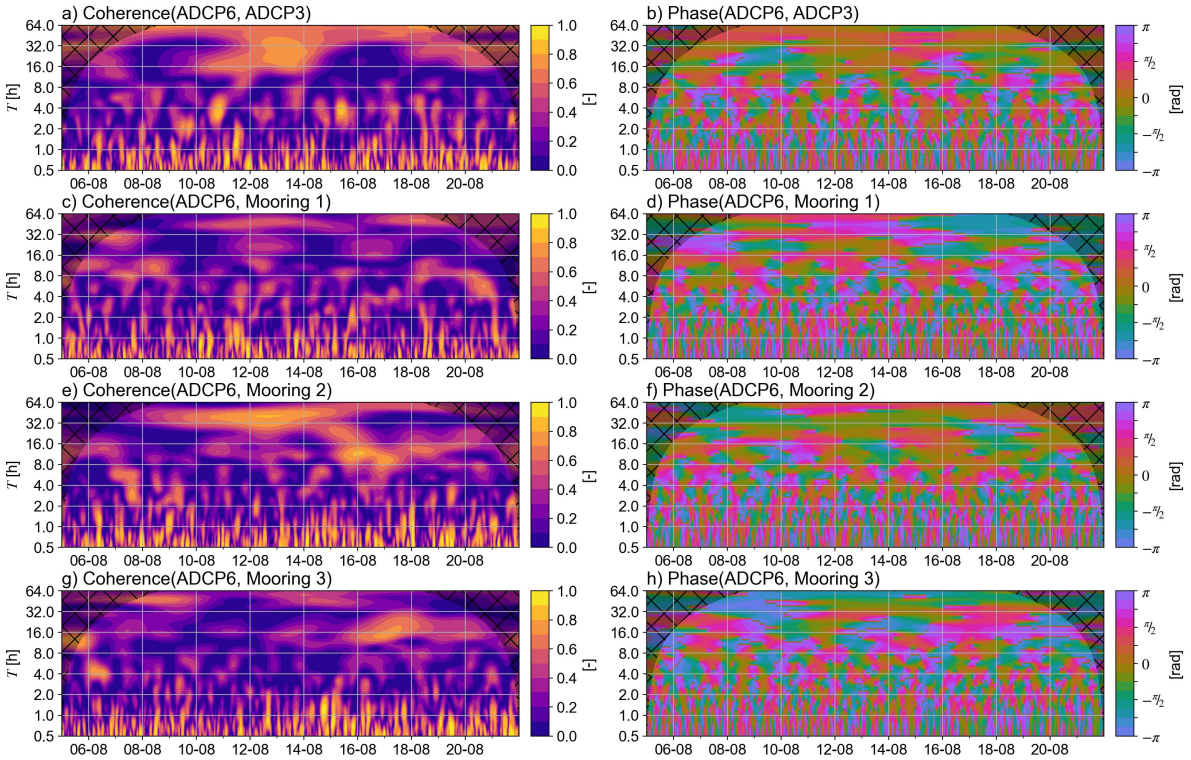


**Figure G.8:** Wavelet coherence transform of the tracked interface time series measured by ADCP6 with each of the other time series. The left plots show the magnitude $[0, 1]$ of the complex coherence, and the right plots show the phase angle $[-\pi, \pi]$ of the complex coherence between the respective signals. Note that phase angles should only be analyzed in areas with increased coherence.

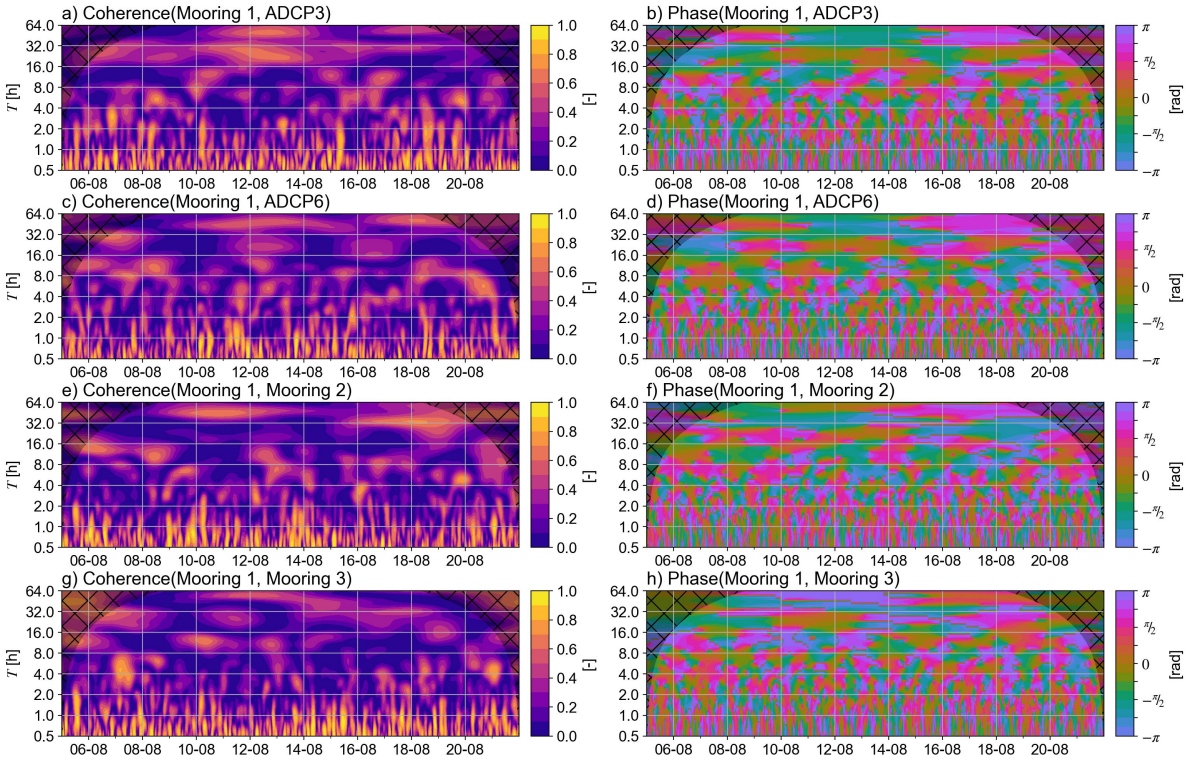


**Figure G.9:** Wavelet coherence transform of the tracked interface time series measured by mooring 1 with each of the other time series. The left plots show the magnitude $[0, 1]$ of the complex coherence, and the right plots show the phase angle $[-\pi, \pi]$ of the complex coherence between the respective signals. Note that phase angles should only be analyzed in areas with increased coherence.

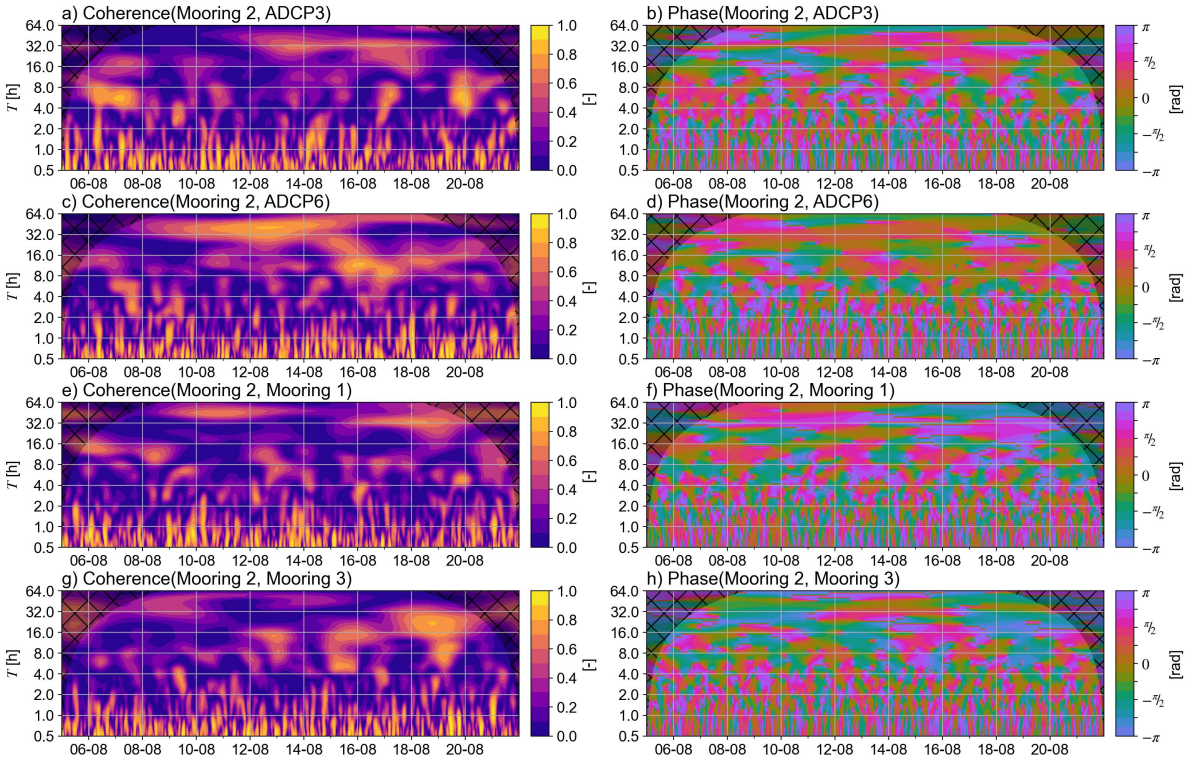


**Figure G.10:** Wavelet coherence transform of the tracked interface time series measured by mooring 2 with each of the other time series. The left plots show the magnitude $[0, 1]$ of the complex coherence, and the right plots show the phase angle $[-\pi, \pi]$ of the complex coherence between the respective signals. Note that phase angles should only be analyzed in areas with increased coherence.

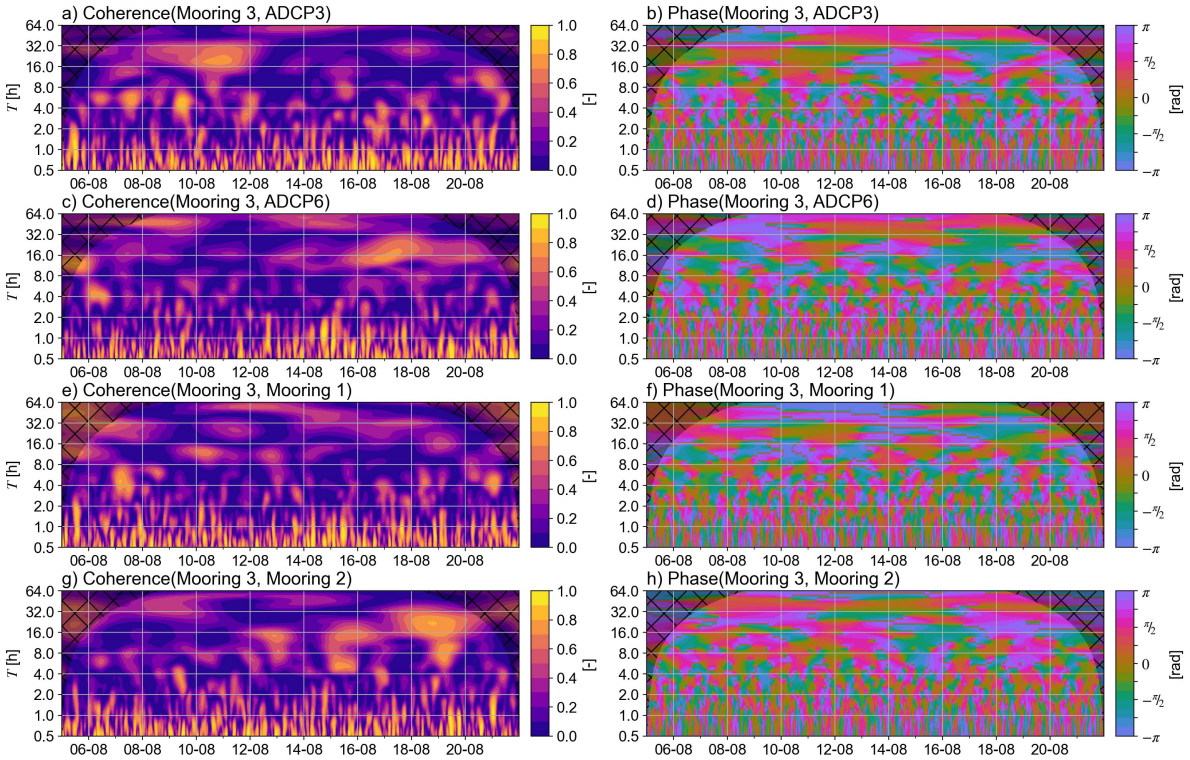


**Figure G.11:** Wavelet coherence transform of the tracked interface time series measured by mooring 3 with each of the other time series. The left plots show the magnitude $[0, 1]$ of the complex coherence, and the right plots show the phase angle $[-\pi, \pi]$ of the complex coherence between the respective signals. Note that phase angles should only be analyzed in areas with increased coherence.

**Table G.1:** Observed periods of increased coherence between different signals and the corresponding phase difference. Devices 1 and 2 indicate the signals between which we computed coherence and phase. We distinguished the following bands: daily, semi-daily, and $4$-$8$ hours. Higher frequencies become increasingly difficult to identify due to leakage of wavelet power and associated spuriously high coherence.

| Fourier period | Date(s) (in August, 2024) | Device 1 | Device 2 | Phase difference [rad] |
|---|---|---|---|---|
| **24 hours** | 6-8 | Mooring 1 | Mooring 3 | $-1/2\pi$ |
| | 8-14 | ADCP3 | Mooring 1 | 0 |
| | 10-12 | ADCP3 | Mooring 3 | 0 |
| | 10-14 | ADCP3 | Mooring 1 | 0 |
| | 11-13 | ADCP6 | Mooring 1 | $1/2\pi$ |
| | 12-14 | ADCP3 | ADCP6 | 0 |
| | 12-13 | Mooring 1 | Mooring 2 | 0 |
| | 15 | ADCP6 | Mooring 2 | $1/4\pi$ |
| | 16-17 | ADCP6 | Mooring 3 | $1/2\pi$ |
| | 18-19 | Mooring 1 | Mooring 2 | $-3/4\pi$ |
| | 18-20 | ADCP3 | Mooring 2 | 0 |
| | 18-20 | Mooring 2 | Mooring 3 | $\pi/-\pi$ |
| **12 hours** | 5 | Mooring 1 | Mooring 3 | $\pi$ |
| | 6-7 | ADCP3 | ADCP6 | 0 |
| | 6-9 | ADCP6 | Mooring 1 | $1/4\pi$ |
| | 7 | ADCP3 | Mooring 3 | $1/4\pi$ |
| | 10 | ADCP3 | Mooring 1 | $1/2\pi$ |
| | 12 | ADCP6 | Mooring 1 | $1/2\pi$ |
| | 12-13 | ADCP6 | Mooring 2 | $-1/4\pi$ |
| | 12 | Mooring 1 | Mooring 2 | $-1/2\pi$ |
| | 16 | ADCP3 | Mooring 1 | $\pi$ |
| | 18 | ADCP6 | Mooring 1 | $3/4\pi$ |
| | 21 | Mooring 1 | Mooring 2 | $-3/4\pi$ |
| **4-8 hours** | 6-7 | ADCP3 | Mooring 2 | $-1/2\pi$ |
| | 6-7 | ADCP3 | Mooring 3 | $1/2\pi - \pi$ |
| | 6 | ADCP6 | Mooring 3 | $\pi$ |
| | 7 | Mooring 1 | Mooring 3 | $1/2\pi$ |
| | 8 | ADCP3 | Mooring 1 | $-1/4\pi$ |
| | 9 | ADCP3 | Mooring 3 | $1/4\pi$ |
| | 10 | ADCP3 | ADCP6 | 0 |
| | 10 | ADCP3 | Mooring 2 | $-1/4\pi$ |
| | 12 | ADCP3 | Mooring 3 | $\pi$ |
| | 12 | ADCP6 | Mooring 1 | 0 |
| | 12-14 | Mooring 1 | Mooring 2 | $\pi$ |
| | 14 | ADCP6 | Mooring 2 | $1/2\pi$ |
| | 15 | ADCP3 | ADCP6 | 0 |
| | 15-16 | ADCP3 | Mooring 1 | $-1/2\pi$ |
| | 16 | ADCP3 | Mooring 2 | $1/2\pi$ |
| | 18 | ADCP3 | ADCP6 | $1/2\pi$ |
| | 18 | ADCP3 | Mooring 3 | $1/2\pi$ |
| | 19 | ADCP3 | Mooring 1 | $\pi$ |
| | 19 | ADCP3 | Mooring 2 | 0 |
| | 19 | Mooring 1 | Mooring 2 | $\pi$ |
| | 20 | ADCP6 | Mooring 1 | $\pi$ |
| | 21 | ADCP3 | Mooring 3 | $\pi$ |
| | 21 | Mooring 1 | Mooring 3 | $\pi$ |